CAPITAL UNIVERSITY OF SCIENCE AND TECHNOLOGY, ISLAMABAD

Electromagnetic Wave Scattering from Interfaces with Material Contrast

by

Shahana Rizvi

A dissertation submitted in partial fulfillment for the degree of Doctor of Philosophy

in the

Faculty of Computing
Department of Mathematics

2025

Electromagnetic Wave Scattering from Interfaces with Material Contrast

By

Shahana Rizvi

(DMT183002)

Dr. Burhan Tiryakioğlu, Associate Professor

Marmara University, Türkiye

(Foreign Evaluator 1)

Dr. Yukun Guo, Professor

Harbin Institute of Technology, China

(Foreign Evaluator 2)

Dr. Muhammad Afzal

(Research Supervisor)

Dr. Muhammad Sagheer

(Head, Department of Mathematics)

Dr. Muhammad Abdul Qadir

(Dean, Faculty of Computing)

DEPARTMENT OF MATHEMATICS

CAPITAL UNIVERSITY OF SCIENCE AND TECHNOLOGY

ISLAMABAD

2025

Dedicated to My Late Parents

Abbas Jahan

&

Riaz Haider

CAPITAL UNIVERSITY OF SCIENCE & TECHNOLOGY
ISLAMABAD
Expressway, Kahuta Road, Zone-V, Islamabad
Phone:+92-51-111-555-666 Fax: +92-51-4486705
Email: info@cust.edu.pk Website: https://www.cust.edu.pk

CERTIFICATE OF APPROVAL

This is to certify that the research work presented in the dissertation, entitled "**Electromagnetic Wave Scattering from Interfaces with Material Contrast**" was conducted under the supervision of **Dr. Muhammad Afzal**. No part of this dissertation has been submitted anywhere else for any other degree. This dissertation is submitted to the **Department of Mathematics, Capital University of Science and Technology** in partial fulfillment of the requirements for the degree of Doctor in Philosophy in the field of **Mathematics.** The open defence of the dissertation was conducted on **January 10, 2025**.

Student Name : Shahana Rizvi (DMT183002) ________________

The Examination Committee unanimously agrees to award PhD degree in the mentioned field.

Examination Committee :

(a)	External Examiner 1:	Dr. Mahmood ul Hassan Associate Professor COMSATS University, Islamabad	________________
(b)	External Examiner 2:	Dr. Amer Bilal Mann Assistant Professor FUUAST, Islamabad	________________
(c)	Internal Examiner :	Dr. Abdul Rehman Kashif Professor CUST, Islamabad	________________

Supervisor Name : Dr. Muhammad Afzal
Associate Professor
CUST, Islamabad ________________

Name of HoD : Dr. Muhammad Sagheer
Professor
CUST, Islamabad ________________

Name of Dean : Dr. Muhammad Abdul Qadir
Professor
CUST, Islamabad ________________

AUTHOR'S DECLARATION

I, **Shahana Rizvi** (Registration No. **DMT183002**), hereby state that my dissertation titled, "**Electromagnetic Wave Scattering from Interfaces with Material Contrast**" is my own work and has not been submitted previously by me for taking any degree from Capital University of Science and Technology, Islamabad or anywhere else in the country/ world.

At any time, if my statement is found to be incorrect even after my graduation, the University has the right to withdraw my PhD Degree.

(**Shahana Rizvi**)

Dated: 10 January, 2025

Registration No : DMT183002

PLAGIARISM UNDERTAKING

I solemnly declare that research work presented in the dissertation titled "**Electromagnetic Wave Scattering from Interfaces with Material Contrast**" is solely my research work with no significant contribution from any other person. Small contribution/ help wherever taken has been duly acknowledged and that complete dissertation has been written by me.

I understand the zero-tolerance policy of the HEC and Capital University of Science and Technology towards plagiarism. Therefore, I as an author of the above titled dissertation declare that no portion of my dissertation has been plagiarized and any material used as reference is properly referred/ cited.

I undertake that if I am found guilty of any formal plagiarism in the above titled dissertation even after award of PhD Degree, the University reserves the right to withdraw/ revoke my PhD degree and that HEC and the University have the right to publish my name on the HEC/ University Website on which names of students are placed who submitted plagiarized dissertation.

(Shahana Rizvi)

Dated: 10 January, 2025

Registration No : DMT183002

List of Publications

It is certified that following publication(s) have been made out of the research work that has been carried out for this dissertation:-

1. **Shahana Rizvi**, and Muhammad Afzal, "The Electromagnetic Wave Propagation in Discontinuous Waveguide containing Plasma," *Waves in Random and Complex Media*, 1–20 (2023).
2. **Shahana Rizvi**, and Muhammad Afzal, "Cold Plasma-induced Effects on Electromagnetic Wave Scattering in Waveguides: A Mode-matching Analysis," *Communications in Theoretical Physics* 76(3), 035501 (2024).
3. **Shahana Rizvi**, and Muhammad Afzal, "Electromagnetic Wave Scattering in Plasma Beam driven Waveguides under Strong Magnetic Field," *Communications in Theoretical Physics* 76(11), 115502 (2024).

(Shahana Rizvi)

Registration No: DMT183002

Acknowledgement

The attainment of a doctoral degree relies heavily on the support and guidance of specific individuals and the academic department where the research is conducted. I express my gratitude to the Capital University of Science and Technology for offering me the opportunity and creating an environment conducive to achieving my academic aspirations.

I owe a significant debt of gratitude to Dr. Muhammad Afzal, my supervisor, who stands out as the most influential figure in my academic journey. His guidance, mentorship, and unwavering support have been instrumental in steering the research process towards success. Dr. Afzal's expertise, dedication, and commitment to academic excellence have not only enriched my research but also broadened my intellectual horizons. Furthermore, I would like to express my deepest gratitude to Dr. Muhammad Sagheer, the Head of the Department (HoD), for his administrative support. His guidance on academic matters and active supervision of research activities within the department have significantly contributed in fostering a productive and stimulating research environment. Additionally, I am grateful to my fellow researchers who have provided valuable insights and steady support throughout the research process.

I want to express deep appreciation to my husband, Faisal Altaf, for his tireless emotional support and encouragement throughout this challenging journey. I am grateful for the presence of my children Ali Haider and Hadi, as they helped me strike a healthy work-life balance while pursuing my academic goals, showing great understanding towards their mother's challenges. Lastly, I extend my heartfelt thanks to my dear siblings Shaheen Fatima, Saleem Haider, Nadeem Haider, and Ejaz Haider for believing in me and offering moral support through regular check-ins on progress made towards completing my PhD program.

(Shahana Rizvi)

Abstract

This dissertation delves into a comprehensive analysis of electromagnetic wave behavior in rectangular and cylindrical waveguides having variations in medium and geometrical properties. The primary focus is on modeling, propagation, and scattering phenomena, particularly in structures under varying conditions and in the presence or absence of a strong magnetic field. The investigation includes the propagation of electromagnetic waves in diverse structures, such as infinite rectangular waveguides containing semi-bounded regions with cold plasma situated between dielectric layers, as well as rectangular waveguides with grooved structures and central cold plasma slabs. Additionally, the electromagnetic wave scattering in perfectly electric conducting infinite cylindrical waveguides with central chambers filled with cold plasma, vacuum, and dielectric medium is discussed in detail. The formulated boundary value problems, represented by the Helmholtz equation and governed by Maxwell's equations, were solved using the Mode Matching technique. This technique serves as a valuable tool for analyzing the scattering characteristics of structures involving partitioning and material property discontinuities. The Mode Matching solution elucidates the phenomena of reflection, transmission, and attenuation of planar mode excitation. The solution is projected onto the eigenfunctions, and information about the orthogonal properties is crucial for achieving a convergent solution. The eigenvalue problems with perfectly electric conducting boundary conditions exhibit eigenfunctions that satisfy usual orthogonality relations. However, the eigenvalue problems against impedance type conditions reveal that the eigenfunctions satisfy generalized orthogonality conditions.

The unique properties of plasma-filled waveguides make them valuable tools in various technological advancements across different fields, highlighting the relevance and significance of this research in driving innovation and development. The findings of this dissertation offer valuable insights into the practical implementation of electromagnetic wave behavior in waveguide structures, laying the foundation for prospective advancements in technology and various applications across different fields.

Contents

List of Figures

List of Tables

Abbreviations

Electromagnetic	**EM**
Mode Matching	**MM**
Perfectly Electric Conducting	**PEC**
Transverse Electric	**TE**
Transverse Electromagnetic	**TEM**
Transverse Magnetic	**TM**

Symbols

$\mathbf{E}$	Electric field intensity
$\mathbf{H}$	Magnetic field intensity
$\mathbf{D}$	Electric flux density
$\mathbf{B}$	Magnetic flux density
$\mathbf{J}$	Electric current density
$\mathbf{B}_0$	Direct magnetic field
ρ	Volume charge density
ϵ	Electric permittivity
μ	Magnetic permeability
σ	Conductivity of the medium
c	Speed of light
e	Electric charge
m	Electron mass
ω	Angular frequency
ω_p	Plasma frequency
n_p	Plasma density
ω_c	Cyclotron frequency
ω_b	Plasma beam frequency
n_b	Beam density

Chapter 1

General Introduction

1.1 Introduction

Plasma, a state of matter, is an electrically conducting quasi-neutral gas that consists of charged particles moving collectively. In addition to charged particles, plasma also contains molecules and photons across various wavelengths. Plasma is a significant component of the observable universe due to its prevalence in various environments. The motion of charged particles in plasma plays a crucial role in facilitating the propagation of electromagnetic (EM) waves. The magnetosphere of the Earth, a region of space influenced by Earth's magnetic field, is home to dense, cold plasma. This plasma interacts with EM waves, which serves as an essential source for radio communication. Cold plasma is classified as non-thermal because the electrons have significantly higher temperatures compared to ions and neutrals [1]. This medium, in which compression forces play an insignificant role [2], holds particular importance in biomedicine and healthcare. The cold plasma technology has emerged as a new and innovative approach in fighting cancer, due to the ability of cold plasma to eradicate cancer cells and activate specific signaling pathways essential for treatment responses [3]. In the food industry, this technology is emerging as a viable nonthermal processing method that reduces the necessity for prolonged microbial treatments and has the potential to supplant chemical disinfection techniques in the future [4]. Plasma treatment has been demonstrated as a fast, easy, and eco-friendly innovative approach for handling the catalytic materials, sparking the interest of numerous researchers. The treatment can facilitate the reduction, deposition, combination, and decomposition of active components in the preparation of catalytic materials [5]. Consequently, plasma technology has become an object of keen interest due to its manifoldness and low-cost production.

Waveguides are structures that guide the propagation of energy within a confined pathway. The alterations in their shape and material composition significantly influence the scattering of the energy within the pathway. A comparison of the properties of plasma waveguides and conventional dielectric waveguides reveals significant differences in many aspects. Plasma-filled rectangular waveguides are employed in laser-wakefield, a particle acceleration scheme, which has a potential application in physical sciences, radioisotope production, possible transmutation of nuclear waste, and generation of broad band X-ray radiation [6, 7]. The microwave-plasma interaction in these waveguides is viable in material processing, in controlled fusion and in active contact of radio waves with the ionosphere. Moreover, EM wave can be generated by injecting Cherenkov free electron laser within such type of waveguide [8]. Plasma-filled cylindrical waveguides are utilized in the conversion of methane into hydrogen or synthesis gas, which is crucial for the production of raw chemicals such as methanol and ammonia. Additionally, they serve as hydrogenation agents in oil refineries and play a role in reducing gases in the steel industry [9]-[10]. Additionally, these structures form integral parts of plasma jets, powerful microwave generators, accelerators in free electron lasers [11–13] and nuclear fusion equipment such as tokamaks and stellarators [14]. Additionally, plasma antennas utilizing ionized gas instead of metal-conducting components are highly efficient and require minimal power consumption [15]. An alternative structure is an infinite circular corrugated waveguide, which is easier to manufacture as compared to rectangular symmetry with corrugated walls [16]. The corrugated surface supports the backward wave, which makes it viable to be applied within a cylindrical structure as a backward-wave oscillator, a high-power microwave source at the centimeter and millimeter wavelength bands [17]. The use of electron beam in this wave structure results in generation of very high-power microwave pulses, which are widely applicable in ultra-precise radar systems and high-energy particle accelerators. Furthermore, the utilization of high-power microwave sources in a directed-energy weapon can result in permanent harm by emitting concentrated energy in a specific direction to disrupt or overwhelm electronic equipment [18].

1.2 Literature Review

The rectangular and cylindrical waveguides are uniform structures, characterized by cross sections transverse to the direction of propagation and almost identical in size and shape with each other. Therefore, the EM field within such waveguides can be presented as superposition of an infinite number of modes [19]. If the EM wave frequency delivered to the plasma surface is greater than the plasma frequency, the wave passes through it. However, if the frequency of the wave delivered to the plasma is lower than the plasma frequency, the wave does not pass through the plasma. Wait [20] elucidated that when a constant magnetic field is present, the dielectric constant of a plasma takes the form of a tensor. He provided detailed conclusions for the reflection coefficients of stratified plasma in both planar and cylindrical configurations.

Plasma waveguides have gained significant attention from researchers due to their potential in efficiently transferring EM energy [21]-[22]. Such waveguides have a significance in development of powerful microwave generators, in optical systems and in the progress of high-power millimeter wave amplifiers, high information density communication, as radiofrequency sources in accelerators for High Energy Physics, in reflective-type half-wave plate and for transmission control in quarter-wave plate and half-wave plate metallic and all-dielectric metasurfaces [23–27]. The importance of collective plasma effects in a hollow-core target for achieving collimation of injected electrons and the impact of the ion dynamics on a laser-driven electron acceleration are also investigated [28]-[29].

Malik et al. [30] focused on the Transverse Electric (TE) mode excited by a high intensity microwave in a lossless inhomogeneous unmagnetized plasma filled rectangular waveguide and observed that the electron density within the plasma changed linearly across the transverse direction of mode propagation. Sakhnenko et al. [31] gave analytical and numerical analysis of the EM fields of a circular cylinder of plasma with respect to time and spatial distribution. The investigation carried out by Gehre et al. [32] focused on the analysis of the scattering behavior of microwaves as they propagate through a circular waveguide that is partially filled with a uniform, lossless, and cold electron plasma. Kinderdijk and Hagebeuk [33] conducted a comparative analysis of various techniques for determining the propagation constant of the principal mode in a circular waveguide that contains a cold, cylindrically stratified plasma. A generalized problem for EM wave propagation, was discussed by Shahid et al. [34] in graphene-wrapped circular waveguides filled with magnetized plasma. The solution for the scattering of plane EM waves by a plasma-filled anisotropic sphere was derived by Geng et al. [35]. Achieving a multiscale property in a Janus metastructure is possible by utilizing the anisotropy of the plasma [36]. Researchers in the past have also examined the scattering of microwaves from a plasma column within a rectangular waveguide [37]-[38].

Analytical and numerical studies have been conducted on the dispersion properties of a cylindrical waveguide filled with plasma [39]. The theory of EM waves in cylindrical structures containing radially inhomogeneous plasma and plasma-dielectric fillings has also been presented in the past [40–43]. The more homogeneous layers are added within the cylinder, the higher the solution accuracy becomes, but this improvement comes at the cost of increased computation time when dealing with the problem of plane wave scattering from a magnetized, nonuniform, collisional, cold, and steady-state plasma cylinder [44]. After deriving the plasma dielectric tensor analytically, Khalil and Mousa [45] conducted investigations on the propagation of EM waves in a plasma-filled cylindrical waveguide. In order to determine plasma and collision frequencies in case of plasma or the dielectric constant and loss in case of dielectric, Thomassen [46] examined how a cylindrical plasma or dielectric column iteracts with a resonant cavity from which it extends. Manheimer [47] concluded that a long-wavelength electron plasma wave in a cylindrical waveguide steepens in the same manner as a nonlinear sound wave.

Strong magnetic fields are essential for the particle transport and propagation of laser pulses. The investigation carried out by Dawson and Oberma [48] explored the complexities of normal modes in a cold plasma slab and cylinder situated within a strong magnetic field. Electron acceleration and dynamics in plasma-filled rectangular, cylindrical, corrugated and elliptical waveguides have also drawn attention of the researchers [49–51]. Alekhina and Tyukhtin [52] studied features of the Cherenkov-Transition Radiation generated in the vacuum area of a circular waveguide partly filled with strongly magnetized plasma.

To investigate the impact of electron thermal velocity on the features of eigenmodes in a cylindrical waveguide, Aghamir and Abbas-nejad [53] gave the numerical solution of the dispersion relations for these modes. Investigations have also been carried out to study EM propagation behavior in plasma in the presence of magnetic field by changing plasma parameters and optimizing the incident angle and external magnetic field [54–56]. Intense lasers or particle beams [57] have a great application in producing large electric fields for accelerating particles. Therefore these beams, particularly plasma beams, are playing a pivotal role in advancement in astrophysics, in fabricating nanostructures [58] and in energy production.

Kobayashi et al. [59] conducted an investigation into the impact of plasma on the linear gain of a traveling wave tube featuring a helix-type interaction structure which supports Transverse Magnetic (TM) wave. The absorption of a high-power millimeter pulse in a waveguide comprising of plasma for a below critical density was established through simulations by Cao et el. [60]. Dvorak et al. [61] conducted a study on the propagation of an ultra-wide-band EM pulse in a uniform, cold plasma. Jazi et al. [62] conducted an analytical investigation into the reflection and absorption of a polarized wave in a magnetized plasma slab that is both inhomogeneous and dissipative.

Nusinovich et al. [63] reviewed the development of hybrid modes in a slow wave system containing plasma which results in the improvement of the coupling of the EM wave and plasma beam. The advantages of implementing the asymmetric as well as symmetric eigenmodes of a slow EM wave within a traveling-wave tube were discussed by Abubakirov et al. [64] in their paper. Carmel et al. [65] concluded that a high-power microwave pulse is generated in a corrugated wall waveguide or a cylindrical wave tube when a relativistic electron beam passes. The dispersion features of a similar wave structure along with a helix type slow wave structure were analyzed by Hong-Quan and Pu-Kun [66]-[67] for various geometric parameters and plasma densities. The relativistic traveling-wave tube and relativistic backward-wave oscillator work efficiently as amplifiers and high-power microwave sources. Bayat et al. [68] found an exact numerical solution of the dispersion relation of these structures when they contain plasma and are powered by an electron beam.

Various methods, both analytical and numerical, have been utilized to model the propagation of waves in isotropic and anisotropic cold plasma within a dielectric-filled metallic waveguide, for instance [69–82]. Galejs [83] developed a variational approach to analyze the impedance characteristics of a finite strip antenna, under the influence of a static magnet field, placed within a planar dielectric slab encompassed by a magnetoionic medium comprising cold electron plasma. Davies [84] employed a modified version of the Runge-Kutta method to examine how a transverse plasma velocity component affects the boundary layer structure at the interface between a plasma and a vacuum magnetic field. Leuterer and Derfler [85] examined the EM fields produced by a gap with azimuthal symmetry in a waveguide filled with cold plasma. The fields in the configuration space were determined through an inverse Fourier transform. Alekhina and Tyukhtin [86] applied the steepest descent method to obtain asymptotic expressions for the EM field in cold plasma and vacuum. In another research study, Li and Jiang [87] conducted an investigation on the characteristics of EM waves as they travel through magnetized plasma slabs and interact with plasma-coated spheres. They employed the discontinuous Galerkin finite-element time-domain method for their analysis. Mitsalas et al. [88] conducted investigation of a canonical problem involving a Transverse Electromagnetic (TEM) wave propagating within a parallel plate waveguide containing magnetized plasma by applying Weiner-Hopf technique. Simple approximate solutions for thin cylindrical antennas immersed in uniaxial resonant plasmas were obtained by Lee [89] by using an extension of the Wiener-Hopf technique. Maxwell's equations were solved numerically using the fourth-order Runge-Kutta method, by Abdoli-Arani [90] for the field amplitude of the microwave in a plasma-filled perfectly conducting waveguide. A modal solution was found by Nguyen [91] for the associated waveguide problem inside an infinite cylindrical antenna. Applying the finite-difference time-domain method, Chaohui et al. [92], numerically, made a three-dimensional model of a rectangular waveguide used as surface-wave plasma source. Ikuno et al. [93] used the meshless time domain method to evaluate the propagation of EM waves in various shaped waveguides.

Most of the above-mentioned analyses are focused on dispersion properties of rectangular and cylindrical structures or on achieving simple solutions. The propagation of power and the validation of the truncated solution were some prominent features that needed to be addressed. The problems discussed in this dissertation involve EM wave scattering in rectangular/ cylindrical waveguides containing unmagnetized/strongly magnetized cold plasma environment. Choosing a rectangular or cylindrical structure involves overcoming several challenges. One of the primary difficulties is the selection of an appropriate technique for dealing with geometric partitioning, material property variations, and bounding characteristics. Calculating roots of characteristic equations by applying an appropriate guess in a suitable method and constructing orthogonality relations are also complex tasks. The straightforward part of these configurations is the calculation of eigenvalues through Helmholtz equation and boundary conditions. The main objective of our investigation was to introduce an analytical framework and conduct a mathematical analysis of the problems under discussion.

The Mode Matching (MM) method has recently advanced in various directions not only to investigate the scattering of EM waves but also to analyze the acoustic wave scattering at structural discontinuities, for instance, see [94–97]. The application of MM methods to analyze the EM scattering characteristics of various configurations can be found in [98–105]. Najari et al. [106] applied MM technique to probe into the EM wave propagation in a semi-bounded plasma from a lossless isotropic cylindrical waveguide with metallic walls. Abdoli-Arani and Moghaddasi [107] studied the acceleration of an electron injected inside a cylindrical waveguide having collisional plasma, using MM technique. Gashturi et al. [108] suggested the employment of a combination of method of moments and the MM technique to numerically simulate the components of waveguides including the cavity resonators. Efficient MM and hybrid MM/numerical EM waveguide building blocks have been applied for the optimized usage of powerful circuit computer-aided design tools and waveguide components [109]. The MM technique has also been applied in calculations for the resonator of gyro-devices [110]. The resonators are widely exploited in the gyro-oscillators and amplifiers. Due to the recognition for its ability to conserve power balance, meet eigen properties as outlined by Lawrie [111, 112], align tangential electric and magnetic fields even when facing corners, and exhibit strong contrast for both fundamental mode forcing, the research methodology adopted in this dissertation involved employing a MM solution approach. Although, numerical techniques like finite element method or boundary element method allow for the study of finite-length conduits of any shape or size, however, as the excitation frequency and waveguide dimensions increase, the complexity of the problem grows rapidly due to the escalating number of degrees of freedom. In the context of guiding structures, MM is a rapid and convergent technique that can be easily implemented without the need for discretization of variables. It offers an exact solution to EM scattering challenges in various structures, including discontinuous, planar, and periodic ones [113]. This method involves matching modes at different sections of the conduit to analyze the behavior of EM wave scattering.

1.3 Objective and Physical Problems

The study presented in this dissertation is committed to a brief discussion on the scattering characteristics and power propagation of EM waves through cold plasma and beam in wave structures with various geometries and discontinuities. This topic has drawn the attention of the researchers due to the growing involvement of plasma in a variety of applications. The semi-analytic MM technique is invoked to handle this category of the problems. The dissertation covers the below-mentioned physical problems:

1. The EM wave propagation in discontinuous waveguide containing plasma.

2. Cold plasma-induced effects on EM wave scattering in waveguides: An MM analysis.

3. Exploring scattering in a cylindrical duct with plasma between vacuum and dielectric layers.

4. EM wave scattering in plasma beam driven waveguides under strong magnetic field.

5. TM wave scattering in a cylindrical waveguide with a central chamber containing beam-plasma environment.

1.4 Outline of the Dissertation

The dissertation outlines are as follows.

Chapter 2: The chapter on preliminaries institutes some basic definitions and notions that are necessary to comprehend the work presented in the subsequent chapters.

Chapter 3: This chapter comprises the scattering of EM waves encountering plasma medium and step-discontinuities. The study's physical model comprises dielectric and plasma layers separated by metallic conducting material in the form of horizontal plates. The MM method is employed to address the issue at hand. This method works by projecting the solution onto an orthogonal basis. Through this process, it becomes possible to elucidate how planar mode excitation behaves in terms of reflection, transmission, and attenuation. The precision of algebraic manipulation and solution scheme utilized is confirmed by the mathematical and intrinsic power analyses. The investigation offers insights into both the mathematical and theoretical aspects of the structure being examined. The contents of this investigation are published in the journal Waves in Random and Complex Media. The analyses in this chapter also include the examination of how EM waves scatter when interacting with a plasma slab. This slab can either be enclosed between Perfectly Electric Conducting (PEC) plates or situated within a dielectric medium. The MM method is once again utilized to solve the problem, and the accuracy of this approach is confirmed through numerical evaluations that involve verifying the cogency of matching conditions and power conservation. The study emphasizes the influence of variations in geometry and materials on the reflection and transmission phenomena within the waveguide. An article based on this study is published in Communications in Theoretical Physics journal.

Chapter 4: This chapter includes the propagation of EM waves in a cylindrical PEC waveguide with a central chamber filled with cold plasma embedded in vacuum which is covered by dielectric layer in conducting cylinder. The mathematical modeling formulates a boundary value problem which is solved by using the MM technique to analyze the scattering characteristics. The efficacy of the truncated solution is exhibited by verifying the matching conditions. The investigation focuses on the power flux in different regions of the waveguide, considering both transparency and non-transparency regimes. Computational results demonstrate energy propagation against the properties of the medium and geometrical parameters of configuration. It is found that the plasma radius alterations do not significantly affect transmission, but influence the number of cut-on modes in transparency regime. The contents of this chapter are submitted in the journal Optical and Quantum Electronics for possible publication.

Chapter 5: The scattering of EM wave in a cold and uniform plasma-filled waveguide driven by an intense relativistic electron beam under a strong magnetic field is probed in this chapter. The Helmholtz equation portrays the boundary value problem which is solved by incorporating the MM technique. Invoking the boundary and matching conditions and the derived orthogonality and dispersion relations in this scheme gives an exact solution to the scattering problem. The numerical results shed light on the occurrence of reflection and transmission and flow of power. The power flux is plotted against angular frequency and various duct configurations. The solution is substantiated altogether through the befitting analytical and numerical results. The investigation of this structure reveals not only its mathematical but also the physical features. The EM wave scattering in a beam-plasma configuration, enclosed within a central chamber of an infinite cylindrical waveguide, is also meticulously analyzed using the MM technique. This technique provides an exact solution that is validated through the verification of matching conditions. Furthermore, the investigation into the power flux behavior versus angular frequency is carried out.

Chapter 6: In this chapter, a comprehensive summary of the scattering problems that were discussed throughout the research is provided. Moreover, the conclusion drawn from the analysis and the interpretation of the scattering data is also presented in chapter 6. Additionally, this chapter delves into future directions for research in this field based on the insights gained from the study of the scattering problems.

Chapter 2

Preliminaries

This chapter renders the fundamental concepts that are indispensable to understand the propagation and scattering of EM wave in waveguides with step discontinuities and having different material mediums. The EM scattering problems are governed by Maxwell's equations and different types of boundary conditions. Derived from Maxwell's equations, the Helmholtz equation depicts the propagation of EM waves. This equation along with the boundary conditions generates the eigenfunctions that are linearly dependent and satisfy the usual or generalized orthogonality relations. The orthogonality relations help to transform the system of differential equations into linear algebraic system during the matching analysis which is discussed in ongoing chapters of the dissertation.

Waveguides are structures that confine and direct the propagation of waves. Being single conductors with no current source, waveguide is a specialized form of transmission line that is extensively employed to direct EM waves from one location to another. The TEM mode propagates in presence of two conductors, one of which is the current source. This concludes that only TE and TM waves can propagate in a waveguide. More precisely, when an EM wave propagates through a hollow cylindrical or rectangular waveguide, either the electric field or the magnetic field will be transverse to the direction of the wave. The EM waves are formed when electric and magnetic fields come in contact with each other and produce vibrations, with both fields perpendicular to each other.

2.1 Maxwell's Equations

James Clark Maxwell was the first scientist who explained the correlation between electricity and magnetism in the form of equations. Listed below, these equations provide the relationship of electric and magnetic fields with each other as well as with electric and magnetic charges and currents.

$$\nabla \times \tilde{\mathbf{E}} = -\frac{\partial \tilde{\mathbf{B}}}{\partial t}, \tag{2.1}$$

$$\nabla \times \tilde{\mathbf{H}} = \tilde{\mathbf{J}} + \frac{\partial \tilde{\mathbf{D}}}{\partial t}, \tag{2.2}$$

$$\nabla . \tilde{\mathbf{D}} = \rho, \tag{2.3}$$

$$\nabla . \tilde{\mathbf{B}} = 0, \tag{2.4}$$

where, $\tilde{\mathbf{E}} = \mathbf{E}(r)e^{-i\omega t}$ and $\tilde{\mathbf{H}} = \mathbf{H}(r)e^{-i\omega t}$ are the time-dependent electric and magnetic field intensities, $\tilde{\mathbf{D}} = \mathbf{D}(r)e^{-i\omega t}$ and $\tilde{\mathbf{B}} = \mathbf{B}(r)e^{-i\omega t}$ are the electric and magnetic flux densities, while ρ denotes the volume charge density and $\tilde{\mathbf{J}}$ represents electric current density. All quantities stated in these equations are vectors except ρ.

The equations (2.1)-(2.4) are the respective representations of Faraday's law, Ampere's law, Gauss's law and magnetic Gauss's law. Note that we have assumed harmonic dependence of $e^{-i\omega t}$ which is suppressed throughout this dissertation [114]. The Maxwell's equations in time harmonic form can now be written as follows:

$$\nabla \times \mathbf{E} = i\omega \mathbf{B}, \tag{2.5}$$

$$\nabla \times \mathbf{H} = \mathbf{J} - i\omega \mathbf{D}, \tag{2.6}$$

$$\nabla . \mathbf{D} = \rho, \tag{2.7}$$

$$\nabla . \mathbf{B} = 0. \tag{2.8}$$

In a source-free region ρ and $\mathbf{J}$ are zero. Throughout this dissertation, the analyses are carried out in source-free regions, therefore the EM propagation will be governed by Maxwell's equations 2.5 and 2.6.

2.2 Constitutive Relations and Wave Equations

To link the densities with fields, we may assume some material medium. The constitutive relations express the interconnection between the medium and the EM field in terms of material parameters. Following types of material mediums are considered in this dissertation:

- Dielectric Medium,
- Plasma medium.

2.2.1 Dielectric Medium

Dielectrics are poor conductors of electricity. William Whewell introduced the term dielectric by merging the words ‘dia’ and ‘electric’ on request of Michael Faraday. The constitutive relations for a dielectric medium are stated as follows:

$$\mathbf{D} = \epsilon_d \mathbf{E}, \tag{2.9}$$

$$\mathbf{B} = \mu_0 \mathbf{H}, \tag{2.10}$$

$$\mathbf{J} = \sigma \mathbf{E}, \tag{2.11}$$

where ϵ_d is the permittivity constant in dielectric medium which is some non-zero multiple of the permittivity ϵ_0 of free space, which is approximated to be $\epsilon_0 = 8.8542 \times 10^{-12}$ F/m (Farads per meter). The magnetic permeability of free space μ_0 has the approximate value $\mu_0 = 4\,\pi \times 10^{-7}$ N/A^2 (Newtons per Ampere squared). The parameter σ is the conductivity of the medium and (2.11) depicts the Ohm’s law. The magnetic permeability is assumed to be of free space and permittivity is either in the form of constant or a tensor in all the mediums discussed in this dissertation. Consequently, the Faraday’s law remains invariant but the Ampere’s law behaves differently in these mediums. The Faraday’s law and Ampere’s law together give rise to the Helmholtz or wave equation which portrays the propagation of EM waves in a material medium. Applying the constitutive relation (2.9), the dielectrics are governed by Faraday's law and Ampere's law in following manner:

$$\nabla \times \mathbf{E} = i\omega \mathbf{B}, \tag{2.12}$$

$$\nabla \times \mathbf{H} = -i\omega\epsilon_d \mathbf{E}. \tag{2.13}$$

Multiplying (2.13) throughout by μ_0 produces

$$\nabla \times \mathbf{B} = -i\omega\epsilon_d\mu_0 \mathbf{E}. \tag{2.14}$$

Taking curl of (2.12), we obtain

$$\nabla \times \nabla \times \mathbf{E} = i\omega \nabla \times \mathbf{B}. \tag{2.15}$$

Substituting $\nabla \times \mathbf{B}$ in (2.15) yields

$$\nabla \times \nabla \times \mathbf{E} = \omega^2\epsilon_d\mu_0 \mathbf{E}. \tag{2.16}$$

Applying the vector equation

$$\nabla \times \nabla \times \mathbf{E} = -\nabla^2 \mathbf{E} + \nabla(\nabla.\mathbf{E}),$$

remolds (2.16) in the following manner:

$$-\nabla^2 \mathbf{E} + \nabla(\nabla.\mathbf{E}) = \omega^2\epsilon_d\mu_0 \mathbf{E}. \tag{2.17}$$

The Gauss's Law in a source-free region implies $\nabla.\mathbf{E} = 0$. Therefore, (2.17) reduces to the wave equation of TM mode in the dielectric medium in the following way:

$$\left(\nabla^2 + \omega^2\epsilon_d\mu_0\right) \mathbf{E} = 0. \tag{2.18}$$

Taking curl of (2.14) and solving in a similar manner generates the wave equation for TE modes in the dielectric medium as:

$$\left(\nabla^2 + \omega^2\epsilon_d\mu_0\right) \mathbf{B} = 0. \tag{2.19}$$

The equations (2.18) and (2.19) are known as Helmholtz equations and can be collectively written as follows:

$$\left(\nabla^2 + \omega^2 \epsilon_d \mu_0\right) \begin{pmatrix} \mathbf{E} \\ \mathbf{B} \end{pmatrix} = \begin{pmatrix} 0 \\ 0 \end{pmatrix}. \tag{2.20}$$

The solution to the above wave equation can be obtained by assuming an electric or magnetic field uniform in the z direction. Thus, the Helmholtz equation (2.20) reduces to

$$\left(\nabla^2 + \omega^2 \epsilon_d \mu_0\right) \begin{pmatrix} E_z \\ B_z \end{pmatrix} = \begin{pmatrix} 0 \\ 0 \end{pmatrix}. \tag{2.21}$$

For vacuum, the relations (2.10) and (2.11) remain unchanged, while (2.9) is transformed as follows,

$$\mathbf{D} = \epsilon_0 \mathbf{E}. \tag{2.22}$$

The wavenumber of the vacuum is stated as $\omega\sqrt{\epsilon_0 \mu_0}$. As the speed of light c is associated with permeability and permittivity of free space or vacuum by the relation $c = 1/\sqrt{\epsilon_0 \mu_0}$, therefore the wavenumber of vacuum can be recast as ω/c. Thus, replacing ϵ_d by ϵ_0 in (2.13) and following the same procedure as was applied for dielectric medium, the wave equation for vacuum can be expressed as:

$$\left(\nabla^2 + \frac{\omega^2}{c^2}\right) \begin{pmatrix} E_z \\ B_z \end{pmatrix} = \begin{pmatrix} 0 \\ 0 \end{pmatrix}. \tag{2.23}$$

2.2.2 Plasma Medium

Gyroelectric or gyromagnetic materials are those that exhibit susceptibility to changes when subjected to a quasistatic magnetic field. The permittivity tensor $\overline{\epsilon}$ of "dielectric" (or gyroelectric) materials can be altered by an externally applied magnetic field. Moreover, such a magnetic field causes a change in the permeability tensor $\overline{\mu}$ in the case of ferrites (or gyromagnetic materials). In waveguides comprising gyroelectric materials, it is typically assumed that waves propagate along the z-axis. Consider a cold plasma medium subjected to a direct magnetic field $\mathbf{B}_0$ along longitudinal direction and containing induced current $\mathbf{J}$. The constitutive relations in plasma are given as

$$\mathbf{D} = \epsilon_0 \bar{\epsilon}_j \mathbf{E}, \tag{2.24}$$

$$\mathbf{B} = \mu_0 \mathbf{H}, \tag{2.25}$$

$$\mathbf{J} = \sigma \mathbf{E}. \tag{2.26}$$

The Maxwell's equations for plasma medium can be stated as:

$$\nabla \times \mathbf{E} = i\omega \mathbf{B}, \tag{2.27}$$

$$\nabla \times \mathbf{B} = -\frac{i\omega}{c^2} \bar{\epsilon}_j . \mathbf{E}, \tag{2.28}$$

where $j = p, b$ stand for cold plasma and beam, respectively. The permittivity tensor $\bar{\epsilon}_j$ can be expressed [115], as

$$\bar{\epsilon}_p = \begin{bmatrix} \epsilon_1 & -i\epsilon_2 & 0 \\ i\epsilon_2 & \epsilon_1 & 0 \\ 0 & 0 & \epsilon_{3j} \end{bmatrix}. \tag{2.29}$$

The tensor components ϵ_1 and ϵ_2 are determined by analyzing the properties of EM fields in an anisotropic medium, and are same for both cold plasma and beam stated as

$$\epsilon_1 = 1 - \frac{\omega_p^2}{\omega^2 - \omega_c^2}, \quad \epsilon_2 = \frac{\omega_c \omega_p^2}{\omega \left(\omega^2 - \omega_c^2\right)},$$

while the component ϵ_{3j} ; $j = p, b$ can be expressed for the two mediums as

$$\epsilon_{3p} = 1 - \frac{\omega_p^2}{\omega^2}$$

and

$$\epsilon_{3b} = 1 - \frac{\omega_p^2}{\omega^2} - \frac{\omega_b^2}{\gamma^3 (\omega - k_{nz} v)^2}.$$

Here e, n_p, n_b, m represent the electric charge, plasma density, beam density, and electron mass, while ω_c, ω_p and ω_b reveal the cyclotron, plasma and beam frequencies, respectively [116]. The quantity γ is the relativistic factor and v is the electron beam velocity, such that $\gamma = \sqrt{1 - \dfrac{v^2}{c^2}}$. The frequencies ω_c, ω_p and ω_b can further be explained as follows,

$$\omega_c = \frac{|e|\mu_0 B_0}{m}, \qquad \omega_p = \left(\frac{e^2 n_p}{\epsilon_0 m}\right)^{1/2}, \qquad \omega_b = \left(\frac{e^2 n_b}{\epsilon_0 m}\right)^{1/2},$$

where B_0 reveals the magnitude of the direct magnetic field.

2.2.2.1 Cold Plasma

Cold plasma is a material medium constituting high-temperature but low density electrons at room temperature and pressure, which supports the propagation of EM waves.

Case I: Absence of Magnetic Field; $B_0 = 0$

In absence of magnetic field, i.e., $B_0 = 0$ the plasma behaves as unmagnetized and $\omega_c = 0$. The permittivity tensor $\bar{\epsilon}_p$ takes the form

$$\bar{\epsilon}_p = \begin{bmatrix} \epsilon_{3p} & 0 & 0 \\ 0 & \epsilon_{3p} & 0 \\ 0 & 0 & \epsilon_{3p} \end{bmatrix}. \tag{2.30}$$

Taking curl of z-component in Faraday's law in (2.27), we have

$$(\nabla \times \nabla \times \mathbf{E})_z = i\omega(\nabla \times \mathbf{B})_z. \tag{2.31}$$

Substituting $(\nabla \times \mathbf{B})_z$ in (2.31) yields

$$(\nabla \times \nabla \times \mathbf{E})_z = \frac{\omega^2}{c^2}\epsilon_{3p}\mathbf{E}_z. \tag{2.32}$$

Invoking the vector equation

$$(\nabla \times \nabla \times \mathbf{E})_z = -\nabla^2\mathbf{E}_z + (\nabla(\nabla.\mathbf{E}))_z\,,$$

reforms (2.32) in the following way:

$$-\nabla^2\mathbf{E}_z + (\nabla(\nabla.\mathbf{E}))_z = \frac{\omega^2}{c^2}\epsilon_{3p}\mathbf{E}_z. \tag{2.33}$$

The Gauss's Law in a source-free region indicates $(\nabla.\mathbf{E})_z = 0$. Therefore, (2.33) reduces to the wave equation of TM mode in the cold plasma as:

$$\left(\nabla^2\mathbf{E}_z + \frac{\omega^2}{c^2}\epsilon_{3p}\right)\mathbf{E}_z = 0. \tag{2.34}$$

The wave equation of TE mode can be evaluated in a similar way by considering longitudinal component of magnetic field $\mathbf{B}$.

Hence, the Helmholtz equation for cold unmagnetized plasma, in the form of longitudinal components of fields [117], is expressed as

$$\left\{\nabla^2 + \frac{\omega^2}{c^2}\left(1 - \frac{\omega_p^2}{\omega^2}\right)\right\}\begin{pmatrix} E_z \\ B_z \end{pmatrix} = \begin{pmatrix} 0 \\ 0 \end{pmatrix}. \tag{2.35}$$

Case II: Presence of Strong Magnetic Field; $B_0 \to \infty$

When a strong magnetic field is present, the coupling of TE and TM modes cannot be formed and the tensor component $|\epsilon_2|$ is negligibly small and $\epsilon_1 = 1$ [118]. The permittivity tensor $\bar{\epsilon}_p$ takes the form

$$\bar{\epsilon} = \begin{bmatrix} 1 & 0 & 0 \\ 0 & 1 & 0 \\ 0 & 0 & \epsilon_{3p} \end{bmatrix}. \tag{2.36}$$

The Helmholtz equation becomes

$$(\nabla^2 + T_1^2)\begin{pmatrix} E_z \\ B_z \end{pmatrix} = \begin{pmatrix} 0 \\ 0 \end{pmatrix}, \tag{2.37}$$

where $T_1^2 = \left(\frac{\omega^2}{c^2} - k_{nz}^2\right)\left(1 - \frac{\omega_p^2}{\omega^2}\right)$ and $k_{nz} = \frac{\omega}{c} + 2n\pi;\ n = 0, 1, 2, \ldots$ is the axial wavenumber.

2.2.2.2 Plasma Beam

A plasma beam passing through a plasma-filled waveguide and a strong external magnetic field are considered as the mechanisms for controlling the field attenuation and strength of the waveguide. Therefore, the EM wave propagation in beam-plasma environment under the influence of a strong external magnetic field is discussed in this dissertation. Adopting the procedure as was applied for cold plasma in presence of strong magnetic field, the Helmholtz equation is expressed, in longitudinal components of fields, as

$$\left(\nabla^2 + T_2^2\right)\begin{pmatrix} E_z \\ B_z \end{pmatrix} = \begin{pmatrix} 0 \\ 0 \end{pmatrix}, \tag{2.38}$$

such that $T_2^2 = \left(\dfrac{\omega^2}{c^2} - k_{nz}^2\right)\left(1 - \dfrac{\omega_p^2}{\omega^2} - \dfrac{\omega_b^2}{\gamma^3(\omega - k_{nz}v)^2}\right)$.

2.3 Boundary Conditions

With a view to solve Maxwell's equations in a closed or bounded region, a set of boundary conditions is required. These conditions help us analyze the behavior of fields at interfaces and boundaries joining various media. By using waveguides, the energy loss during propagation can be avoided.

Let $(\mathbf{E}_1, \mathbf{H}_1)$ and $(\mathbf{E}_2, \mathbf{H}_2)$ be the respective electric and magnetic fields of two mediums namely Ω_1 and Ω_2 and $\boldsymbol{n}$ be the unit vector with respect to medium Ω_1, normal to the boundary $\partial\Omega$.

2.3.1 PEC Boundary Conditions

If the second medium is perfectly conducting then it offers zero electrical resistance ($\mathbf{E} = 0$ in Ω_2). Moreover, any magnetic field must be constant in time, i.e., $\dfrac{\partial \mathbf{H}}{\partial t} = 0$ in Ω_2. The magnetic field is zero, $\mathbf{H} = 0$ in Ω_2 in a source-free region. According to Maxwell's equations, the normal component of magnetic field and the tangential component of electric field exhibit continuity throughout the boundary $\partial\Omega$. Mathematically, these conditions imply

$$(\mathbf{E} \times \boldsymbol{n})\,|_{\partial\Omega} = 0, \tag{2.39}$$

$$(\mathbf{H} \cdot \boldsymbol{n})\,|_{\partial\Omega} = 0. \tag{2.40}$$

2.3.2 Interface Conditions

Once it is established that the medium Ω_2 supports the EM fields, the boundary $\partial\Omega$ becomes the interface.

In case of TM wave, the continuity conditions at interface are stated as

$$(E_{z2} - E_{z1})|_{\partial\Omega} = 0, \tag{2.41}$$

$$\left(\left(\frac{1}{\mu_2}\nabla E_{z2} - \frac{1}{\mu_1}\nabla E_{z1}\right) \cdot \boldsymbol{n}\right)\Big|_{\partial\Omega} = 0. \tag{2.42}$$

If the wave propagates in TE mode, the continuity conditions at interface are stated as

$$(H_{z2} - H_{z1})|_{\partial\Omega} = 0, \tag{2.43}$$

$$\left(\left(\frac{1}{\epsilon_2}\nabla H_{z2} - \frac{1}{\epsilon_1}\nabla H_{z1}\right) \cdot \boldsymbol{n}\right)\Big|_{\partial\Omega} = 0, \tag{2.44}$$

where ϵ_1 and μ_1 represent the permittivity and permeability in Ω_1 while ϵ_2 and μ_2 indicate the permittivity and permeability in Ω_2.

2.4 EM Wave Propagation in Waveguides

The present dissertation is focused on the scattering characteristics of waveguides containing different mediums and geometric properties. Rectangular and cylindrical types of configurations have been, specifically, discussed. It is possible to rewrite the Helmholtz equation in six scalar equations using rectangular or cylindrical coordinates. All these scalar equations will yield the components of EM waves in any medium. In case of plane waves, not all the six components of EM fields are considered. It has been widely observed in the literature that the propagation of a plane EM wave is considered for analysis. It is due to the fact that with increase in components, only the complexity of the problem increases while physical features remain same. The longitudinal and transverse components of fields in given configurations for TE and TM modes are briefly expressed in next sections.

2.4.1 EM Fields in Rectangular Coordinate System

Maxwell's equations subject to prescribed boundary conditions are solved to ascertain the guided waves. Let us consider waves directed along the z-direction in a medium whose wavenumber is given as $k = \omega\sqrt{\epsilon\mu_0}$. These waves indicate a z-dependence $e^{ik_z z}$ and their field components are written as $E(x, y, z) = \tilde{E}(x, y)e^{ik_z z}$ and $B(x, y, z) = \tilde{B}(x, y)e^{ik_z z}$. For a two dimensional waveguide, the EM fields are decomposed into longitudinal components E_z and B_z and transverse components E_x, E_y, B_x and B_y. The components of electric and magnetic fields for different mediums will now be determined through Maxwell's equations (2.5) and (2.6) after decomposition into six scalar equations as follows:

$$\frac{\partial E_z}{\partial y} - ik_z E_y = i\omega B_x, \tag{2.45}$$

$$-\frac{\partial E_z}{\partial x} + ik_z E_x = i\omega B_y, \tag{2.46}$$

$$\frac{\partial E_y}{\partial x} - \frac{\partial E_x}{\partial y} = i\omega B_z, \tag{2.47}$$

$$\frac{\partial B_z}{\partial y} - ik_z B_y = -i\omega\epsilon\mu_0 E_x, \tag{2.48}$$

$$-\frac{\partial B_z}{\partial x} + ik_z B_x = -i\omega\epsilon\mu_0 E_y, \tag{2.49}$$

$$\frac{\partial B_y}{\partial x} - \frac{\partial B_x}{\partial y} = -i\omega\epsilon\mu_0 E_z. \tag{2.50}$$

All the transverse components are determined in terms of longitudinal components. For example E_x can be evaluated by exploiting (2.46) and (2.48). In this way we

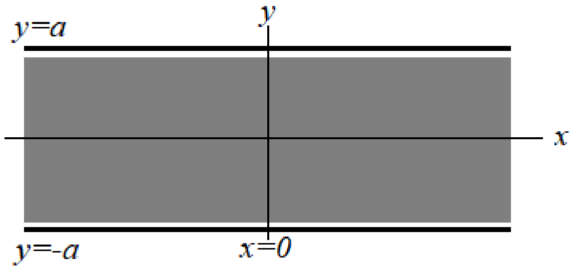

FIGURE 2.1: A two dimensional infinite rectangular waveguide with duct height $2a$.

can determine all four transverse components stated as:

$$E_x = \frac{1}{k^2 - k_z^2}\left(ik_z\frac{\partial E_z}{\partial x} + i\omega\frac{\partial B_z}{\partial y}\right), \quad E_y = \frac{1}{k^2 - k_z^2}\left(ik_z\frac{\partial E_z}{\partial y} - i\omega\frac{\partial B_z}{\partial x}\right),$$

$$B_x = \frac{1}{k^2 - k_z^2}\left(-\frac{ik^2}{\omega}\frac{\partial E_z}{\partial y} + ik_z\frac{\partial B_z}{\partial x}\right), \quad B_y = \frac{1}{k^2 - k_z^2}\left(\frac{ik^2}{\omega}\frac{\partial E_z}{\partial x} + ik_z\frac{\partial B_z}{\partial y}\right).$$

As the waveguides support propagation of EM waves in TE and TM modes only, so the transverse components of fields will be discussed for these two cases.

2.4.2 TE Wave

If the EM wave is propagating in TE mode, then the component of electric field in the direction of propagation is zero, i. e., $E_z = 0$. The transverse components of fields can be stated as

$$E_x = \frac{i\omega}{k^2 - k_z^2}\frac{\partial B_z}{\partial y}, \quad E_y = -\frac{i\omega}{k^2 - k_z^2}\frac{\partial B_z}{\partial x},$$

$$B_x = \frac{ik_z}{k^2 - k_z^2}\frac{\partial B_z}{\partial x}, \quad B_y = \frac{ik_z}{k^2 - k_z^2}\frac{\partial B_z}{\partial y}.$$

2.4.3 TM Wave

In case of a TM wave, the components of magnetic field are perpendicular to the direction of propagation, i. e., $B_z = 0$. The transverse components can be determined by utilizing the details from the longitudinal components in the following manner:

$$E_x = \frac{ik_z}{k^2 - k_z^2}\frac{\partial E_z}{\partial x}, \quad E_y = \frac{ik_z}{k^2 - k_z^2}\frac{\partial E_z}{\partial y},$$

$$B_x = -\frac{ik^2}{\omega(k^2 - k_z^2)}\frac{\partial E_z}{\partial y}, \quad B_y = \frac{ik^2}{\omega(k^2 - k_z^2)}\frac{\partial E_z}{\partial x}.$$

2.4.4 EM Fields in a Two Dimensional Rectangular Waveguide

An appropriate representation of wave propagation in real situations is a plane wave.

Considering a plane wave not only saves time and effort but gives an accurate analysis of the related EM wave problem without damaging its physical properties.

Therefore, in this dissertation a plane wave will be considered while investigating the waveguide problems. The Helmholtz equation for a plane wave propagating in a two dimensional waveguide ($\partial/\partial z = 0$) can be described as

$$\left(\frac{\partial^2}{\partial x^2} + \frac{\partial^2}{\partial y^2} + k^2\right)\begin{pmatrix} E_z \\ B_z \end{pmatrix} = \begin{pmatrix} 0 \\ 0 \end{pmatrix}. \tag{2.51}$$

The transverse components of fields can be listed as,

$$E_x = \frac{i\omega}{k^2}\frac{\partial B_z}{\partial y}, \quad E_y = -\frac{i\omega}{k^2}\frac{\partial B_z}{\partial x},$$

$$B_x = -\frac{i}{\omega}\frac{\partial E_z}{\partial y}, \quad B_y = \frac{i}{\omega}\frac{\partial E_z}{\partial x}.$$

The transformation of the electric and magnetic field components occurs differently for TE and TM waves. The transverse components of fields in the case of a TE wave are

$$E_x = \frac{i\omega}{k^2}\frac{\partial B_z}{\partial y}, \quad E_y = -\frac{i\omega}{k^2}\frac{\partial B_z}{\partial x},$$

$$B_x = 0, \quad B_y = 0,$$

while in the case of a TM wave, the transverse components are given as

$$E_x = 0, \quad E_y = 0,$$

$$B_x = -\frac{i}{\omega}\frac{\partial E_z}{\partial y}, \quad B_y = \frac{i}{\omega}\frac{\partial E_z}{\partial x}.$$

In the form of harmonic time dependence field potential ϕ, the Helmholtz equation for a uniform plane wave can be expressed as

$$\left(\frac{\partial^2}{\partial x^2} + \frac{\partial^2}{\partial y^2} + k^2\right)\phi = 0. \tag{2.52}$$

The solution of this Helmholtz equation (2.52) by variable separable technique is known as traveling wave solution that can be expressed as

$$\phi(x, y) = \sum_{n=0}^{\infty} \mathcal{B}_n Y_n e^{\pm i s_n x}, \tag{2.53}$$

where $Y_n(y); n = 0, 1, 2, \ldots$ represent the eigenfunction expansions, $\mathcal{B}_n$ are the amplitudes and s_n represent the wavenumber of nth mode. With reference to Section 2.3, the boundary condition for a perfectly conducting wall is stated as

$$\frac{\partial \phi}{\partial y} = 0. \tag{2.54}$$

2.4.5 Orthogonality Relation

The physical problems considered in this dissertation are dealt with by using MM technique. In order to implement this technique, the orthogonal features of the aforementioned eigenfunctions are employed.

Let us consider a duct $0 \leq y \leq b$ bounded between PEC walls at $y = 0$ and $y = b$. The boundary at $y = a$ separates the two material mediums. The eigenfunctions $Y_n(y)$ in these mediums can be expressed as

$$Y_n(y) = \begin{cases} Y_{1n}(y), & 0 \leq y \leq a, \\ Y_{2n}(y), & a \leq y \leq b. \end{cases} \tag{2.55}$$

The eigen-sub-systems can be formed as

$$Y_{1n}^{''}(y) - \tau_n^2 Y_{1n}(y) = 0, \tag{2.56}$$

$$Y_{2n}^{''}(y) - \gamma_n^2 Y_{2n}(y) = 0, \tag{2.57}$$

$$Y_{1n}^{'}(0) = 0 = Y_{2n}^{'}(b), \tag{2.58}$$

$$Y_{1n}(a) = Y_{2n}(a), \tag{2.59}$$

$$\eta_1 Y_{1n}^{'}(a) = \eta_2 Y_{2n}^{'}(a). \tag{2.60}$$

The quantities τ_n and γ_n can be revealed as $\tau_n^2 = k_1^2 - s_n^2$ and $\gamma_n^2 = k_2^2 - s_n^2$; $n = 0, 1, 2, \ldots$ where k_1 and k_2 are the wavenumbers of the two mediums.

The respective impedances of these mediums are represented as η_1 and η_2.

Multiplying equation (2.56) by $Y_{1m}(y)$ and integrating from 0 to a,

$$\int_0^a Y_{1n}^{''}(y) Y_{1m}(y) dy = \tau_n^2 \int_0^a Y_{1n}(y) Y_{1m}(y) dy. \tag{2.61}$$

Applying the integration by parts of the left hand side of (2.61) and employing condition (2.58), we obtain

$$\begin{aligned}\int_0^a Y_{1n}^{''}(y) Y_{1m}(y) dy &= \Big[Y_{1n}^{'}(y) Y_{1m}(y)\Big]_0^a - \Big[Y_{1n}(y) Y_{1m}^{'}(y)\Big]_0^a + \int_0^a Y_{1m}^{''}(y) Y_{1n}(y) dy \\ &= Y_{1n}^{'}(a) Y_{1m}(a) - Y_{1n}(a) Y_{1m}^{'}(a) + \tau_m^2 \int_0^a Y_{1n}(y) Y_{1m}(y) dy.\end{aligned} \tag{2.62}$$

Substituting (2.62) in (2.61) results in

$$(\tau_n^2 - \tau_m^2) \int_0^a Y_{1n}(y) Y_{1m}(y) dy = Y_{1n}^{'}(a) Y_{1m}(a) - Y_{1n}(a) Y_{1m}^{\prime}(a), \tag{2.63}$$

which can be further transformed by using the given correlation of τ_n with s_n

$$(s_n^2 - s_m^2) \int_0^a Y_{1n}(y) Y_{1m}(y) dy = Y_{1n}^{'}(a) Y_{1m}(a) - Y_{1n}(a) Y_{1m}^{\prime}(a). \tag{2.64}$$

Solving in a similar manner, (2.57) leads to the formation of the following equation

$$(s_n^2 - s_m^2) \int_a^b Y_{2n}(y) Y_{2m}(y) dy = -Y_{2n}^{'}(a) Y_{2m}(a) + Y_{2n}(a) Y_{2m}^{'}(a). \tag{2.65}$$

Incorporating the boundary conditions (2.59) and (2.60), we obtain

$$(s_n^2 - s_m^2) \int_a^b Y_{2n}(y) Y_{2m}(y) dy = -\frac{\eta_1}{\eta_2} Y_{1n}^{'}(a) Y_{1m}(a) + \frac{\eta_1}{\eta_2} Y_{1n}(a) Y_{1m}^{'}(a). \tag{2.66}$$

Multiplying the equation (2.64) by $\dfrac{\eta_1}{\eta_2}$ and adding to (2.66), yields

$$(s_n^2 - s_m^2) \left(\frac{\eta_1}{\eta_2} \int_0^a Y_{1n}(y) Y_{1m}(y) dy + \int_a^b Y_{2n}(y) Y_{2m}(y) dy \right) = 0. \tag{2.67}$$

When $m \neq n$, the above equation results in

$$\eta_1 \int_0^a Y_{1n}(y) Y_{1m}(y) dy + \eta_2 \int_a^b Y_{2n}(y) Y_{2m}(y) dy = 0. \tag{2.68}$$

On the other hand $m = n$, leads to

$$E_n = \eta_1 \int_0^a Y_{1n}^2(y) dy + \eta_2 \int_a^b Y_{2n}^2(y) dy. \tag{2.69}$$

The equations (2.68) and (2.69) collectively form the orthogonality relation for the eigenfunctions $Y_n(y)$,

$$\eta_1 \int_0^a Y_{1n}(y) Y_{1m}(y) dy + \eta_2 \int_a^b Y_{2n}(y) Y_{2m}(y) dy = \delta_{mn} E_n. \tag{2.70}$$

2.4.6 EM Fields in Cylindrical Coordinate System

In case of cylindrical coordinates, let us consider waves propagating in the z-direction in a material medium with wavenumber $k = \omega\sqrt{\epsilon\mu_0}$. The field components of these guided waves are written as $E(r,\theta,z) = \tilde{E}(r,\theta)e^{ik_z z}$ and $B(r,\theta,z) = \tilde{B}(r,\theta)e^{ik_z z}$, where $e^{ik_z z}$ shows z-dependence. The longitudinal components are given as E_z and B_z and transverse components are mentioned as E_r, E_θ, B_r and B_θ. The components of electric and magnetic fields for various mediums are

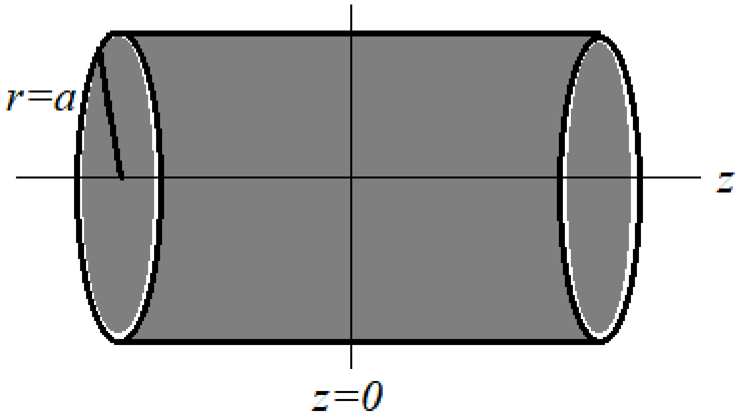

FIGURE 2.2: A cylindrical waveguide with duct radius a.

enumerated through six scalar counterparts of Maxwell's equations (2.5) and (2.6) in the following way:

$$\frac{1}{r}\frac{\partial E_z}{\partial \theta} - ik_z E_\theta = i\omega B_r, \tag{2.71}$$

$$-\frac{\partial E_z}{\partial r} + ik_z E_r = i\omega B_\theta, \tag{2.72}$$

$$\frac{\partial E_\theta}{\partial r} - \frac{1}{r}\frac{\partial E_r}{\partial \theta} = i\omega B_z, \tag{2.73}$$

$$\frac{1}{r}\frac{\partial B_z}{\partial \theta} - ik_z B_\theta = -i\omega\epsilon\mu_0 E_r, \tag{2.74}$$

$$-\frac{\partial B_z}{\partial r} + ik_z B_r = -i\omega\epsilon\mu_0 E_\theta, \tag{2.75}$$

$$\frac{\partial B_\theta}{\partial r} - \frac{1}{r}\frac{\partial B_r}{\partial \theta} = -i\omega\epsilon\mu_0 E_z. \tag{2.76}$$

The manipulation of equations (2.71)-(2.76) equips the transverse components in the form of longitudinal components as follows:

$$E_r = \frac{1}{k^2 - k_z^2}\left(ik_z\frac{\partial E_z}{\partial r} + i\omega\frac{1}{r}\frac{\partial B_z}{\partial \theta}\right), \quad E_\theta = \frac{1}{k^2 - k_z^2}\left(ik_z\frac{1}{r}\frac{\partial E_z}{\partial \theta} - i\omega\frac{\partial B_z}{\partial r}\right),$$

$$B_r = \frac{1}{k^2 - k_z^2}\left(-\frac{ik^2}{\omega}\frac{1}{r}\frac{\partial E_z}{\partial \theta} + ik_z\frac{\partial B_z}{\partial r}\right), \quad B_\theta = \frac{1}{k^2 - k_z^2}\left(\frac{ik^2}{\omega}\frac{\partial E_z}{\partial r} + ik_z\frac{1}{r}\frac{\partial B_z}{\partial \theta}\right).$$

The transverse components of fields for TE and TM cases are explained in the next subsections.

2.4.7 TE Wave

As the longitudinal component of electric field is zero, i. e., $E_z = 0$, in the case of TE wave, therefore the transverse components of fields can be stated as

$$E_r = \frac{i\omega}{k^2 - k_z^2}\frac{1}{r}\frac{\partial B_z}{\partial \theta}, \quad E_\theta = -\frac{i\omega}{k^2 - k_z^2}\frac{\partial B_z}{\partial r},$$

$$B_r = \frac{ik_z}{k^2 - k_z^2}\frac{\partial B_z}{\partial r}, \quad B_\theta = \frac{ik_z}{k^2 - k_z^2}\frac{1}{r}\frac{\partial B_z}{\partial \theta}.$$

2.4.8 TM Wave

For a TM wave, the components of magnetic field transverse to the direction of propagation survive, i. e., $B_z = 0$. The transverse components can be calculated through the longitudinal components as follows:

$$E_r = \frac{ik_z}{k^2 - k_z^2}\frac{\partial E_z}{\partial r}, \quad E_\theta = \frac{ik_z}{k^2 - k_z^2}\frac{1}{r}\frac{\partial E_z}{\partial \theta},$$

$$B_r = -\frac{ik^2}{\omega(k^2 - k_z^2)}\frac{1}{r}\frac{\partial E_z}{\partial \theta}, \quad B_\theta = \frac{ik^2}{\omega(k^2 - k_z^2)}\frac{\partial E_z}{\partial r}.$$

2.4.9 EM Fields in a Two Dimensional Cylindrical Waveguide

The Helmholtz equation for a plane wave propagating in a two dimensional waveguide ($\partial/\partial\theta = 0$) can be described as

$$\left(\frac{\partial^2}{\partial r^2} + \frac{1}{r}\frac{\partial}{\partial r} + \frac{\partial^2}{\partial z^2} + k^2\right)\begin{pmatrix} E_z \\ B_z \end{pmatrix} = \begin{pmatrix} 0 \\ 0 \end{pmatrix}. \tag{2.77}$$

The transverse field components can be described as

$$E_r = \frac{ik_z}{k^2 - k_z^2}\frac{\partial E_z}{\partial r}, \quad E_\theta = -\frac{i\omega}{k^2 - k_z^2}\frac{\partial B_z}{\partial r},$$

$$B_r = \frac{ik_z}{k^2 - k_z^2}\frac{\partial B_z}{\partial r}, \quad B_\theta = \frac{ik^2}{\omega(k^2 - k_z^2)}\frac{\partial E_z}{\partial r}.$$

The transverse components of fields in case of a TE wave are

$$E_r = 0, \quad E_\theta = -\frac{i\omega}{k^2 - k_z^2}\frac{\partial B_z}{\partial r},$$

$$B_r = \frac{ik_z}{k^2 - k_z^2}\frac{\partial B_z}{\partial r}, \quad B_\theta = 0,$$

while in the case of a TM wave, the transverse components are given as

$$E_r = \frac{ik_z}{k^2 - k_z^2}\frac{\partial E_z}{\partial r}, \quad E_\theta = 0,$$

$$B_r = 0, \quad B_\theta = \frac{ik^2}{\omega(k^2 - k_z^2)}\frac{\partial E_z}{\partial r}.$$

The Helmholtz equation for a uniform plane wave can be stated, in the form of field potential ϕ, as

$$\left(\frac{\partial^2}{\partial r^2} + \frac{1}{r}\frac{\partial}{\partial r} + \frac{\partial^2}{\partial z^2} + k^2\right)\phi = 0. \tag{2.78}$$

The traveling wave solution can be expressed as

$$\phi(r, z) = \sum_{n=0}^{\infty} \mathcal{B}_n R_n(r) e^{\pm i s_n z}, \tag{2.79}$$

where $R_n(r); n = 0, 1, 2, \ldots$ represent the eigenfunction expansions, with $\mathcal{B}_n$ and s_n representing the amplitudes and wavenumber of the nth mode.

The boundary condition for a PEC wall in a cylindrical structure is given as

$$\frac{\partial \phi}{\partial r} = 0. \tag{2.80}$$

2.4.10 Orthogonality Relation

Let us consider a duct $0 \leq y \leq b$, in which the boundary at $r = a$ separates two material mediums and a PEC wall is positioned at $r = b$. The eigenfunctions $R_n(r)$

for the two mediums can be expressed as

$$R_n(r) = \begin{cases} R_{1n}(r), & 0 \leq r \leq a, \\ R_{2n}(r), & a \leq r \leq b. \end{cases} \tag{2.81}$$

The eigen-sub-system can be formed as

$$R''_{1n}(r) + \frac{1}{r}R'_{1n}(r) - \tau_n^2 R_{1n}(r) = 0, \tag{2.82}$$

$$R''_{2n}(r) + \frac{1}{r}R'_{2n}(r) - \gamma_n^2 R_{2n}(r) = 0, \tag{2.83}$$

$$R'_{2n}(b) = 0, \tag{2.84}$$

$$R_{1n}(a) = R_{2n}(a), \tag{2.85}$$

$$\eta_1 R'_{1n}(a) = \eta_2 R'_{2n}(a), \tag{2.86}$$

where $\tau_n^2 = k_1^2 - s_n^2$ and $\gamma_n^2 = k_2^2 - s_n^2; n = 0, 1, 2, \ldots$ where k_1 and k_2 are the wavenumbers of the two mediums, with η_1 and η_2 representing the impedances in the respective two mediums.

Multiplying equation (2.82) by $R_{1m}(r)r$ and integrating from 0 to a,

$$\int_0^a (rR'_{1n}(r))' R_{1m}(r)dr = \tau_n^2 \int_0^a R_{1n}(r)R_{1m}(r)rdr. \tag{2.87}$$

Applying the integration by parts of the left hand side of (2.87), we obtain

$$\begin{aligned} \int_0^a (rR'_{1n}(r))' R_{1m}(r)dr &= \Big[rR'_{1n}(r)R_{1m}(r)\Big]_0^a - \Big[rR_{1n}(r)R'_{1m}(r)\Big]_0^a \\ &\quad + \int_0^a (rR'_{1m}(r))' R_{1n}(r)dr \\ &= aR'_{1n}(a)R_{1m}(a) - aR_{1n}(a)R'_{1m}(a) + \tau_m^2 \int_0^a R_{1n}(r)R_{1m}(r)rdr. \end{aligned} \tag{2.88}$$

Substituting (2.88) in (2.87) results in

$$(\tau_n^2 - \tau_m^2) \int_0^a R_{1n}(r)R_{1m}(r)rdr = aR'_{1n}(a)R_{1m}(a) - aR_{1n}(a)R'_{1m}(a). \tag{2.89}$$

The correlation between τ_n and s_n transforms the equation (2.89) as follows

$$(s_n^2 - s_m^2)\int_0^a R_{1n}(y)R_{1m}(r)rdr = aR_{1n}'(a)R_{1m}(a) - aR_{1n}(a)R_{1m}'(a). \tag{2.90}$$

Solving (2.83) likewise, the following equation is obtained

$$(s_n^2 - s_m^2)\int_a^b R_{2n}(r)R_{2m}(r)rdr = -aR_{2n}'(a)R_{2m}(a) + aR_{2n}(a)R_{2m}'(a). \tag{2.91}$$

Invoking the boundary conditions (2.84)-(2.86), yields

$$(s_n^2 - s_m^2)\int_a^b R_{2n}(r)R_{2m}(r)rdr = -\frac{\eta_1}{\eta_2}aR_{1n}'(a)R_{1m}(a) + \frac{\eta_1}{\eta_2}aR_{1n}(a)R_{1m}'(a). \tag{2.92}$$

Multiplying (2.90) by $\dfrac{\eta_1}{\eta_2}$ and adding to (2.92), yields

$$(s_n^2 - s_m^2)\left(\frac{\eta_1}{\eta_2}\int_0^a R_{1n}(r)R_{1m}(r)rdr + \int_a^b R_{2n}(r)R_{2m}(r)rdr\right) = 0. \tag{2.93}$$

When $m \neq n$, the equation (2.93) can be expressed as

$$\eta_1\int_0^a R_{1n}(r)R_{1m}(r)rdr + \eta_2\int_a^b R_{2n}(r)R_{2m}(r)rdr = 0. \tag{2.94}$$

However, when $m = n$, we can write

$$E_n = \eta_1\int_0^a R_{1n}^2(r)rdr + \eta_2\int_a^b R_{2n}^2(r)rdr. \tag{2.95}$$

The equations (2.94) and (2.95) collectively form the orthogonality relation for the eigenfunctions $R_n(y)$,

$$\eta_1\int_0^a R_{1n}(r)R_{1m}(r)rdr + \eta_2\int_a^b R_{2n}(r)R_{2m}(r)rdr = \delta_{mn}E_n. \tag{2.96}$$

2.5 MM Technique

The MM method is a useful approach to treat discontinuities in waveguides. This method is applicable if the structure is piece-wise uniform along one spatial direction.

It is mandatory that the waveguide at the discontinuous surface can be split into simpler separate regions each comprising of a different set of waveguide modes. Expanded theoretically as an infinite series of the waveguide modes, the EM field in each of these regions is actually a weighted superposition of these modes. The modes of any two separate regions can be matched at the interface using some conditions for the EM fields **E** and **H**. For computational reasons, these series are truncated according to the degree of accuracy required. The mode-coefficients of the two regions are connected through a scattering matrix. The steps involved in the application of MM method are as follows:

1. The Helmholtz equation is solved in the different regions of the waveguide by incorporating the variable separable technique and the imposed boundary conditions.
2. The EM fields in the regions are specified with suitable eigenfunctions according to the geometric configuration of the waveguide [119–121].
3. The related orthogonality relations in every region of the waveguide are determined.
4. The matching of the transverse field components between the regions at their interface is performed.
5. An infinite system of linear algebraic equations with unknown mode coefficients is obtained. These coefficients are determined after truncating the number of modes.

The MM technique provides an exact solution to the formulated scattering problems. The accuracy of the solution can be confirmed easily by reconstruction of matching conditions and energy conservation.

2.6 Energy Flux

Named after the English physicist John Henry Poynting, the Poynting vector expressed as $\mathbf{S} = \mathbf{E} \times \mathbf{H}^*$ denotes the energy flux per unit area. A real form of the fields **E** and **H** is utilized to compute the time average Poynting vector $\frac{1}{2}\mathrm{Re}(\mathbf{E} \times \mathbf{H}^*)$ [122]. In case of a two dimensional rectangular waveguide, the energy flux in form of scalar field potential ϕ is stated as

$$Power = \frac{1}{2} Re \left(\int_R \phi \left(\frac{\partial \phi}{\partial x} \right)^* dy \right), \tag{2.97}$$

where (*) represents complex conjugate.

For a two dimensional cylindrical waveguide, the power flux can be revealed as [123]

$$Power = \int_R \pi r Re \left\{ \phi \left(\frac{\partial \phi}{\partial z} \right)^* \right\} dr. \tag{2.98}$$

After calculating the powers in all regions of the waveguide the existence of the law of conservation of energy is confirmed. This law, which mathematically states that the transmitted power is equal to the sum of incident and reflected powers, establishes the accuracy of MM solution of the wave scattering problem.

Chapter 3

The EM Wave Propagation in Discontinuous Waveguide containing Plasma

3.1 Introduction

A cold plasma rectangular waveguide is a type of waveguide that uses a rectangular cross-section to guide EM waves through a cold plasma medium. In this chapter, the electromagnetic wave scattering from the cold plasma rectangular waveguide having semi-infinite and finite length is discussed. The presence of the cold plasma allows for the manipulation and control of EM waves within the waveguide, making it a versatile tool in various applications such as particle acceleration, and microwave transmission.

This chapter contains two problems. In the first problem, a semi-infinite cold plasma strip enclosed by metallic walls is placed in an infinite waveguide, and the scattering behavior of EM waves in the waveguide is discussed. The plasma layer is positioned between the dielectric layers, with metallic conducting plates separating them. The waveguide's enclosing boundaries are also made of metallic conducting material. However, in the second problem the EM scattering in a two-dimensional parallel plate rectangular waveguide, featuring a finite slab of cold plasma sandwiched between metallic strips is discussed. The plasma is positioned in a groove situated in the central finite region. The central region is enclosed, with and without metallic strips, by dielectric medium. Both of these problems are solved by using the MM technique. The eigenfunctions and related features in the segments of the waveguide with identical physical properties remain same for both of these problems. However, the eigenfunction expansions, scattering coefficients and interface conditions are different. In both problems, the solution is projected on the orthogonal basis while the matching conditions help to convert the differential system into linear algebraic systems that are truncated and solved numerically.

This chapter is arranged in ten sections. Sections 3.1-3.5 comprise the discussion on the scattering of EM waves in a parallel plate waveguide with a rectangular region containing cold plasma. The problem formulation is described in Section 3.2. The MM solution has been discussed in Section 3.3. The section 3.4 provides the validation of law of conservation of energy. Numerical results and discussion on findings are outlined in Section 3.5.

Sections 3.6-3.10 explore electromagnetic wave scattering from a finite plasma slab enclosed by metal strips as well as embedded within a dielectric environment. Section 3.7 discusses the physical aspects of the problem and provides a concise overview of the subject. Section 3.8 presents the solution of the boundary value problem using Helmholtz equation and boundary conditions, yielding the eigenfunctions, which are then used to numerically compute transmission and reflection coefficients. The energy identity is established in Section 3.9. In 3.10, simulations are conducted for both the frequency ranges, namely the transparency region (where the EM wave frequency exceeds the plasma frequency) and the non-transparency region (where the EM wave frequency is lower than the plasma frequency). Power analysis is conducted for different heights in both the frequency regimes. The reflection and transmission coefficients are also determined with reference to the normalized wave frequency for both transparency and non-transparency regions.

Conceptually, the problem discussed in Sections 3.6-3.10 represents a finite counterpart to the semi-infinite plasma slab problem addressed in Sections 3.1-3.5.

3.2 Problem Statement

The scattering of EM waves in a parallel plate waveguide with a rectangular region containing cold plasma is investigated.

The waveguide, extending along the x-axis, features an abrupt change in height at $x = 0$, effectively splitting it into two distinct regions $x < 0$ and $x > 0$. Figure 3.1 illustrates the structure under discussion.

The interior of the regions $x < 0, |y| < h$ and $x > 0, |y| > a$ is assumed dielectric having permittivity and permeability ϵ_0 and μ_0, respectively and indicates the speed of light $c = \sqrt{1/\epsilon_0 \mu_0}$.

On the other hand, the region defined as, $x > 0, |y| < a$, comprises cold plasma characterized by the permeability μ_0 and permittivity tensor $\overline{\epsilon}$.

A harmonic time dependence $e^{-i\omega t}$ is assumed, with ω being the angular frequency, and is omitted from subsequent expressions for simplicity [114].

Incorporate a direct magnetic field $\mathbf{B}_0$ into cold plasma in the longitudinal direction and containing induced current $\mathbf{J} = \overline{\sigma}\mathbf{E}$, where $\mathbf{E}$ represents electric field and $\overline{\sigma}$ is conductivity tensor defined as

$$\overline{\sigma} = \frac{n_p e^2}{m} \begin{bmatrix} -\dfrac{i\omega}{\omega_c^2 - \omega^2} & \dfrac{\omega_c}{\omega_c^2 - \omega^2} & 0 \\ -\dfrac{\omega_c}{\omega_c^2 - \omega^2} & -\dfrac{i\omega}{\omega_c^2 - \omega^2} & 0 \\ 0 & 0 & \dfrac{i}{\omega} \end{bmatrix}.$$

The electric charge, plasma density, electron mass, cyclotron frequency, and plasma frequency are denoted by e, n_p, m, ω_c, and ω_p, respectively [116]. The conductivity tensor's relationship with the permittivity tensor $\overline{\epsilon}$ can now be represented as

$$\overline{\epsilon} = \overline{1} - \frac{\overline{\sigma}}{i\omega\epsilon_0},$$

where $\overline{1}$ is unit tensor.

The displacement vector $\mathbf{D}$ is now described as $\mathbf{D} = \bar{\epsilon}\mathbf{E}$, where $\bar{\epsilon}$ is the permittivity tensor for plasma medium and can be expressed as [115]

$$\bar{\epsilon} = \begin{bmatrix} \epsilon_1 & -i\epsilon_2 & 0 \\ i\epsilon_2 & \epsilon_1 & 0 \\ 0 & 0 & \epsilon_3 \end{bmatrix}.$$

The tensor components ϵ_1, ϵ_2 and ϵ_3 are found through the properties of EM fields in an anisotropic medium, that are

$$\epsilon_1 = 1 - \frac{\omega_p^2}{\omega^2 - \omega_c^2}, \quad \epsilon_2 = \frac{\omega_c \omega_p^2}{\omega\left(\omega^2 - \omega_c^2\right)}, \quad \epsilon_3 = 1 - \frac{\omega_p^2}{\omega^2},$$

where

$$\omega_p^2 = \frac{n_p e^2}{m\epsilon_0}, \qquad \omega_c = \frac{|e|\mu_0 B_0}{m}.$$

It is important to note that the quantity B_0 represents the magnitude of the direct magnetic field. The metallic conducting walls, running along $y = \pm a$ and $y = \pm b$, horizontally bound the regions and vertically along $-b < y < -a$ and $a < y < b$, where $a < b$.

The propagation of EM waves in a waveguide is determined by Maxwell's equations, which are responsible for governing this phenomenon and are listed below:

- In dielectric,

$$\begin{aligned} \nabla \times \mathbf{E} &= i\omega\mathbf{B}, \\ \nabla \times \mathbf{B} &= -i\frac{\omega}{c^2}\mathbf{E}. \end{aligned} \tag{3.1}$$

- In plasma,

$$\begin{aligned} \nabla \times \mathbf{E} &= i\omega\mathbf{B}, \\ \nabla \times \mathbf{B} &= -\frac{i}{\omega}\bar{\kappa}.\mathbf{E}. \end{aligned} \tag{3.2}$$

The tensor $\overline{\kappa}$ is defined as

$$\overline{\kappa} = \begin{bmatrix} \kappa_1 & \kappa_2 & 0 \\ -\kappa_2 & \kappa_1 & 0 \\ 0 & 0 & \kappa_3 \end{bmatrix}, \tag{3.3}$$

where $\kappa_1 = k_0^2\epsilon_1$, $\kappa_2 = -k_0^2 i\epsilon_2$, and $\kappa_3 = k_0^2\epsilon_3$, in which $k_0 = \omega/c$. For a two dimensional waveguide $(\partial/\partial z = 0)$, the EM fields can be decomposed into longitudinal components E_z and B_z and transverse components E_x, E_y, B_x and B_y.

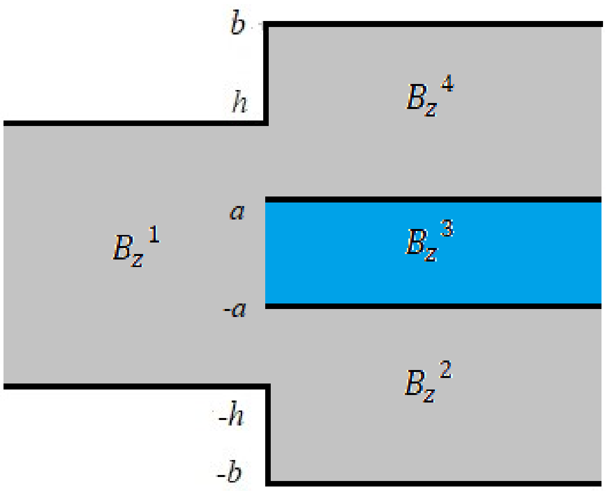

FIGURE 3.1: Geometry of the problem.

For a dielectric material, the longitudinal components obey the Helmholtz equation stated as

$$\left(\frac{\partial^2}{\partial x^2} + \frac{\partial^2}{\partial y^2} + k_0^2\right)\begin{pmatrix} E_z \\ B_z \end{pmatrix} = \begin{pmatrix} 0 \\ 0 \end{pmatrix}. \tag{3.4}$$

The transverse components are given as

$$E_x = -\frac{c^2}{i\omega}\frac{\partial B_z}{\partial y}, \quad E_y = \frac{c^2}{i\omega}\frac{\partial B_z}{\partial x},$$

$$B_x = \frac{1}{i\omega}\frac{\partial E_z}{\partial y}, \quad B_y = -\frac{1}{i\omega}\frac{\partial E_z}{\partial x}.$$

In case of cold unmagnetized plasma, the cyclotron frequency, $\omega_c = 0$, then $\kappa_2 = 0$ and $\kappa_1 = \kappa_3$. The Helmholtz equation is expressed as [117]

$$\left(\frac{\partial^2}{\partial x^2} + \frac{\partial^2}{\partial y^2} + \kappa_3\right)\begin{pmatrix} E_z \\ B_z \end{pmatrix} = \begin{pmatrix} 0 \\ 0 \end{pmatrix}. \tag{3.5}$$

The transverse components can be given as

$$E_x = \frac{i\omega}{\kappa_3}\frac{\partial B_z}{\partial y}, \quad E_y = -\frac{i\omega}{\kappa_3}\frac{\partial B_z}{\partial x},$$

$$B_x = \frac{1}{i\omega}\frac{\partial E_z}{\partial y}, \quad B_y = -\frac{1}{i\omega}\frac{\partial E_z}{\partial x}.$$

3.3 Formulation and Solution of the Governing Boundary Value Problem using MM Method

Let us formulate the boundary value problem by considering a TE mode incident from the left and propagating in the positive x direction. The magnetic field potential $B_z(x, y)$ in harmonic time-independent form, can be expressed by

$$B_z(x,y) = \begin{cases} B_z^1(x,y), & x < 0, \quad -h < y < h, \\ B_z^2(x,y), & x > 0, \quad -b < y < -a, \\ B_z^3(x,y), & x > 0, \quad -a < y < a, \\ B_z^4(x,y), & x > 0, \quad a < y < b. \end{cases} \tag{3.6}$$

The field potentials B_z^1, B_z^2 and B_z^4 satisfy the Helmholtz equation

$$\left(\nabla^2 + k_0^2\right) B_z^j = 0, \quad j = 1, 2, 4,$$

whereas, in cold plasma region, the field B_z^3 satisfies the equation

$$\left(\nabla^2 + \kappa_3\right) B_z^3 = 0,$$

The boundaries at $y = \pm h$ in region $-\infty < x < 0$ and at $y = \pm a,\ \pm b$ in region $0 < x < \infty$ are metallic conducting. Accordingly, the boundary conditions in these regions are given by

$$\frac{\partial B_z^1}{\partial y} = 0, \quad y = \pm h, \tag{3.7}$$

$$\frac{\partial B_z^2}{\partial y} = 0, \quad y = -b, -a, \tag{3.8}$$

$$\frac{\partial B_z^3}{\partial y} = 0, \quad y = \pm a, \tag{3.9}$$

$$\frac{\partial B_z^4}{\partial y} = 0, \quad y = a, b. \tag{3.10}$$

In order to address the boundary value problem using the MM method, the initial step involves determining the expansions of eigenfunctions and the corresponding orthogonality conditions within each region of the waveguide.

The Helmholtz equation along with boundary conditions in region $-\infty < x < 0$, renders the eigenexpansion form as follows

$$B_z^1 = e^{ik_0 x} + \sum_{n=0}^{\infty} A_n e^{-i\nu_n x}\phi_n(y), \quad -h < y < h, \tag{3.11}$$

where $\nu_n = \sqrt{k_0^2 - \left(\frac{n\pi}{2h}\right)^2}, n = 0, 1, 2, \ldots,$ is wavenumber of nth reflected mode, A_n is the amplitude and $\phi_n(y) = \cosh\left[\frac{n\pi}{2h}(y+h)\right], n = 0, 1, 2\ldots$ are the eigenfunctions corresponding to eigenvalues $n\pi/2h$. Accordingly, the eigenexpansion form in region $0 < x < \infty$ can be written as

$$B_z^2 = \sum_{n=0}^{\infty} B_n e^{i\tau_n x} Y_{1n}(y), \tag{3.12}$$

$$B_z^3 = \sum_{n=0}^{\infty} C_n e^{i\gamma_n x} Y_{2n}(y), \tag{3.13}$$

$$B_z^4 = \sum_{n=0}^{\infty} D_n e^{i\tau_n x} Y_{3n}(y). \tag{3.14}$$

Here $B_n, C_n, D_n, n = 0, 1, 2, \ldots$ represent the the amplitudes, the wavenumber of nth transmitted mode in each dielectric region is given by $\tau_n = \sqrt{k_0^2 - (\frac{n\pi}{b-a})^2}$, while $\gamma_n = \sqrt{\kappa_3 - (\frac{n\pi}{2a})^2}$, is the wavenumber in cold plasma. The eigenfunctions $Y_{1n}(y) = \cos\{\frac{n\pi}{(b-a)}(y+b)\}$, $Y_{2n}(y) = \cos\{\frac{n\pi}{(b-a)}(y+b)\}$ and $Y_{3n}(y) = \cos\{\frac{n\pi}{(b-a)}(y-b)\}$, satisfy the following orthogonality relations

$$\int_{-b}^{-a} Y_{1m}Y_{1n}dy = \delta_{mn}\left(\frac{b-a}{2}\right)\epsilon_m, \tag{3.15}$$

$$\int_{-a}^{a} Y_{2m}Y_{2n}dy = \delta_{mn}a\epsilon_m, \tag{3.16}$$

$$\int_{a}^{b} Y_{3m}Y_{3n}dy = \delta_{mn}\left(\frac{b-a}{2}\right)\epsilon_m, \tag{3.17}$$

where δ_{mn} is Kronecker delta and $\epsilon_m = 2$ for $m = 0$ and 1 otherwise. The continuity of EM fields at the interface provides the matching conditions as follows,

$$B_z^1(0,y) = \begin{cases} B_z^2(0,y), & -h < y < -a \\ B_z^3(0,y), & -a \le y \le a, \\ B_z^4(0,y), & a < y < h, \end{cases} \tag{3.18}$$

$$\frac{\partial B_z^2}{\partial x}(0,y) = \begin{cases} 0, & -b \le y \le -h, \\ \frac{\partial B_z^1}{\partial x}(0,y), & -h \le y \le -a, \end{cases} \tag{3.19}$$

$$\frac{\partial B_z^3}{\partial x}(0,y) = \left(\frac{\kappa_3}{k_0^2}\right)\frac{\partial B_z^1}{\partial x}(0,y), -a \le y \le a, \tag{3.20}$$

$$\frac{\partial B_z^4}{\partial x}(0,y) = \begin{cases} \frac{\partial B_z^1}{\partial x}(0,y), & a \le y \le h, \\ 0, & h \le y \le b. \end{cases} \tag{3.21}$$

Employing (3.11)-(3.14), the matching condition (3.18) readily implies

$$1 + \sum_{n=0}^{\infty} A_n\phi_n(y) = \begin{cases} \sum_{n=0}^{\infty} B_nY_{1n}(y), & -h < y < -a, \\ \sum_{n=0}^{\infty} C_nY_{2n}(y), & -a < y < a, \\ \sum_{n=0}^{\infty} D_nY_{3n}(y), & a < y < h. \end{cases} \tag{3.22}$$

To normalize (3.22) with respect to $\phi_m(y)$, we multiply both sides of it by $\phi_m(y)$

and integrate from $-h$ to h to get

$$A_m = -\delta_{m0} + \frac{1}{\epsilon_m h}\left\{\sum_{n=0}^{\infty} B_n P_{mn} + \sum_{n=0}^{\infty} C_n Q_{mn} + \sum_{n=0}^{\infty} D_n R_{mn}\right\}, \tag{3.23}$$

where

$$P_{mn} = \int_{-h}^{-a} \phi_m(y) Y_{1n}(y) dy,$$

$$Q_{mn} = \int_{-a}^{a} \phi_m(y) Y_{2n}(y) dy,$$

$$R_{mn} = \int_{a}^{h} \phi_m(y) Y_{3n}(y) dy.$$

Accordingly, on using (3.11)-(3.14) into the matching conditions (3.19)-(3.21) reveals

$$\sum_{n=0}^{\infty} B_n \tau_n Y_{1n}(y) = \begin{cases} 0, & -b \le y \le -h \\ k_0 - \sum_{n=0}^{\infty} A_n \nu_n \phi_n(y), & -h \le y \le -a, \end{cases} \tag{3.24}$$

$$\sum_{n=0}^{\infty} C_n \gamma_n Y_{2n}(y) = \frac{\kappa_3}{k_0^2}\left(k_0 - \sum_{n=0}^{\infty} A_n \nu_n \phi_n(y)\right), -a \le y \le a, \tag{3.25}$$

$$\sum_{n=0}^{\infty} D_n \tau_n Y_{3n}(y) = \begin{cases} k_0 - \sum_{n=0}^{\infty} A_n \nu_n \phi_n(y), & a \le y \le h, \\ 0, & h \le y \le b. \end{cases} \tag{3.26}$$

After performing mathematical rearrangements, normalizing (3.24)-(3.26) with respect to the associated $Y_{jn}, j = 1, 2, 3$ results in

$$B_m = \frac{2}{(b-a)\tau_m \epsilon_m}\left(k_0 P_{0m} - \sum_{n=0}^{\infty} A_n \nu_n P_{nm}\right), \tag{3.27}$$

$$C_m = \frac{\kappa_3}{a k_0^2 \gamma_m \epsilon_m}\left(k_0 Q_{0m} - \sum_{n=0}^{\infty} A_n \nu_n Q_{nm}\right), \tag{3.28}$$

$$D_m = \frac{2}{(b-a)\tau_m \epsilon_m}\left(k_0 R_{0m} - \sum_{n=0}^{\infty} A_n \nu_n R_{nm}\right). \tag{3.29}$$

The equation (3.23) in conjunction with equations (3.27)-(3.29) expose a series of infinite equations with unknowns $\{A_n, B_n, C_n, D_n\}$. The numerical solution of the truncated system will be elaborated on in the numerical results section.

3.4 Energy Identity

The energy identity is satisfied by the system mentioned above. By rewriting (3.23), we can derive the identity as follows:

$$\epsilon_m h A_m^* = -2h\delta_{m0} + \sum_{n=0}^{\infty} \left\{ B_n^* P_{mn}^* + C_n^* Q_{mn}^* + D_n^* R_{mn}^* \right\}, \tag{3.30}$$

where (*) denotes the complex conjugate. On multiplying (3.30) by $\sum\limits_{m=0}^{\infty} A_m \nu_m$, we find

$$\begin{aligned} h\sum_{m=0}^{\infty} |A_m|^2 \nu_m \epsilon_m &= -2hA_0 k_0 \\ &+ \sum_{m=0}^{\infty} A_m\nu_m \sum_{n=0}^{\infty} B_n^* P_{mn}^* + \sum_{m=0}^{\infty} A_m\nu_m \sum_{n=0}^{\infty} C_n^* Q_{mn}^* + \sum_{m=0}^{\infty} A_m\nu_m \sum_{n=0}^{\infty} D_n^* R_{mn}^*. \end{aligned} \tag{3.31}$$

Similarly, rearranging (3.27)-(3.29) and multiplying (3.27) by $\sum\limits_{m=0}^{\infty} B_m^*$, (3.28) by $\sum\limits_{m=0}^{\infty} C_m^*$ and (3.29) by $\sum\limits_{m=0}^{\infty} D_m^*$, yield

$$\left(\frac{b-a}{2}\right) \sum_{m=0}^{\infty} |B_m|^2 \tau_m \epsilon_m = k_0 \sum_{m=0}^{\infty} B_m^* P_{0m} - \sum_{n=0}^{\infty} A_n \nu_n \sum_{m=0}^{\infty} B_m^* P_{nm}, \tag{3.32}$$

$$\left(\frac{ak_0^2}{\kappa_3}\right) \sum_{m=0}^{\infty} |C_m|^2 \gamma_m \epsilon_m = k_0 \sum_{m=0}^{\infty} C_m^* Q_{0m} - \sum_{n=0}^{\infty} A_n \nu_n \sum_{m=0}^{\infty} C_m^* Q_{nm}, \tag{3.33}$$

$$\left(\frac{b-a}{2}\right) \sum_{m=0}^{\infty} |D_m|^2 \tau_m \epsilon_m = k_0 \sum_{m=0}^{\infty} D_m^* R_{0m} - \sum_{n=0}^{\infty} A_n \nu_n \sum_{m=0}^{\infty} D_m^* R_{nm}. \tag{3.34}$$

Adding (3.31)-(3.34) and simplifying, we conclude that

$$1 = \frac{1}{2k_0}Re\left(\sum_{n=0}^{\infty}|A_n|^2\nu_n\epsilon_n\right) + \frac{(b-a)}{4k_0h}Re\left(\sum_{n=0}^{\infty}|B_n|^2\tau_n\epsilon_n\right)$$
$$+\frac{ak_0}{2\kappa_3h}Re\left(\sum_{n=0}^{\infty}|C_n|^2\gamma_n\epsilon_n\right) + \frac{(b-a)}{4k_0h}Re\left(\sum_{n=0}^{\infty}|D_n|^2\tau_n\epsilon_n\right). \quad (3.35)$$

The energy identity in the duct regions can also be expressed as

$$P_i^1 + P_r^1 = P_t^2 + P_t^3 + P_t^4. \quad (3.36)$$

To provide a physical interpretation of the identity defined in equation (3.36), we delve into the calculation of EM power propagation in duct regions $R_j,\ j = 1, 2, 3, 4$ by using the Poynting vector given by

$$Power = \frac{1}{2}Re\left(\int_R E_y^* B_z dy\right). \quad (3.37)$$

The E_y component in the transverse direction has been previously discussed in relation to dielectric materials and cold plasma. The incident power P_i^1, in region R_1 is given by

$$P_i^1 = \frac{1}{2}Re\left(\int_{-h}^{h}\frac{c^2}{i\omega}\left(\frac{\partial B_z^i}{\partial x}\right)^* B_z^i dy\right).$$

Using the incident field $B_z^i = e^{ik_0x}$ in above equation gives

$$P_i^1 = \frac{1}{2}Re\left(\int_{-h}^{h}\frac{c^2}{i\omega}ik_0e^{-ik_0x}e^{ik_0x}dy\right),$$

or

$$P_i^1 = hc. \quad (3.38)$$

Therefore, an incident power $P_i^1 = hc$ is fed into the system. The reflected power P_r^1 in region R_1 can be found by using $B_z^1(x, y)$ in (3.37) as follows

$$P_r^1 = \frac{1}{2}Re\left(-\int_{-h}^{h}\frac{c^2}{i\omega}\sum_{n=0}^{\infty}\sum_{m=0}^{\infty}A_nA_m^*i\nu_m^*e^{i(\nu_n-\nu_m^*)x}\phi_n(y)\phi_m(y)dy\right).$$

The orthogonality of eigenfunctions $\phi_n(y)$ remolds the above equation as

$$P_r^1 = \frac{1}{2}Re\left(-\int_{-h}^{h}\frac{c^2}{\omega}\sum_{n=0}^{\infty}\sum_{m=0}^{\infty}A_nA_m^*\nu_m^*e^{i(\nu_n-\nu_m^*)x}\delta_{mn}h\epsilon_m\right).$$

On simplifying the above equation, we obtain

$$P_r^1 = -\frac{hc}{2k_0}Re\left(\sum_{n=0}^{\infty}|A_n|^2\nu_n^*\epsilon_n\right). \tag{3.39}$$

Similarly, using $B_z^2(x,y)$ in (3.37), the transmitted power P_t^2 in region R_2 can be calculated as

$$P_t^2 = \frac{1}{2}Re\left(\int_{-b}^{-a}\frac{c^2}{i\omega}\sum_{n=0}^{\infty}\sum_{m=0}^{\infty}B_nB_m^*i\tau_m^*e^{i(\tau_n-\tau_m^*)x}Y_{1n}(y)Y_{1m}(y)dy\right).$$

Applying the orthogonality relation (3.15)

$$P_t^2 = \frac{1}{2}Re\left(\int_{-b}^{-a}\frac{c^2}{i\omega}\sum_{n=0}^{\infty}\sum_{m=0}^{\infty}B_nB_m^*i\tau_m^*e^{i(\tau_n-\tau_m^*)x}\delta_{mn}\left(\frac{b-a}{2}\right)\epsilon_m\right),$$

or

$$P_t^2 = \frac{(b-a)c}{4k_0}Re\left(\sum_{n=0}^{\infty}|B_n|^2\tau_n^*\epsilon_n\right). \tag{3.40}$$

On the same lines, the energy flux P_t^3 and P_t^4 in regions R_3 and R_4 can be obtained as

$$P_t^3 = \frac{a\omega}{2\kappa_3}Re\left(\sum_{n=0}^{\infty}|C_n|^2\gamma_n^*\epsilon_n\right), \tag{3.41}$$

$$P_t^4 = \frac{(b-a)c}{4k_0}Re\left(\sum_{n=0}^{\infty}|D_n|^2\tau_n^*\epsilon_n\right). \tag{3.42}$$

Since $Re(\nu_n^*) = Re(\nu_n)$, $Re(\tau_n^*) = Re(\tau_n)$ and $Re(\gamma_n^*) = Re(\gamma_n)$, therefore we may write (3.39)-(3.42) as,

$$P_r^1 = -\frac{hc}{2k_0}Re\left(\sum_{n=0}^{\infty}|A_n|^2\nu_n\epsilon_n\right), \tag{3.43}$$

$$P_t^2 = \frac{(b-a)c}{4k_0}Re\left(\sum_{n=0}^{\infty}|B_n|^2\tau_n\epsilon_n\right), \tag{3.44}$$

$$P_t^3 = \frac{a\omega}{2\kappa_3} Re\left(\sum_{n=0}^{\infty} |C_n|^2 \gamma_n \epsilon_n\right), \tag{3.45}$$

$$P_t^4 = \frac{(b-a)c}{4k_0} Re\left(\sum_{n=0}^{\infty} |D_n|^2 \tau_n \epsilon_n\right. \tag{3.46}$$

The law of conservation of power asserts that the energy flow in the left-hand

region equals the energy flow in the right-hand region, that gives

$$\begin{aligned} hc - \frac{hc}{2k_0} Re\left(\sum_{n=0}^{\infty} |A_n|^2 \nu_n \epsilon_n\right) &= \frac{(b-a)c}{4k_0} Re\left(\sum_{n=0}^{\infty} |B_n|^2 \tau_n \epsilon_n\right) \\ &+ \frac{a\omega}{2\kappa_3} Re\left(\sum_{n=0}^{\infty} |C_n|^2 \gamma_n \epsilon_n\right) + \frac{(b-a)c}{4k_0} Re\left(\sum_{n=0}^{\infty} |D_n|^2 \tau_n \epsilon_n\right). \end{aligned} \tag{3.47}$$

Solving equation (3.47), we get the form

$$1 = \mathcal{E}_1 + \mathcal{E}_2 + \mathcal{E}_3 + \mathcal{E}_4,$$

where

$$\mathcal{E}_1 = \frac{1}{2k_0} Re\left(\sum_{n=0}^{\infty} |A_n|^2 \nu_n \epsilon_n\right),$$

$$\mathcal{E}_2 = \frac{(b-a)}{4k_0 h} Re\left(\sum_{n=0}^{\infty} |B_n|^2 \tau_n \epsilon_n\right),$$

$$\mathcal{E}_3 = \frac{ak_0}{2\kappa_3 h} Re\left(\sum_{n=0}^{\infty} |C_n|^2 \gamma_n \epsilon_n\right),$$

$$\mathcal{E}_4 = \frac{(b-a)}{4k_0 h} Re\left(\sum_{n=0}^{\infty} |D_n|^2 \tau_n \epsilon_n\right).$$

The calculations presented above clearly demonstrate that the energy flux determined through mathematical methods aligns with the energy determined physically using the Poynting vector.

The next section is structured to validate the matching conditions and explore the role of plasma in the reflection and transmission coefficients across each incident, reflected, and transmitted mode.

3.5 Numerical Results and Discussion

The results presented in this study are derived through the truncation and numerical solution of infinite system of linear algebraic equations, as described in the Section 3.3. The truncation of system of equations up to 150 terms results in a system containing 151 equations. After solving these equations we get the unknown coefficients $\{A_n, B_n, C_n, D_n\}$; $n = 0, 1, 2, \ldots, 150$.

These scattered mode coefficients are utilized for analyzing the propagation of power in the sections of the duct. The magnetic field potentials B_z^1, B_z^2, B_z^3 and B_z^4 are denoted by $\phi_1(x,y), \phi_2(x,y), \phi_3(x,y)$ and $\phi_4(x,y)$, respectively. The respective electric field potentials are represented by $\phi_{1x}(x,y)$, $\phi_{2x}(x,y), \phi_{3x}(x,y)$ and $\phi_{4x}(x,y)$.

The physical parameter chosen is speed of light, $c = 3 \times 10^8$ m/s. The respective dimensional duct heights are given as $\overline{a} = 0.004$ cm, $\overline{b} = 1$ cm, $\overline{h} = 0.085$ cm. The plasma frequency is taken as $\omega_p = 10^9$ radian/second. All values, except $\overline{h}$, are consistent with Najari et al. [106]. The radii a, b and h, are the non-dimensional analogues of $\overline{a}, \overline{b}$ and $\overline{h}$. The accuracy of the matching conditions at the interfaces is confirmed by using truncated solutions to reconstruct the conditions, as demonstrated through figures showing the non-dimensional magnetic and electric field profiles.

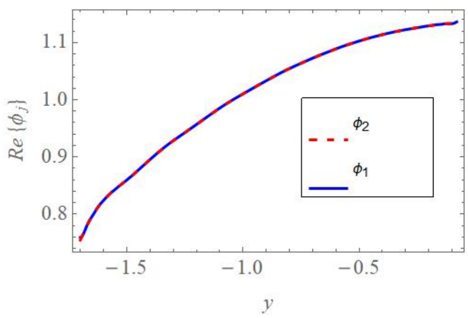

(a)

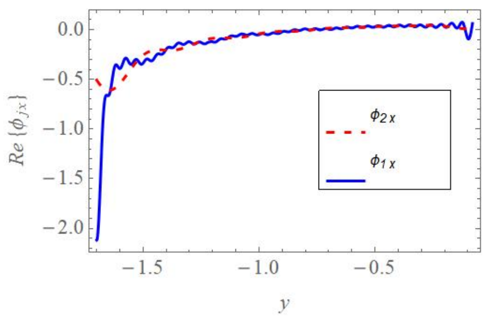

(b)

FIGURE 3.2: The real parts of (a) magnetic and (b) electric fields at $x = 0, -b < y < -a$.

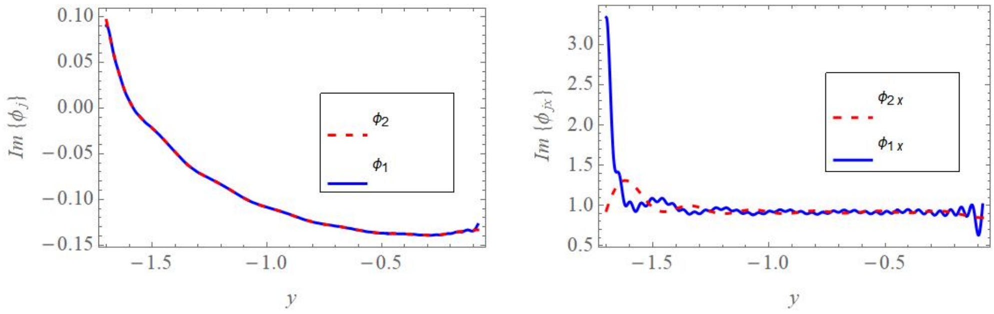

(a) (b)

FIGURE 3.3: The imaginary parts of (a) magnetic and (b) electric fields at $x = 0, -b < y < -a$.

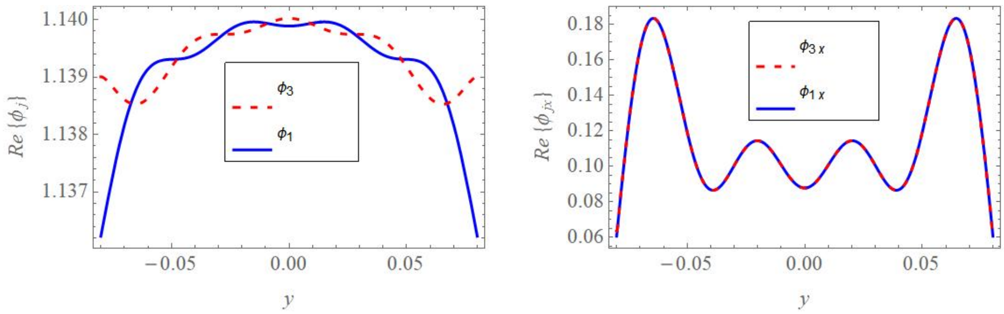

(a) (b)

FIGURE 3.4: The real parts of (a) magnetic and (b) electric fields at $x = 0, -a < y < a$.

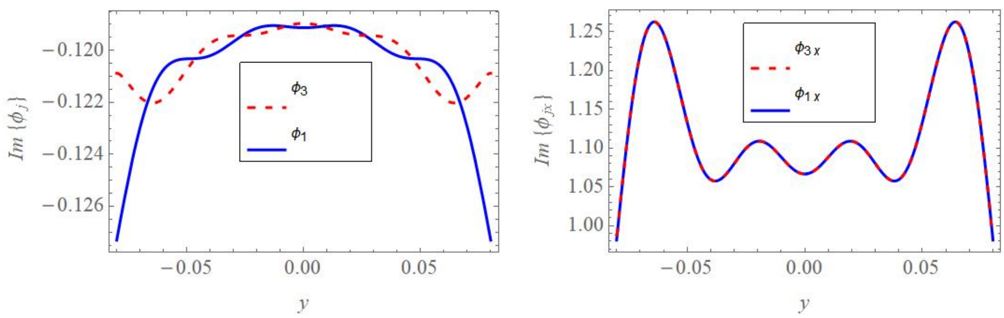

(a) (b)

FIGURE 3.5: The imaginary parts of (a) magnetic and (b) electric fields at $x = 0, -a < y < a$.

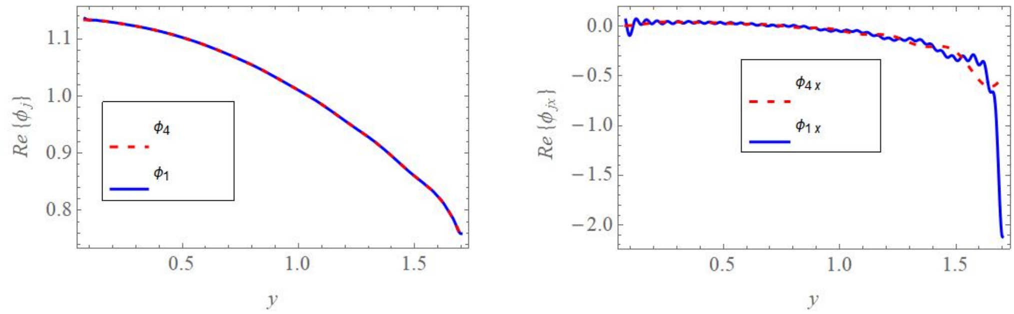

(a) (b)

FIGURE 3.6: The real parts of (a) magnetic and (b) electric fields at $x = 0, a < y < b$.

In case of dielectric regions $x < 0$ and $x > 0$, the graphs of fields are shown in figures 3.2-3.7. The magnetic and electric field curves completely coincide at the interface $x = 0$. Figures 3.4 and 3.5, show that the curves of magnetic and electric fields in cold plasma completely match at interface. The reflected and transmission coefficients $\{A_n, B_n, C_n, D_n\}$ with respect to the normalized wave frequency $b\omega/c$ are also determined and are plotted for $n = 0, 1, 2$. The normalized frequency is considered higher than 0.1 ($b\omega/c > 0.1$) in transparency region and lower than 0.1 ($0 < b\omega/c < 0.1$) in non-transparency region. In order to examine the reflected and transmitted coefficients, the incident mode numbers $n = 0, 1, 2$ are taken into account. The numerical computations have been done by Mathematica software of version 11. All the chosen parameters are same as were considered for verifying matching conditions, except ω. In all diagrams, the dimensionless normalized frequency $b\omega/c$ has been considered.

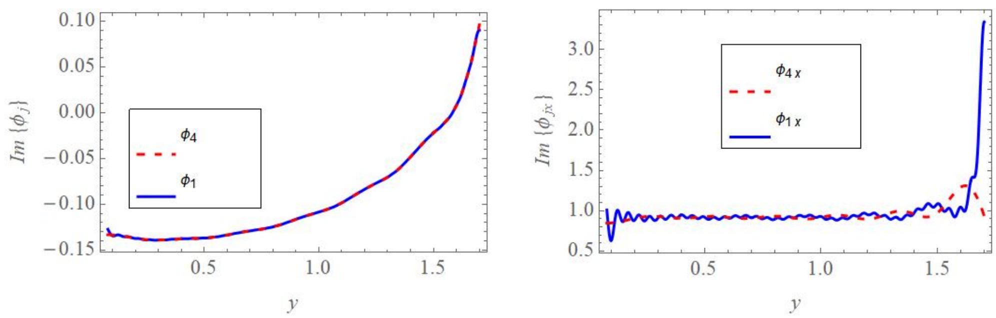

(a) (b)

FIGURE 3.7: The imaginary parts of (a) magnetic and (b) electric fields at $x = 0, a < y < b$.

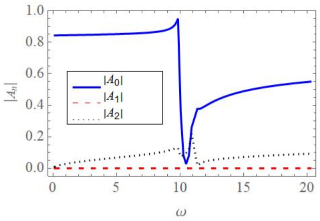

(a)

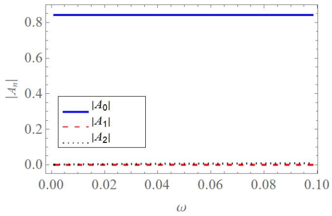

(b)

FIGURE 3.8: Reflected coefficients $|A_n|$ in (a) transparency and (b) non-transparency region.

Figure 3.8 shows the plot of reflection coefficients with respect to normalized frequency for the first three incident modes, including both transparency ($\omega > \omega_p$) and non-transparency ($\omega < \omega_p$) frequency domains. The first reflected mode stands out as the dominant mode in both the transparency and non-transparency regions, with a maximum magnitude in the transparency region. The transmission coefficients for the initial three incident modes are plotted against the normalized frequency $b\omega/c$ in Figure 3.9, encompassing both transparency and non-transparency frequency ranges. Upon examining the diagram, it is clear that in the transparency frequency regime, mode 2 is the dominant transmitted mode in the dielectric region $(-b < y < -a)$, whereas in the non-transparency case, mode 1 emerges as the dominant mode. Figure 3.10 illustrates the transmission coefficients for the first three incident modes in plasma, with mode 1 dominating in both transparency and non-transparency frequency regimes. The transmission coefficients in the dielectric region $(a < y < b)$ display the same pattern as in the region $(-b < y < -a)$, with mode 2 dominating in transparency and mode 1 in non-transparency, as shown in Figure 3.11.

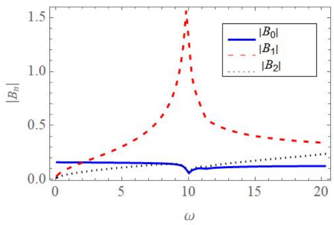

(a)

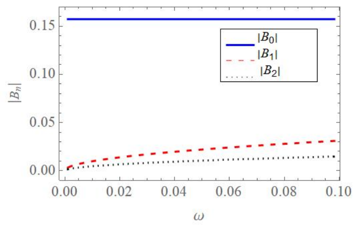

(b)

FIGURE 3.9: Transmitted coefficients in $|B_n|$ (a) transparency and (b) non-transparency region, $-b < y < -a$.

The transmission coefficient graphs exhibit a distinct peak at frequency 11.111 in the dielectric regions of the right duct and cold plasma, signifying resonance in both cases.

The power distribution graphs for different non-dimensional heights a, b, and h demonstrate power balance in both transparency and non-transparency regions, with the exception of the cold plasma region in non-transparency cases, where energy transmission is zero. The reflected power in left duct $(x < 0)$ is represented by $\mathcal{E}_1$. The quantities $\mathcal{E}_2, \mathcal{E}_3$ and $\mathcal{E}_4$ are the transmitted powers in right duct $(x > 0)$ in regions $-b \leq y \leq -a, -a \leq y \leq a$ and $a \leq y \leq b$, respectively. The sum of powers in all duct sections $\mathcal{E}_t$ is revealed as ,

$$\mathcal{E}_t = \mathcal{E}_1 + \mathcal{E}_2 + \mathcal{E}_3 + \mathcal{E}_4.$$

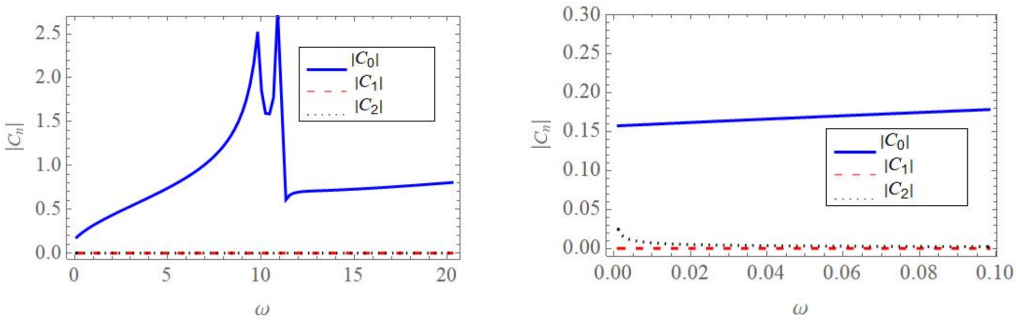

(a) (b)

FIGURE 3.10: Transmitted coefficients $|C_n|$ in (a) transparency and (b) non-transparency region, $-a < y < a$.

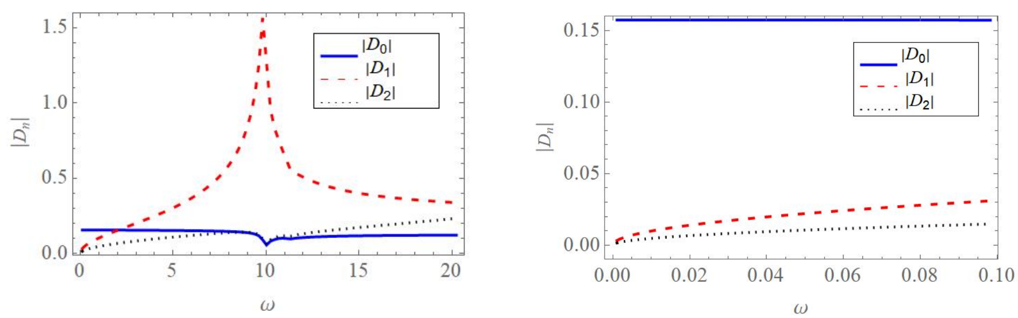

(a) (b)

FIGURE 3.11: Transmitted coefficients $|D_n|$ in (a) transparency and (b) non-transparency region, $a < y < b$.

TABLE 3.1: Cut-on modes versus angular frequency ω.

Frequency ($b\omega/c$)	Region 1	Region 2	Region 3	Region 4
0.111	1	1	0	1
10.028	1	2	0	2
11.334	1	2	1	2

TABLE 3.2: Cut-on modes versus height a.

Height (a)	Region 1	Region 2	Region 3	Region 4
0.02	2	5	1	5
1.6	2	5	2	5

For the graphs plotted against non-dimensional height a, the values of $\overline{a}$ are considered as 0.001 cm $< \overline{a} <$ 0.084 cm. Figure 3.12(a) illustrates that the transmission in cold plasma is enhanced as the plasma waveguide height a increases in the transparency region, whereas the reflection is amplified with the increment in a for the non-transparency region, see Figure 3.12(b).

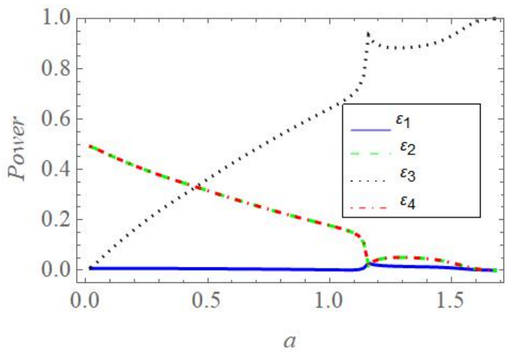

(a)

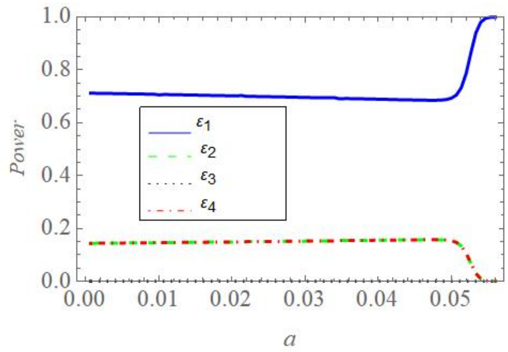

(b)

FIGURE 3.12: Power flux plotted against a in (a) transparency and (b) non-transparency region.

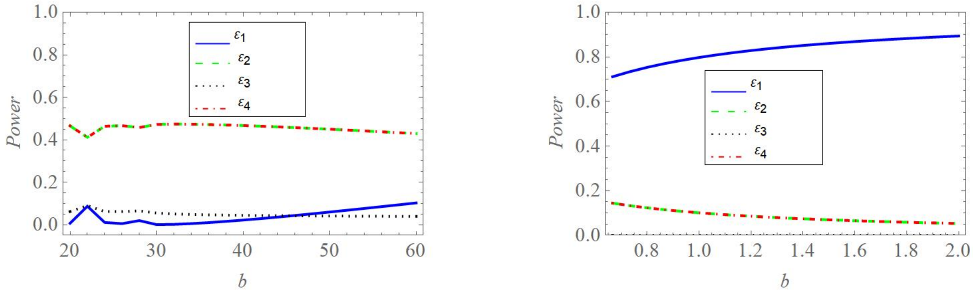

(a) (b)

FIGURE 3.13: Power flux plotted against b in (a) transparency and (b) non-transparency region.

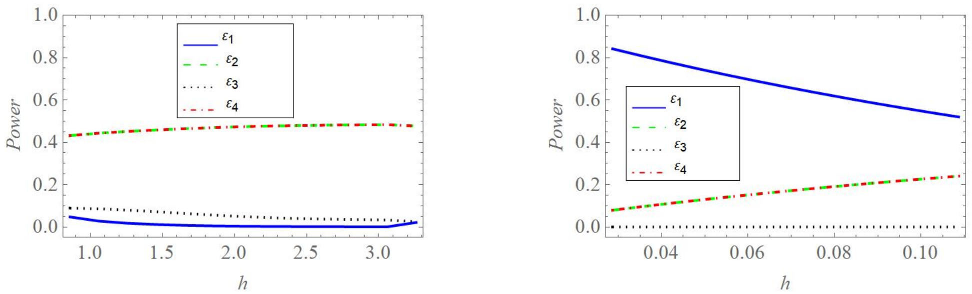

(a) (b)

FIGURE 3.14: Power flux plotted against h in (a) transparency and (b) non-transparency region.

TABLE 3.3: Cut-on modes versus height b.

Height (b)	Region 1	Region 2	Region 3	Region 4
20	2	7	1	7
24	2	8	1	8

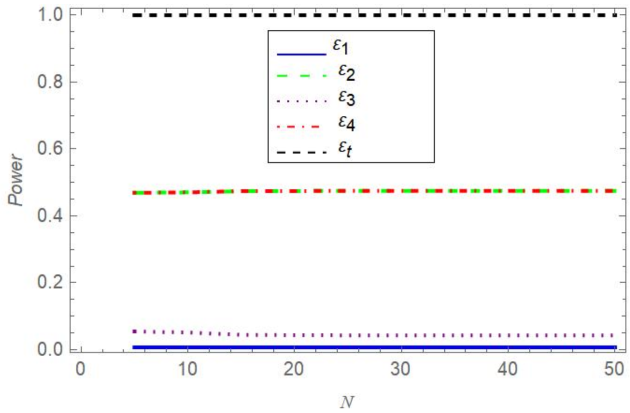

FIGURE 3.15: Power flux plotted against number of terms N.

When examining the relationship between power and height b, with a specified range 1 cm $< \bar{b} <$ 3 cm, a notable trend emerges. As evident from Figure 3.13(a), the rise in b implicates a gradual decrease in transmission in dielectric regions in transparency regime, However, in the non-transparency region, increase in reflection is apparent with increase in b, as revealed in Figure 3.13(b).

TABLE 3.4: Cut-on modes versus height h.

Height (h)	Region 1	Region 2	Region 3	Region 4
0.86	1	4	2	4
1.66	2	4	2	4
3.26	3	4	2	4

TABLE 3.5: Power conservation versus number of terms N.

Terms (N)	$\mathcal{E}_1$	$\mathcal{E}_2$	$\mathcal{E}_3$	$\mathcal{E}_4$	$\mathcal{E}_t$
5	0.007210	0.469161	0.054467	0.469161	1
10	0.007204	0.470669	0.051457	0.47669	1
15	0.007249	0.474104	0.044543	0.474104	1
20	0.007250	0.474622	0.043505	0.474622	1
25	0.007246	0.474896	0.042961	0.474896	1
30	0.007246	0.475005	0.042744	0.475005	1
35	0.007246	0.475081	0.042591	0.475081	1
40	0.007246	0.475086	0.042582	0.475086	1
45	0.007245	0.475087	0.042581	0.475087	1
50	0.007245	0.475092	0.042571	0.475092	1

Finally, the power graphs are plotted against the non-dimensional height h, with a range of 0.043 cm $< \bar{h} <$ 0.165 cm. The transmission has a dominant behavior in dielectric regions for transparency regime, while it is insignificant in cold plasma as apparent from Figure 3.14(a), as h grows. However, for non-transparency frequency range, the rise in the height h of the waveguide implies a decrease in the reflection and increase in transmission in dielectric regions, see Figure 3.14(b).

The number of cut-on modes versus angular frequency ω and duct heights a, b and h, in all regions of waveguide for transparency regime with respect to normalized frequency, are presented in tables 3.1-3.4. In these tables, Region 1 represents the left duct region $x < 0, -h \leq y \leq h$. The regions $-b \leq y \leq -a, -a \leq y \leq a$ and

$a \leq y \leq b$ in right duct $(x > 0)$ are represented by Region 2, Region 3 and Region 4, respectively.

Conservation of power implies that the truncated solution is convergent. The accuracy is verified up to six decimal places. It is noted that the impact of truncation diminishes to infinitesimal levels when $N \geq 25$. This fact is evident from Figure 3.15 as well as Table 3.5. Thus,the given system of infinite equations can be regarded as finite.

3.6 Cold Plasma-induced Effects on EM Scattering in Waveguides: An MM Analysis

This study deals with the complexities of EM scattering in a two-dimensional parallel plate rectangular waveguide, featuring a slab of cold plasma sandwiched between metallic strips. The plasma is positioned in a groove situated in the central region. The central region is enclosed, with and without metallic strips, by dielectric medium.

The core of the MM technique lies in the projection of the EM field solution onto basis functions. By representing the field using these basis functions, the problem is transformed into a set of linear algebraic equations that can be efficiently solved. One of the key insights gained from this study is the profound impact that geometric and material variations have on reflection and transmission phenomena within the waveguide.

The validation through numerical assessments further enhances confidence in the method's accuracy and reliability, highlighting its potential for advancing research in electromagnetics. The solution to this problem has far-reaching implications, as waveguides play a crucial role in the functioning of resonators and plasma propulsion engines, which are critical components in various technological applications.

The formulation of the related boundary problem is furnished in next section.

3.7 Formulation of Propagating Waves within a Plasma Slab

The discussion in this section focuses on the examination of how EM waves scatter when interacting with a plasma slab. This slab can either be situated between PEC plates or be positioned within a dielectric medium. The depicted physical arrangement in Figure 3.16 illustrates the central region layout of the metallic waveguide where the analysis of scattering is carried out. An **H**-polarized incident wave, making a zero angle with x axis, is contemplated to be traveling in the positive x direction within this scenario. The incident wave referred to in this context is presumed to represent the fundamental duct mode, characterized by a unit magnitude, traveling from the left inlet towards the interfaces on the right. Figure 3.16(a) shows the plasma slab enclosed by PEC walls, while Figure 3.16(b) depicts the plasma slab surrounded by a dielectric medium. The plasma slab's dimensions are constrained by $|y| < a$ and $|x| < L$, with PEC walls placed at $y = \pm a$ and $y = \pm b$ in Figure 3.16(a), and at $y = \pm b$ in Figure 3.16(b). The region between $|y| > a$ and $|y| < b$ is considered to be a dielectric medium with permittivity ϵ_0 and permeability μ_0. This configuration corresponds to a wavenumber k_0, which is defined as $k_0 = \omega\sqrt{\mu_0\epsilon_0}$, where ω represents the angular frequency and c denotes the speed of light. The speed of light, connected to the permittivity and permeability of free space as $c = \sqrt{1/\epsilon_0\mu_0}$, suggests the formation of k_0 as $k_0 = \omega/c$. However, for the case of a cold plasma, the permeability remains μ_0, and the permittivity tensor $\bar{\epsilon}$, as specified in references [115] and [116], is

$$\bar{\epsilon} = \begin{bmatrix} \epsilon_1 & -i\epsilon_2 & 0 \\ i\epsilon_2 & \epsilon_1 & 0 \\ 0 & 0 & \epsilon_3 \end{bmatrix},$$

where $\epsilon_1 = 1 - \dfrac{\omega_p^2}{\omega^2 - \omega_c^2}$, $\epsilon_2 = \dfrac{\omega_c\omega_p^2}{\omega\left(\omega^2 - \omega_c^2\right)}$ and $\epsilon_3 = 1 - \dfrac{\omega_p^2}{\omega^2}$. Here the quantities ω_p and ω_c stand for the frequencies associated with plasma and cyclotron effects, respectively. The exponential time-varying function $e^{-i\omega t}$ is considered and consistently excluded. [114].

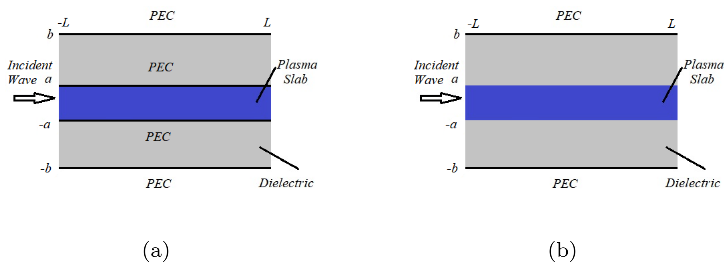

FIGURE 3.16: Cold plasma slab configuration: (a) enclosed by metal strips, and (b) embedded within a dielectric environment.

Maxwell's equations govern the transmission of EM waves within a waveguide. Faraday's law, as shown below, holds true for both dielectric and cold plasma mediums.

$$\nabla \times \mathbf{E} = i\omega \mathbf{B}. \tag{3.48}$$

In the context of dielectrics, Ampere's law can be expressed as follows:

$$\nabla \times \mathbf{B} = -i\frac{\omega}{c^2}\mathbf{E}, \tag{3.49}$$

while in the case of a cold plasma, this law is formulated as:

$$\nabla \times \mathbf{B} = -\frac{i}{\omega}k_0^2\bar{\epsilon}.\mathbf{E}. \tag{3.50}$$

In a two dimensional waveguide ($\partial/\partial z = 0$), the EM fields $\mathbf{E}$ and $\mathbf{B}$ consist of longitudinal components E_z and B_z as well as transverse components E_x, E_y, B_x and B_y. To depict EM wave propagation, the Helmholtz equation is solved along with boundary and interface conditions. In case of dielectric, the longitudinal components satisfy the Helmholtz equation

$$\left(\frac{\partial^2}{\partial x^2} + \frac{\partial^2}{\partial y^2} + k_0^2\right)\begin{pmatrix} E_z \\ B_z \end{pmatrix} = \begin{pmatrix} 0 \\ 0 \end{pmatrix}, \tag{3.51}$$

whereas, the transverse components can be determined by utilizing the details provided in the longitudinal components as indicated below:

$$E_x = -\frac{c^2}{i\omega}\frac{\partial B_z}{\partial y}, \quad E_y = \frac{c^2}{i\omega}\frac{\partial B_z}{\partial x},$$

$$B_x = \frac{1}{i\omega}\frac{\partial E_z}{\partial y}, \quad B_y = -\frac{1}{i\omega}\frac{\partial E_z}{\partial x}.$$

For cold unmagnetized plasma, the Helmholtz equation is expressed, in longitudinal components of fields, as [117]

$$\left(\frac{\partial^2}{\partial x^2} + \frac{\partial^2}{\partial y^2} + k_1^2\right)\begin{pmatrix} E_z \\ B_z \end{pmatrix} = \begin{pmatrix} 0 \\ 0 \end{pmatrix}. \tag{3.52}$$

The transverse components can be given as

$$E_x = \frac{i\omega}{k_1^2}\frac{\partial B_z}{\partial y}, \quad E_y = -\frac{i\omega}{k_1^2}\frac{\partial B_z}{\partial x},$$

$$B_x = \frac{1}{i\omega}\frac{\partial E_z}{\partial y}, \quad B_y = -\frac{1}{i\omega}\frac{\partial E_z}{\partial x}.$$

The wavenumber of cold plasma medium is indicated as $k_1 = \frac{\omega}{c}\sqrt{1 - \frac{\omega_p^2}{\omega^2}}$, where ω_p is the plasma frequency. Under the influence of a magnetic field, like in the upper atmosphere, ω_c assumes a non-zero value.

In such scenario, the presence of all components in the permittivity tensor $\bar{\epsilon}$ significantly impacts both the Helmholtz equation and the transverse components of the electric field, leading to a transformation in the matching conditions.

Solving equations (3.51) and (3.52) with boundary and interface conditions facilitates in determining wave propagation in the regions presented in Figure 3.16. The next subsection explains the traveling wave formulation applicable to **H**-polarized scenarios.

3.7.1 Plasma Slab Enclosed by Metal Strips

The boundary conditions at the metallic walls $y = \pm a$ and $\pm b$ in plasma are expressed as

$$\frac{\partial B_z}{\partial y}(x, \pm a) = 0 = \frac{\partial B_z}{\partial y}(x, \pm b). \tag{3.53}$$

On solving (3.52) subject to (3.53) with the separation of variable technique, the eigenfunction expansion formation can be achieved as:

$$B_z(x,y) = \begin{cases} \displaystyle\sum_{n=0}^{\infty} \left(B_n^{(1)} e^{i\zeta_n x} + C_n^{(1)} e^{-i\zeta_n x}\right) Y_{1n}(y), \\ \displaystyle\sum_{n=0}^{\infty} \left(B_n^{(2)} e^{i\lambda_n x} + C_n^{(2)} e^{-i\lambda_n x}\right) Y_{2n}(y), \\ \displaystyle\sum_{n=0}^{\infty} \left(B_n^{(3)} e^{i\zeta_n x} + C_n^{(3)} e^{-i\zeta_n x}\right) Y_{3n}(y), \end{cases} \tag{3.54}$$

where the amplitudes in the respective regions $-b < y < -a$, $a < y < a$ and $a < y < b$ are displayed by $B_n^{(j)}$ and $C_n^{(j)}$, $j = 1, 2, 3$. The wavenumbers of nth modes in these regions are $\zeta_n = \sqrt{k_0^2 - \left(\frac{n\pi}{b-a}\right)^2}$ and $\lambda_n = \sqrt{k_1^2 - \left(\frac{n\pi}{2a}\right)^2}$, $n = 0, 1, 2, \ldots$ Here the eigenfunctions $Y_{1n}(y) = \cos\left\{\left(\frac{n\pi}{b-a}\right)(y+b)\right\}$, $Y_{2n}(y) = \cos\left\{\left(\frac{n\pi}{2a}\right)(y+a)\right\}$, and $Y_{3n}(y) = \cos\left\{\left(\frac{n\pi}{b-a}\right)(y-b)\right\}$ are orthogonal and satisfy the usual orthogonality relations,

$$\left.\begin{aligned} \int_{-b}^{-a} Y_{1m}Y_{1n}dy &= \delta_{mn}\left(\frac{b-a}{2}\right)\epsilon_m, \\ \int_{-a}^{a} Y_{2m}Y_{2n}dy &= \delta_{mn}a\epsilon_m, \\ \int_{a}^{b} Y_{3m}Y_{3n}dy &= \delta_{mn}\left(\frac{b-a}{2}\right)\epsilon_m, \end{aligned}\right\} \tag{3.55}$$

where δ_{mn} is Kronecker delta and $\epsilon_m = 2$ for $m = 0$ and 1 otherwise.

3.7.2 Plasma Slab Embedded within a Dielectric Environment

The boundary conditions in case of slab layered in a dielectric environment are as follows:

$$B_z(x, -a^-) = B_z(x, -a^+), \tag{3.56}$$

$$B_z(x, a^-) = B_z(x, a^+), \tag{3.57}$$

$$\eta_0 \frac{\partial B_z}{\partial y}(x, -a^-) = \eta_1 \frac{\partial B_z}{\partial y}(x, -a^+), \tag{3.58}$$

$$\eta_1 \frac{\partial B_z}{\partial y}(x, a^-) = \eta_0 \frac{\partial B_z}{\partial y}(x, a^+), \tag{3.59}$$

$$\frac{\partial B_z}{\partial y}(x, \pm b) = 0, \tag{3.60}$$

such that the wavenumbers of cold plasma and dielectric and the respective surface impedances, η_0 and η_1, are correlated as $\eta_0 = 1/k_0^2$ and $\eta_1 = 1/k_1^2$. Using separation of variables on (3.52) with conditions (3.56)-(3.60) yields the eigenfunction expansion

$$B_z(x, y) = \sum_{n=0}^{\infty} (B_n e^{is_n x} + C_n e^{-is_n x}) Y_n(y), \tag{3.61}$$

whereas the amplitudes B_n and C_n correspond to the nth mode and the associated eigenfunctions $Y_n(y)$; $n = 0, 1, 2, \ldots$ in this groove are expressible as,

$$Y_n(y) = \begin{cases} Y_{1n}(y), & -b < y < -a, \\ Y_{2n}(y), & -a < y < a, \\ Y_{3n}(y), & a < y < b, \end{cases} \tag{3.62}$$

where

$$Y_{1n}(y) = \cosh[\tau_n(y + b)], \tag{3.63}$$

$$Y_{2n}(y) = \frac{1}{\eta_1 \gamma_n} \{\eta_0 \tau_n \sinh[\tau_n(b - a)] \sinh[\gamma_n(y + a)]\} \\ + \cosh[\tau_n(b - a)] \cosh[\gamma_n(y + a)], \tag{3.64}$$

$$Y_{3n}(y) = \frac{\cosh[\tau_n(y - b)]}{\eta_1 \gamma_n \cosh[\tau_n(b - a)]} \{\eta_0 \tau_n \sinh[\tau_n(b - a)] \sinh(2\gamma_n a)\} \\ + \eta_1 \gamma_n \cosh[\tau_n(y - b)] \cosh(2\gamma_n a), \tag{3.65}$$

satisfy the orthogonality relation as given below

$$\eta_0 \int_{-b}^{-a} Y_{1m} Y_{1n} dy + \eta_1 \int_{-a}^{a} Y_{2m} Y_{2n} dy + \eta_0 \int_{a}^{b} Y_{3m} Y_{3n} dy = \delta_{mn} E_m, \tag{3.66}$$

such that

$$E_n = \eta_0 \int_{-b}^{-a} Y_{1n}^2 dy + \eta_1 \int_{-a}^{a} Y_{2n}^2 dy + \eta_0 \int_{a}^{b} Y_{3n}^2 dy. \tag{3.67}$$

The quantities τ_n and γ_n, expressed as $\tau_n = \sqrt{s_n^2 - k_0^2}$ and $\gamma_n = \sqrt{s_n^2 - k_1^2}$, are the roots corresponding to the characteristic equation,

$$\eta_0^2\tau_n^2 \sinh^2[\tau_n(b-a)] \sinh(2\gamma_n a) + \eta_1^2\gamma_n^2 \cosh^2[\tau_n(b-a)] \sinh(2\gamma_n a)$$
$$+\eta_0\eta_1\tau_n\gamma_n \sinh[2\tau_n(b-a)] \cosh(2\gamma_n a) = 0. \quad (3.68)$$

Here s_n indicates the wave number of nth mode inside the groove.

3.8 An MM Approach to Plasma Slab Scattering

Within the context of waveguide technology, plasma slabs are implemented in the central part ($|x| < L$) of the waveguide, which extends infinitely along the x-axis. Figure 3.17 illustrates the geometrical configuration of both cases. The research pertains to examining how EM waves scatter when they encounter a plasma slab, starting from the region $x < -L$ and observing their interaction with the plasma-contained region as they leave the domain at $x > L$.

We consider an **H**-polarized wave incident on the partially confined waveguide, traveling in the positive x direction. The complete magnetic field potential $B_z^{(T)}(x,y)$, is stated as follows:

$$B_z^{(T)}(x,y) = \begin{cases} B_z^{(1)}(x,y), & x < -L, \quad -h < y < h, \\ B_z^{(2)}(x,y), & |x| < L, \quad -b < y < b, \\ B_z^{(3)}(x,y), & x > L, \quad -h < y < h. \end{cases} \quad (3.69)$$

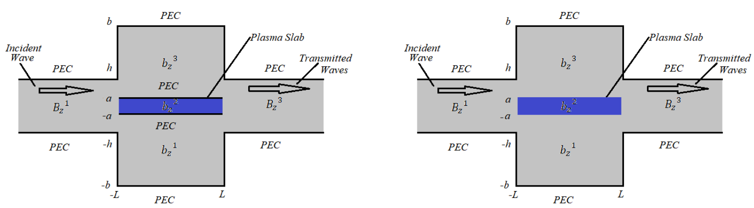

(a) (b)

FIGURE 3.17: Waveguide configuration: (a) enclosed by metal strips, and (b) embedded within a dielectric environment.

The eigenfunction expansions and corresponding orthogonality criteria are established by implementing the MM technique within each particular region of the waveguide.

Incorporating the method of separation of variables, the scattered fields within these regions $x < -L$ and $x > L$ can be illustrated as follows:

$$B_z^{(1)}(x,y) = e^{ik_0(x+L)} + \sum_{n=0}^{\infty} A_n e^{-i\nu_n(x+L)}\phi_n(y), \quad -h < y < h, \tag{3.70}$$

$$B_z^{(3)}(x,y) = \sum_{n=0}^{\infty} D_n e^{i\nu_n(x-L)}\phi_n(y), \quad -h < y < h. \tag{3.71}$$

In the regions $x < -L$ and $x > L$, the wavenumber of the nth mode ν_n, takes values of $n = 0, 1, 2$, and so on. The amplitudes A_n and D_n determine the intensity of these modes, while the eigenfunctions $\phi_n(y)$ can be expressed as,

$$\phi_n(y) = \cosh\left[\frac{n\pi}{2h}(y+h)\right].$$

Helmholtz equation and perfectly conducting boundary conditions are satisfied by the field potentials $B_z^{(1)}$ and $B_z^{(3)}$.

Two different plasma slab configurations - metallic strips and dielectric environments - have their eigenexpansions derivable from (3.54) and (3.61), respectively.

The eigenexpansions (3.54), (3.61), (3.70), and (3.71) contain unknown amplitudes that can be resolved by enforcing the matching conditions at the two interfaces.

3.8.1 Matching Conditions

Matching conditions arise from the continuity of fields at the interfaces $x = -L$ and $x = L$, namely

$$B_z^{(p)}(\pm L, y) = B_z^{(2)}(\pm L, y), \; -h \leq y \leq h, \tag{3.72}$$

$$\frac{\partial B_z^{(2)}}{\partial x}(\pm L, y) = \begin{cases} 0, & -b \leq y \leq -h, \\ \dfrac{\partial B_z^{(p)}}{\partial x}(\pm L, y), & -h \leq y \leq -a, \end{cases} \tag{3.73}$$

$$\frac{\partial B_z^{(2)}}{\partial x}(\pm L, y) = \frac{\eta_0}{\eta_1}\frac{\partial B_z^{(p)}}{\partial x}(\pm L, y), \ -a \leq y \leq a, \tag{3.74}$$

$$\frac{\partial B_z^{(2)}}{\partial x}(\pm L, y) = \begin{cases} \dfrac{\partial B_z^{(p)}}{\partial x}(\pm L, y), & a \leq y \leq h, \\ 0, & h \leq y \leq b, \end{cases} \tag{3.75}$$

where $p = 1$ for the field at interface $x = -L$ and $p = 3$ at interface $x = L$.

3.8.2 Plasma Slab Enclosed by Metal Strips

Application of the matching condition (3.72) along with some mathematical manipulations yields

$$\begin{aligned} A_m = -\delta_{m0} &+ \frac{1}{\epsilon_m h}\sum_{n=0}^{\infty}\left(B_n^{(1)}e^{-i\zeta_n L} + C_n^{(1)}e^{i\zeta_n L}\right)P_{mn} \\ &+ \frac{1}{\epsilon_m h}\sum_{n=0}^{\infty}\left(B_n^{(2)}e^{-i\lambda_n L} + C_n^{(2)}e^{i\lambda_n L}\right)Q_{mn} \\ &+ \frac{1}{\epsilon_m h}\sum_{n=0}^{\infty}\left(B_n^{(3)}e^{-i\zeta_n L} + C_n^{(3)}e^{i\zeta_n L}\right)R_{mn}, \end{aligned} \tag{3.76}$$

$$\begin{aligned} D_m = &\frac{1}{\epsilon_m h}\sum_{n=0}^{\infty}\left(B_n^{(1)}e^{i\zeta_n L} + C_n^{(1)}e^{-i\zeta_n L}\right)P_{mn} \\ &+ \frac{1}{\epsilon_m h}\sum_{n=0}^{\infty}\left(B_n^{(2)}e^{i\lambda_n L} + C_n^{(2)}e^{-}i\lambda_n L\right)Q_{mn} \\ &+ \frac{1}{\epsilon_m h}\sum_{n=0}^{\infty}\left(B_n^{(3)}e^{i\zeta_n L} + C_n^{(3)}e^{-i\zeta_n L}\right)R_{mn}, \end{aligned} \tag{3.77}$$

where

$$P_{mn} = \int_{-h}^{-a}\phi_m(y)Y_{1n}(y)dy, Q_{mn} = \int_{-a}^{a}\phi_m(y)Y_{2n}(y)dy, R_{mn} = \int_{a}^{h}\phi_m(y)Y_{3n}(y)dy.$$

Adding the equations (3.76) and (3.77), leads to

$$\Psi_m^+ = -\delta_{m0} + \frac{2}{h\epsilon_m}\left[\sum_{n=0}^{\infty} \Phi_{1n}^+ \cos(\zeta_n L) P_{mn} + \Phi_{2n}^+ \cos(\lambda_n L) Q_{mn} + \Phi_{3n}^+ \cos(\zeta_n L) R_{mn}\right], \tag{3.78}$$

while subtracting (3.77) from (3.76), submits

$$\Psi_m^- = -\delta_{m0} - \frac{2i}{h\epsilon_m}\left[\sum_{n=0}^{\infty} \Phi_{1n}^- \sin(\zeta_n L) P_{mn} + \Phi_{2n}^- \sin(\lambda_n L) Q_{mn} + \Phi_{3n}^- \sin(\zeta_n L) R_{mn}\right], \tag{3.79}$$

where $\Psi_m^\pm = A_m \pm D_m$ and $\Phi_{jm}^\pm = B_m^{(j)} \pm C_m^{(j)}, j = 1, 2, 3.$

The imposition of the conditions (3.73) to (3.75) at interface $x = -L$ leads to

$$\left(B_m^{(1)} e^{-i\zeta_m L} - C_m^{(1)} e^{i\zeta_m L}\right) = \frac{2}{\zeta_m \epsilon_m (b-a)}\left\{k_0 P_{0m} - \sum_{n=0}^{\infty} A_n \nu_n P_{nm}\right\}, \tag{3.80}$$

$$\left(B_m^{(2)} e^{-i\lambda_m L} - C_m^{(2)} e^{i\lambda_m L}\right) = \frac{\eta_0}{\eta_1 \lambda_m \epsilon_m a}\left\{k_0 Q_{0m} - \sum_{n=0}^{\infty} A_n \nu_n Q_{nm}\right\}, \tag{3.81}$$

$$\left(B_m^{(3)} e^{-i\zeta_m L} - C_m^{(3)} e^{i\zeta_m L}\right) = \frac{2}{\zeta_m \epsilon_m (b-a)}\left\{k_0 R_{0m} - \sum_{n=0}^{\infty} A_n \nu_n R_{nm}\right\}. \tag{3.82}$$

Invoking the matching conditions (3.73) to (3.75), in the same manner as before, at the interface $x = L$, displays

$$\left(B_m^{(1)} e^{i\zeta_m L} - C_m^{(1)} e^{-i\zeta_m L}\right) = \frac{2}{\zeta_m \epsilon_m (b-a)} \sum_{n=0}^{\infty} D_n \nu_n P_{nm}, \tag{3.83}$$

$$\left(B_m^{(2)} e^{i\lambda_m L} - C_m^{(2)} e^{-i\lambda_m L}\right) = \frac{\eta_0}{\eta_1 \lambda_m \epsilon_m a} \sum_{n=0}^{\infty} D_n \nu_n Q_{nm}, \tag{3.84}$$

$$\left(B_m^{(3)} e^{i\zeta_m L} - C_m^{(3)} e^{-i\zeta_m L}\right) = \frac{2}{\zeta_m \epsilon_m (b-a)} \sum_{n=0}^{\infty} D_n \nu_n R_{nm}. \tag{3.85}$$

Subtracting (3.80) from (3.83), (3.81) from (3.84) and (3.82) from (3.85) leads to the formation of the following equations

$$\Phi_{1m}^+ = \frac{i}{\zeta_m \epsilon_m \sin(\zeta_m L)(b-a)}\left(k_0 P_{0m} - \sum_{n=0}^{\infty} \Psi_n^+ \nu_n P_{nm}\right), \tag{3.86}$$

$$\Phi_{2m}^{+} = \frac{i\eta_0}{2\eta_1\lambda_m\epsilon_m a\sin(\lambda_m L)}\left(k_0 Q_{0m} - \sum_{n=0}^{\infty}\Psi_n^{+}\nu_n Q_{nm}\right), \tag{3.87}$$

$$\Phi_{3m}^{+} = \frac{i}{\zeta_m\epsilon_m \sin(\zeta_m L)(b-a)}\left(k_0 R_{0m} - \sum_{n=0}^{\infty}\Psi_n^{+}\nu_n R_{nm}\right). \tag{3.88}$$

Now, respective adding of (3.80) and (3.83), (3.81) and (3.84), (3.82) and (3.85) forms $\Phi_{1m}^{-}, \Phi_{2m}^{-}$ and Φ_{3m}^{-} in the following way

$$\Phi_{1m}^{-} = \frac{1}{\zeta_m\epsilon_m \cos(\zeta_m L)(b-a)}\left(k_0 P_{0m} - \sum_{n=0}^{\infty}\Psi_n^{-}\nu_n P_{nm}\right), \tag{3.89}$$

$$\Phi_{2m}^{-} = \frac{\eta_0}{2\eta_1\lambda_m\epsilon_m a\cos(\lambda_m L)}\left(k_0 Q_{0m} - \sum_{n=0}^{\infty}\Psi_n^{-}\nu_n Q_{nm}\right), \tag{3.90}$$

$$\Phi_{3m}^{-} = \frac{1}{\zeta_m\epsilon_m \cos(\zeta_m L)(b-a)}\left(k_0 R_{0m} - \sum_{n=0}^{\infty}\Psi_n^{-}\nu_n R_{nm}\right). \tag{3.91}$$

The equations (3.78), (3.79) and (3.86)-(3.91) disclose a system of infinite equations having the unknown coefficients $\left\{A_n, B_n^{(j)}, C_n^{(j)}, D_n\right\}$, $j = 1, 2, 3$. The numerical solution of this system, truncated to finite number of terms, is acquired and the results are presented and discussed in Section 3.10.

3.8.3 Plasma Slab Embedded within a Dielectric Environment

Imposing the matching condition (3.72) and normalizing result in

$$A_m = -\delta_{m0} + \frac{1}{\epsilon_m h}\left\{\sum_{n=0}^{\infty}\left(B_n e^{-is_nL} + C_n e^{is_nL}\right)\left(P_{mn} + Q_{mn} + R_{mn}\right)\right\}, \tag{3.92}$$

$$D_m = -\frac{1}{\epsilon_m h}\left\{\sum_{n=0}^{\infty}\left(B_n e^{is_nL} + C_n e^{-is_nL}\right)\left(P_{mn} + Q_{mn} + R_{mn}\right)\right\}. \tag{3.93}$$

Adding (3.92) and (3.93), produces

$$\Psi_m^+ = -\delta_{m0} + \frac{2}{h\epsilon_m}\sum_{n=0}^{\infty}\Phi_n^+\cos(s_nL)\left\{P_{mn}+Q_{mn}+R_{mn}\right\}, \tag{3.94}$$

and subtracting (3.93) from (3.92) results in

$$\Psi_m^- = -\delta_{m0} - \frac{2i}{h\epsilon_m}\sum_{n=0}^{\infty}\Phi_n^-\sin(s_nL)\left\{P_{mn}+Q_{mn}+R_{mn}\right\}. \tag{3.95}$$

where $\Psi_m^\pm = A_m \pm D_m$ and $\Phi_m^\pm = B_m \pm C_m$.

Applying matching conditions (3.73)-(3.75) at the interface $x=-L$ and solving, we get

$$\begin{aligned}\sum_{n=0}^{\infty}\left(B_ne^{-is_nL}-C_ne^{is_nL}\right)s_n\int_{-b}^{-a}Y_{1m}Y_{1n}dy\\ = k_0\int_{-b}^{-a}Y_{1m}dy-\sum_{n=0}^{\infty}A_n\nu_n\int_{-b}^{-a}Y_{1m}\phi_ndy,\end{aligned} \tag{3.96}$$

$$\begin{aligned}\frac{\eta_1}{\eta_0}\sum_{n=0}^{\infty}\left(B_ne^{-is_nL}-C_ne^{is_nL}\right)s_n\int_{-a}^{a}Y_{2m}Y_{2n}dy\\ = k_0\int_{-a}^{a}Y_{1m}dy-\sum_{n=0}^{\infty}A_n\nu_n\int_{-a}^{a}Y_{2m}\phi_ndy,\end{aligned} \tag{3.97}$$

$$\begin{aligned}\sum_{n=0}^{\infty}\left(B_ne^{-is_nL}-C_ne^{is_nL}\right)s_n\int_{a}^{b}Y_{3m}Y_{3n}dy\\ = k_0\int_{a}^{b}Y_{3m}dy-\sum_{n=0}^{\infty}A_n\nu_n\int_{a}^{b}Y_{3m}\phi_ndy.\end{aligned} \tag{3.98}$$

Adding the equations (3.96), (3.97) and (3.98) and employing the orthogonality relation (3.66), produces

$$\begin{aligned}B_me^{-is_mL}-C_me^{is_mL} = \frac{\eta_0k_0}{s_mE_m}\left(P_{0m}+Q_{0m}+R_{0m}\right)\\ -\frac{\eta_0}{s_mE_m}\sum_{n=0}^{\infty}A_n\nu_n\left(P_{nm}+Q_{nm}+R_{nm}\right).\end{aligned} \tag{3.99}$$

The same procedure is applied at the interface $x = L$ using conditions (3.73) to (3.75), leading to

$$B_m e^{is_m L} - C_m e^{-is_m L} = \frac{\eta_0}{s_m E_m} \sum_{n=0}^{\infty} D_n \nu_n \left(P_{nm} + Q_{nm} + R_{nm}\right). \tag{3.100}$$

Subtracting (3.99) from (3.100), brings out

$$\Phi_m^+ = \frac{ik_0\eta_0}{2s_m E_m \sin(s_m L)} \left(P_{0m} + Q_{0m} + R_{0m}\right)$$
$$-\frac{i\eta_0}{2s_m E_m \sin(s_m L)} \sum_{n=0}^{\infty} \Psi_n^+ \nu_n \left(P_{nm} + Q_{nm} + R_{nm}\right), \tag{3.101}$$

while adding (3.99) and (3.100) creates

$$\Phi_m^- = \frac{k_0\eta_0}{2s_m E_m \cos(s_m L)} \left(P_{0m} + Q_{0m} + R_{0m}\right)$$
$$-\frac{\eta_0}{2s_m E_m \cos(s_m L)} \sum_{n=0}^{\infty} \Psi_n^- \nu_n \left(P_{nm} + Q_{nm} + R_{nm}\right). \tag{3.102}$$

A system of infinite algebraic equations is divulged through equations (3.94), (3.95), (3.101) and (3.102), with unknowns $\{A_n, B_n, C_n, D_n\}$. Truncating this system produces a numerical solution, which is then analyzed and presented in the Numerical Results section.

3.9 Energy Flux

The energy flux serves as a vital indicator of the accuracy and convergence of approximate solutions. By utilizing the Poynting vector, we can effectively calculate the energy transmission in duct regions,

$$Power = \frac{1}{2} Re \left(\int_R E_y^* B_z dy \right), \tag{3.103}$$

where (*) represents complex conjugate.

The component E_y of electric field in a dielectric medium, is stated as

$$E_y = -\frac{1}{i\omega\epsilon_0} \frac{\partial B_z}{\partial x}, \tag{3.104}$$

while for the case of cold plasma

$$E_y = \frac{c^2\eta_1}{i\omega\eta_0}\frac{\partial B_z}{\partial x}. \tag{3.105}$$

The Poynting vector enables the calculation of the incident P_i, reflected P_r and transmitted P_t powers, which are listed as

$$P_i = -\frac{k_0 h}{\omega\epsilon_0}, \tag{3.106}$$

$$P_r = \frac{h}{2\omega\epsilon_0} Re\left(\sum_{n=0}^{\infty} |A_n|^2 \nu_n^* \epsilon_n\right), \tag{3.107}$$

$$P_t = -\frac{h}{2\omega\epsilon_0} Re\left(\sum_{n=0}^{\infty} |D_n|^2 \nu_n^* \epsilon_n\right). \tag{3.108}$$

Since $Re(\nu_n^*) = Re(\nu_n)$, therefore, (3.107) and (3.108) take the form,

$$P_r = \frac{h}{2\omega\epsilon_0} Re\left(\sum_{n=0}^{\infty} |A_n|^2 \nu_n \epsilon_n\right), \tag{3.109}$$

$$P_t = -\frac{h}{2\omega\epsilon_0} Re\left(\sum_{n=0}^{\infty} |D_n|^2 \nu_n \epsilon_n\right). \tag{3.110}$$

According to the law of conservation of power,

$$P_i + P_r = P_t.$$

This principle leads to

$$-\frac{k_0 h}{\omega\epsilon_0} + \frac{h}{2\omega\epsilon_0} Re\left(\sum_{n=0}^{\infty} |A_n|^2 \nu_n \epsilon_n\right) = -\frac{h}{2\omega\epsilon_0} Re\left(\sum_{n=0}^{\infty} |D_n|^2 \nu_n \epsilon_n\right). \tag{3.111}$$

Normalizing the incident power P_i to 1, equation (3.111) becomes

$$1 = \mathcal{E}_1 + \mathcal{E}_2, \tag{3.112}$$

where

$$\mathcal{E}_1 = \frac{1}{2k_0} Re\left(\sum_{n=0}^{\infty} |A_n|^2 \nu_n \epsilon_n\right),$$

$$\mathcal{E}_2 = \frac{1}{2k_0} Re \left(\sum_{n=0}^{\infty} |D_n|^2 \nu_n \epsilon_n \right).$$

3.10 Numerical Results and Discussion

Based on the preceding discussions, we now proceed to solve the physical problem numerically. We select the speed of light, $c = 3 \times 10^8$ m/s, as the key physical parameter for our numerical analysis. The magnetic field potential B_z is presented in figures as $\phi(x, y)$, stated as,

$$\phi(x,y) = \begin{cases} \phi_1(x,y), & x < -L, \quad -h < y < h, \\ \phi_2(x,y), & |x| < L, \quad -b < y < -a, \\ \phi_3(x,y), & |x| < L, \quad -a < y < a, \\ \phi_4(x,y), & |x| < L, \quad a < y < b, \\ \phi_5(x,y), & x > L, \quad -h < y < h. \end{cases}$$

The numerical calculations are carried out by using the software Mathematica (versions 11.0 & 12.1).

3.10.1 Case I

Upon truncating the system described by equations (3.78), (3.79), and (3.86)-(3.91) to 100 terms, the resulting solution is utilized to confirm the correctness of the algebraic manipulations and power distribution. The matching conditions at interfaces $x = -L$ and $x = L$ are subsequently re-established. The solution of these equations yields the unknown coefficients $\left\{A_n, B_n^{(j)}, C_n^{(j)}, D_n\right\}$, $j = 1, 2, 3,\ n = 0, 1, 2, \ldots, 99$.

The scattered coefficients and power distribution in the duct regions, corresponding to the incident duct modes $(n = 0, 1, 2)$ are plotted with reference to the normalized frequency $b\omega/c$.

Matching conditions at interfaces $x = -L$ and $x = L$ are used to validate the MM solution, with non-dimensional magnetic and electric fields shown in figures 3.18 and 3.19, respectively.

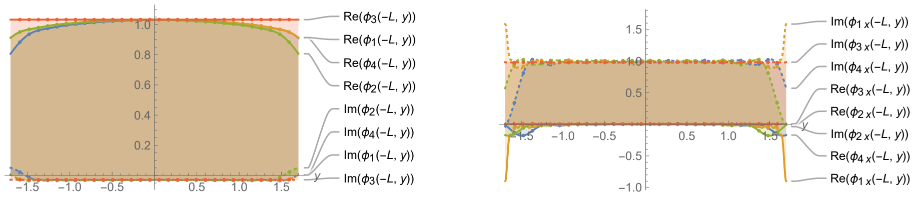

(a) (b)

FIGURE 3.18: The real and imaginary parts of (a) magnetic and (b) electric fields at $x = -L, -h < y < h$.

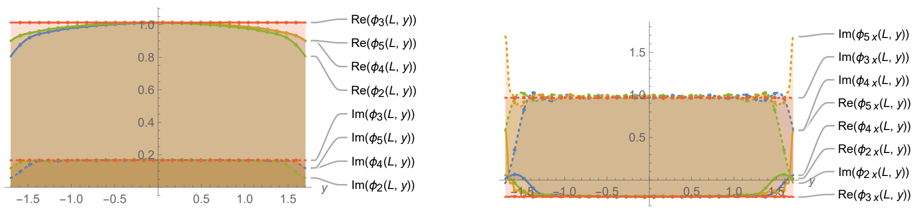

(a) (b)

FIGURE 3.19: The real and imaginary parts of (a) magnetic and (b) electric fields at $x = L, -h < y < h$.

Figures 3.20 and 3.21 show the reflection and transmission coefficients for the first three incident modes, plotted against normalized frequency $b\omega/c$. Notably, the frequency spectrum is divided into two distinct regions: a non-transparency region ($\omega < \omega_p$), where the angular frequency is lower than the plasma frequency, and a transparency region ($\omega > \omega_p$), where the angular frequency exceeds the plasma frequency.

The normalized frequency, $b\omega/c$, distinguishes between two regions: the transparency region, where $b\omega/c > 0.1$, and the non-transparency region, where $b\omega/c < 0.1$.

Figures 3.22-3.24 display the power distribution, with $\mathcal{E}_1$ and $\mathcal{E}_2$ representing the reflected and transmitted powers in the left duct ($x < -L$) and right duct ($x > L$), while $\mathcal{E}_t$ is the aggregate power across all regions of the ducts, such that

$$\mathcal{E}_t = \mathcal{E}_1 + \mathcal{E}_2.$$

Reflected and transmitted powers against the number of terms are plotted in Figure 3.25.

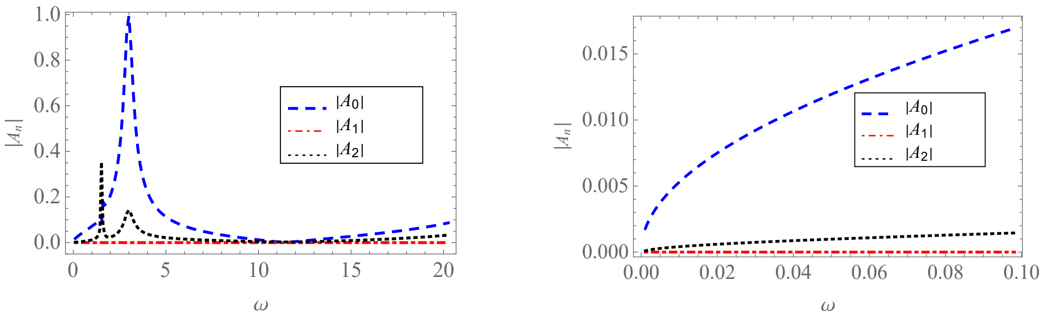

(a) (b)

FIGURE 3.20: Reflected coefficients $|A_n|$ in (a) transparency and (b) non-transparency region.

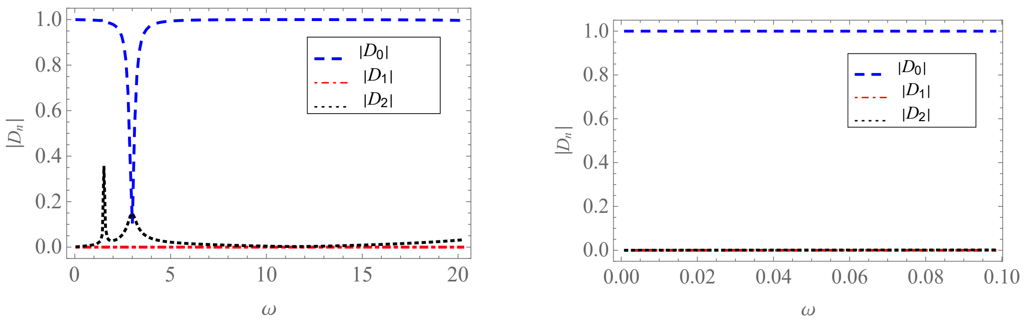

(a) (b)

FIGURE 3.21: Transmitted coefficients $|D_n|$ in (a) transparency and (b) non-transparency region.

The following parameters are set: duct heights $\overline{a} = 0.004$ cm, $\overline{b} = 1$ cm, and $\overline{h} = 0.085$ cm; groove length $\overline{L} = 2 \times 0.005$ cm; and plasma frequency $\omega_p = 10^9$ radian/second. These values are consistent with Najari et al. [106], ensuring a reliable basis for the calculations. Note that the non-dimensional quantities a, b, h, and L correspond to their dimensional counterparts $\overline{a}, \overline{b}, \overline{h}$, and $\overline{L}$, respectively. Additionally, unless otherwise specified, the angular frequency is set to $\omega = 6 \times 10^9$ radian/second for all plots, excluding the incident modes.

The reconstruction of matching conditions of magnetic field ϕ_i and the electric field $\phi_{ix} = \dfrac{\partial \phi_i}{\partial x}$, $i = 1, 2, 3, 4$ at interface $x = -L$ is shown in 3.18(a) and 3.18(b). The real and imaginary parts of these fields completely coincide at this interface. Figure 3.19(a) and 3.19(b) show excellent agreement between the real and imaginary parts of the magnetic ϕ_j, $j = 2, 3, 4, 5$ and the electric field potentials $\phi_{jx} = \dfrac{\partial \phi_j}{\partial x}$, demonstrating complete coincidence at the interface $x = L$. Figures 3.20(a) and 3.20(b) show that the first mode is dominant, while the second mode is negligible, in both transparency and non-transparency regimes, as seen in the reflection coefficient graphs versus normalized frequency for incident modes. However, in both transparency and non-transparency frequency regions, the transmitted mode 1 is dominant, while mode 2 is insignificant, as seen in the transmission coefficient plots for the first three consecutive modes, see 3.21.

TABLE 3.6: Cut-on modes versus height a.

Height (a)	Region 1	Region 2	Region 3	Region 4
0.02	2	5	1	2
1.6	2	5	2	2

TABLE 3.7: Cut-on modes versus height b.

Height (b)	Region 1	Region 2	Region 3	Region 4
20	2	7	1	2
24	2	8	1	2

Cut-on modes are calculated for the transparency regime in all regions of the waveguide, with respect to heights a, b, and h. The waveguide regions are defined as: Region 1: left duct $x < -L$, $|y| \leq h$; Region 2: $-b \leq y \leq -a$ or $a \leq y \leq b, |x| < L$; Region 3: cold plasma region $a \leq y \leq a, |x| < L$; and Region 4: right duct $x > L$, $|y| \leq h$.

The number of cut-on modes varies by region as height h increases: Regions 1 and 4 exhibit two modes, Region 2 (dielectric) has five, and Region 3 (cold plasma) has only one. The cut-on modes corresponding to heights a and b are listed in tables 3.6 and 3.7, respectively.

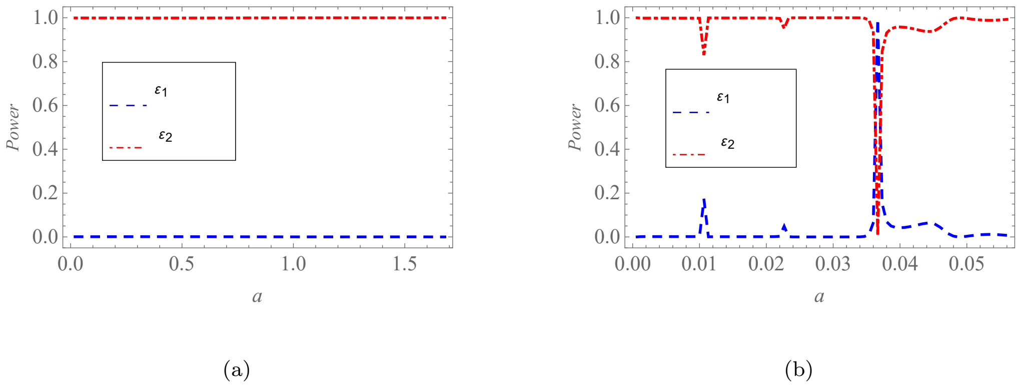

FIGURE 3.22: Power flux plotted against height a and in (a) transparency region and (b) non-transparency region.

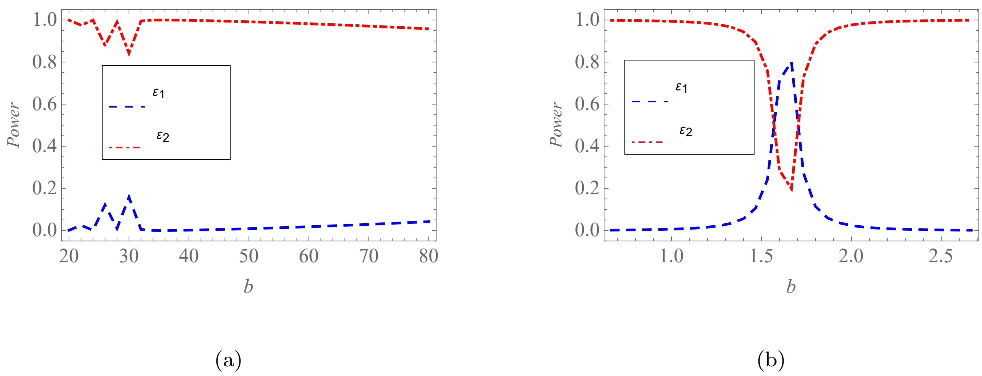

FIGURE 3.23: Power flux plotted against height b and in (a) transparency region and (b) non-transparency region.

The MM solution satisfies the power balance identity (3.112), stated in Section 3.9, for varying duct heights, as shown in figures 3.22-3.24. These figures display the energy flux behavior against duct heights a, b, and h in both transparency (a) and non-transparency (b) regimes, confirming the power balance identity.

Total transmission increases with height, with the exception of some fluctuations in the non-transparency regime for heights a and b. This observation is based on graphs plotted against heights, where the values of $\overline{a}, \overline{b}$ and $\overline{h}$ range from 0.001 cm-0.084 cm, 1 cm-4 cm, and 0.085 cm-0.12 cm, respectively.

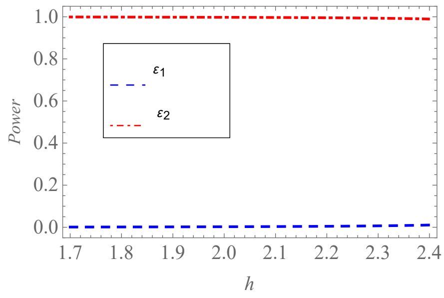

(a)

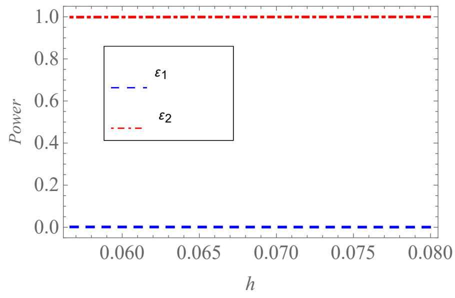

(b)

FIGURE 3.24: Power flux plotted against h in (a) transparency and (b) non-transparency region.

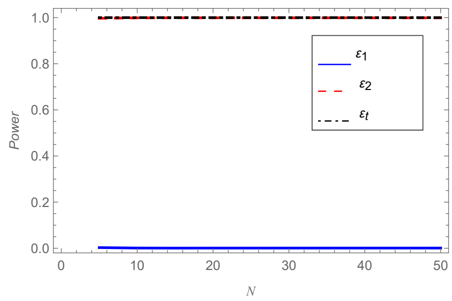

FIGURE 3.25: Power flux plotted against truncated terms N.

TABLE 3.8: Power conservation versus number of terms N.

Terms (N)	$\mathcal{E}_1$	$\mathcal{E}_2$	$\mathcal{E}_t$
5	0.002922	0.997078	1
10	0.000951	0.999049	1
15	0.000624	0.999376	1
20	0.000760	0.999240	1
25	0.000746	0.999254	1
30	0.000783	0.999217	1
35	0.000816	0.999184	1
40	0.000817	0.999183	1
45	0.000847	0.999153	1
50	0.000847	0.999153	1

The effect of truncation becomes negligible for $N \geq 45$, as shown in Figure 3.25 and Table 3.8, which display the variation of the modulus of powers with truncation number N. This allows the infinite system of algebraic equations to be effectively treated as finite.

3.10.2 Case II

The proposed solution is validated and physical insight is gained by truncating the system of equations (3.94), (3.95), (3.101) and (3.102) to 70 terms, with the following parameters: duct heights $\overline{a} = 0.4$ cm, $\overline{b} = 0.5$ cm, $\overline{h} = 0.45$ cm, groove length $2\overline{L} = 2 \times 0.42$ cm, and plasma frequency $\omega_p = 10^9$ radians/second.

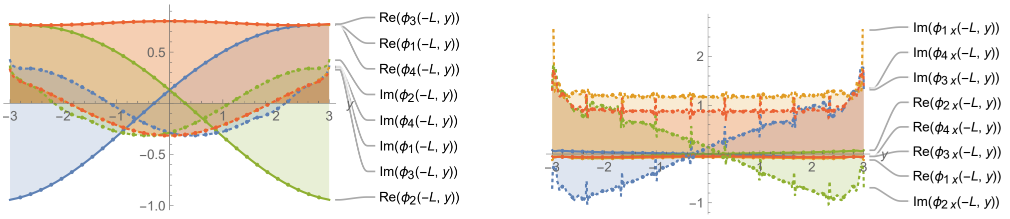

(a) (b)

FIGURE 3.26: The real and imaginary parts of (a) magnetic and (b) electric fields at $x = -L, -h < y < h$.

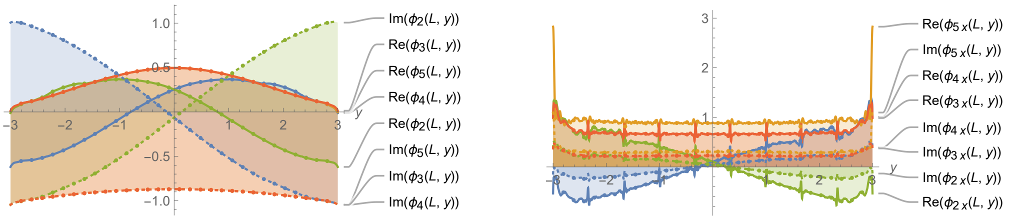

(a) (b)

FIGURE 3.27: The real and imaginary parts of (a) magnetic and (b) electric fields at $x = L, -h < y < h$.

The matching conditions of magnetic and electric fields are successfully reconstructed by the truncated solution, as demonstrated by the excellent agreement of the real and imaginary parts of the fields at the interfaces. Specifically, figures 3.26(a) and 3.26(b) show the agreement of ϕ_i and $\phi_{ix} = \dfrac{\partial \phi_i}{\partial x}$, $i = 1, 2, 3, 4$ at the interface $x = -L$, while figures 3.27(a) and 3.27(b) show the agreement of ϕ_j and $\phi_{jx} = \dfrac{\partial \phi_j}{\partial x}$, $j = 2, 3, 4, 5$ at the interface $x = L$.

Chapter 4

Exploring Scattering in a Cylindrical Duct with Plasma between Vacuum and Dielectric Layers

The scattering of EM waves in a cylindrical duct filled with plasma between vacuum and dielectric layers is a complex phenomenon that arises due to the interaction of the waves with the charged particles in the plasma. This chapter investigates the propagation of EM waves in a PEC cylindrical waveguide with a central chamber loaded with cold plasma. This plasma is embedded in vacuum which is covered by dielectric layer in the conducting cylinder. The ducts located on both the left and right sides of this bounded chamber contain vacuum. By solving the field equations rigorously, the dispersion relations are derived for all sections of this waveguide, providing a comprehensive and accurate understanding of the wave propagation characteristics. The mode coefficients in different duct regions are computed by employing MM method. In order to substantiate the accuracy of MM solution, the energy propagating along with these TM modes in all the regions of the waveguide is calculated.

The physical configuration of the waveguide having a central chamber filled with cold unmagnetized plasma in the middle and enveloped, respectively, in vacuum and dielectric is organized in Section 4.1. In Section 4.2, MM solution of this wave structure is acquired. Section 4.3 vindicates the cogency of the law of conservation of energy. Section 4.4 depicts the results obtained through numerical computations and their physical significance.

4.1 Problem Formulation

The scattering of the fundamental mode of a TM wave, of unit amplitude, in a waveguide comprising of cold unmagnetized plasma along with vacuum and dielectric medium is considered. The physical configuration of this setup is depicted in Figure 4.1. The cold plasma in the center, bounded by PEC walls, is wrapped around by vacuum. This vacuum is encompassed by a dielectric medium. The PEC walls enclose both the vacuum and the dielectric. The plasma medium is located between $|z| < L$. The PEC walls are positioned at radius $r = h_1, h_2$ and a in the region $|z| < L$.

The region $|z| > L$ is also considered to contain vacuum medium having PEC walls at radius $r = a$. The permittivity and permeability of vacuum are represented as ϵ_0 and μ_0, respectively. This configuration corresponds to a wave number k_0 in vacuum, which is defined as $k_0 = \omega\sqrt{\mu_0\epsilon_0}$, where ω represents the angular frequency and the speed of light c is stated as $c = \sqrt{1/\epsilon_0\mu_0}$.

This relation transforms the wavenumber k_0, as $k_0 = \omega/c$. The permittivity ϵ_d in dielectric medium is assumed to be $\epsilon_d = 2 \times \epsilon_0$, however, for the case of a cold plasma and dielectric, the permeability remains μ_0. In cold plasma, the permittivity $\bar{\epsilon}$ is in the form of tensor.

A cold, uniform, collisionless plasma of density n_p, passes through the center of the waveguide. Here, $\omega_p = (e^2 n_p/\epsilon_0 m)^{1/2}$ is the plasma frequency, and $\omega_c = eB_0/m$ denotes the electron cyclotron frequency. These frequencies involve e, m and B_0 which indicate the electric charge, electron mass and magnitude of direct magnetic

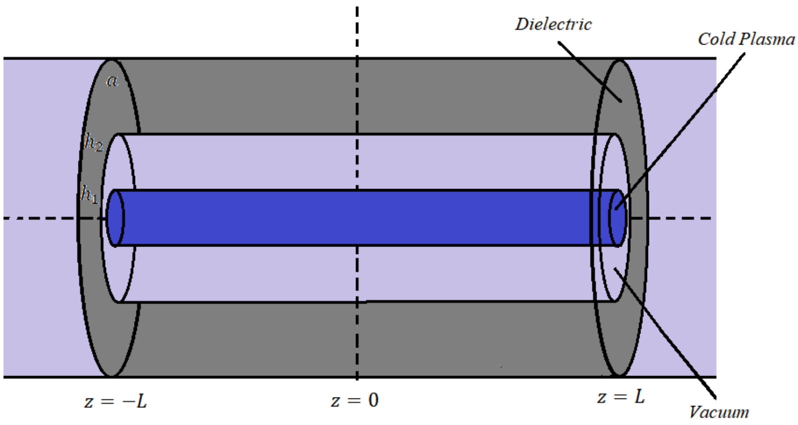

FIGURE 4.1: Cylindrical waveguide comprising of cold plasma, vacuum and dielectric mediums.

field, respectively. The permittivity tensor $\bar{\epsilon}$ [115]-[116], is

$$\bar{\epsilon} = \begin{bmatrix} \epsilon_1 & -i\epsilon_2 & 0 \\ i\epsilon_2 & \epsilon_1 & 0 \\ 0 & 0 & \epsilon_3 \end{bmatrix}, \tag{4.1}$$

where $\epsilon_1 = 1 - \dfrac{\omega_p^2}{\omega^2 - \omega_c^2}$, $\epsilon_2 = \dfrac{\omega_c \omega_p^2}{\omega\left(\omega^2 - \omega_c^2\right)}$ and $\epsilon_3 = 1 - \dfrac{\omega_p^2}{\omega^2}$. As we are considering unmagnetized plasma, therefore the effect of the magnetic field is zero in this medium. Hence $\epsilon_2 = 0$ and $\epsilon_1 = \epsilon_3$. A temporal variant $e^{-i\omega t}$ is considered and is suppressed throughout the chapter [114].

The EM wave propagation in a waveguide is precisely modeled by Maxwell's equations, with Faraday's law, as stated below, remaining universally applicable to various mediums, including cold plasma, vacuum, and dielectrics, providing a fundamental basis for understanding wave behavior in these environments.

$$\nabla \times \mathbf{E} = i\omega \mathbf{B}. \tag{4.2}$$

However, the Ampere's law acts differently in each of these mediums and is discussed in the next subsection.

For a two dimensional cylindrical waveguide $(\partial/\partial\theta = 0)$, the EM fields $\mathbf{E} = (E_r, E_\theta, E_z)$ and $\mathbf{B} = (B_r, B_\theta, B_z)$ include longitudinal components E_z and B_z

and transverse components E_r, E_θ, B_r and B_θ. To depict EM wave propagation, the Helmholtz equation, which is deduced from Maxwell's equations, is solved in conjunction with applicable boundary and interface conditions. In the scenario where walls are PEC, Maxwell's equations dictate that the tangential component of the electric field and the normal component of the magnetic field exhibit continuous behavior across the boundary $\partial\Omega$. Mathematically, for TM case, these conditions imply

$$(\mathbf{E} \times \boldsymbol{n})\,|_{\partial\Omega} = 0, \tag{4.3}$$

$$(\mathbf{H} \cdot \boldsymbol{n})\,|_{\partial\Omega} = 0, \tag{4.4}$$

where $\boldsymbol{t}$ is the tangent and $\boldsymbol{n}$ is the normal to the boundary $\partial\Omega$.
In case of TM wave, the continuity conditions at interface are stated as

$$(E_{z2} - E_{z1})|_{\partial\Omega} = 0, \tag{4.5}$$

$$\left.\left(\left(\frac{1}{\mu_2}\nabla E_{z2} - \frac{1}{\mu_1}\nabla E_{z1}\right) \cdot \boldsymbol{n}\right)\right|_{\partial\Omega} = 0, \tag{4.6}$$

where the subscripts 1 and 2 stand for any two mediums labeled as medium 1 and medium 2, along with permeabilities μ_1 and μ_2, respectively. The regions that contain vacuum i. e., $|z| > L, 0 < r < a$, and $|z| < L, h_1 < r < h_2$ are denoted by R_1, R_3 and R_5, respectively. Likewise, R_2 represents the region $|z| < L, 0 < r < h_1$ comprising of cold plasma and R_4 denotes the region $|z| < L, h_2 < r < a$ containing dielectric.

4.1.1 Traveling Wave Formulation in Vacuum

In context of vacuum, Ampere's law is formulated as:

$$\nabla \times \mathbf{B} = -\frac{i\omega}{c^2}\mathbf{E}. \tag{4.7}$$

The longitudinal components satisfy the Helmholtz equation

$$\left(\nabla^2 + \frac{\omega^2}{c^2}\right)\begin{pmatrix} E_z \\ B_z \end{pmatrix} = \begin{pmatrix} 0 \\ 0 \end{pmatrix}, \tag{4.8}$$

and the transverse components can be given as

$$E_r = \frac{is}{\lambda^2}\frac{\partial E_z}{\partial r}, \quad E_\theta = -\frac{i\omega}{\lambda^2}\frac{\partial B_z}{\partial r},$$

$$B_r = \frac{is}{\lambda^2}\frac{\partial B_z}{\partial r}, \quad B_\theta = \frac{ik_0^2}{\omega\lambda^2}\frac{\partial E_z}{\partial r},$$

where, $\lambda^2 = k_0^2 - s^2$.

The electric scalar field potentials in regions R_1, R_3, and R_5, which contain vacuum, are denoted as ϕ_1, ϕ_3, and ϕ_5, respectively. The boundary condition at the PEC wall, representing the zero tangential field component at the wall, in regions $|z| > L$ at $r = a$, and in region $|z| < L$ at $r = h_1, h_2$, can be expressed as:

$$\frac{\partial \phi_1}{\partial r}(a, z) = 0 = \frac{\partial \phi_5}{\partial r}(a, z), \tag{4.9}$$

$$\frac{\partial \phi_3}{\partial r}(h_1, z) = 0, \tag{4.10}$$

$$\frac{\partial \phi_3}{\partial r}(h_2, z) = 0. \tag{4.11}$$

The equation (4.8) represents an eigenvalue problem. The resultant eigenvalues provide important information about the dynamics of the above-mentioned problem by using linear equations. Deploying separation of variable technique, the dimensional equation (4.8) yields the eigenfunction expansion as follows [119, 121]:

$$\phi_1(r, z) = e^{ik_0(z+L)} + \sum_{n=0}^{\infty} A_n e^{-is_n(z+L)} R_n(r), \tag{4.12}$$

$$\phi_3(r, z) = \sum_{n=0}^{\infty} \left(B_n^{(II)} e^{is_n^{(II)} z} + C_n^{(II)} e^{-is_n^{(II)} z} \right) R_{2n}^{(II)}(r), \tag{4.13}$$

$$\phi_5(r, z) = \sum_{n=0}^{\infty} D_n e^{is_n(z-L)} R_n(r), \tag{4.14}$$

where $A_n, B_n^{(II)}, C_n^{(II)}$ and D_n express the amplitudes in regions R_1, R_3 and R_5. Moreover, the propagating modes in these regions contain wavenumbers $s_n = \sqrt{k_0^2 - \eta_n^2}$, $s_n^{(II)} = \sqrt{k_0^2 - \lambda_n^2}$. The eigenfunctions in the regions R_1 and R_5, can be expressed as

$$R_n(r) = J_0(\eta_n r), \;\; n = 0, 1, 2, \cdots,$$

where $J_0(.)$ and $N_0(.)$ represent the Bessel functions of first and second kinds with zero order. Here, $J_0^{'}(.)$ and $N_0^{'}(.)$ indicate the derivatives of the Bessel functions with respect to radius r. After applying condition (4.10), the eigenfunctions in region R_3 exhibit the following form

$$R_{2n}^{(II)}(r) = \frac{C_0}{N_0^{'}(\lambda_n h_1)} \left\{ N_0^{'}(\lambda_n h_1) J_0(\lambda_n r) - J_0^{'}(\lambda_n h_1) N_0(\lambda_n r) \right\}.$$

These eigenfunctions satisfy the usual orthogonality relations,

$$\int_0^a R_m(r) R_n(r) r dr = \delta_{mn} E_m,$$

$$\int_{h_1}^{h_2} R_{2m}^{(II)}(r) R_{2n}^{(II)}(r) r dr = \delta_{mn} E_{2m}^{(II)},$$

such that $E_n = \int_0^a R_n^2(r) r dr$, and $E_{2n}^{(II)} = \int_{h_1}^{h_2} R_{2n}^{(II)2}(r) r dr$ and δ_{mn} represents Kronecker delta. It is important to note that η_n and λ_n; $n = 0, 1, 2, \ldots$ express the eigenvalues associated with eigenfunctions $R_n(r)$ and $R_n^{(II)}(r)$, respectively. Through the implication of boundary conditions (4.9) and (4.11), it is found that η_n and λ_n satisfy the dispersion relations

$$J_0^{'}(\eta_n a) = 0, \tag{4.15}$$

$$N_0^{'}(\lambda_n h_1) J_0^{'}(\lambda_n h_2) - J_0^{'}(\lambda_n h_1) N_0^{'}(\lambda_n h_2) = 0. \tag{4.16}$$

To determine these eigenvalues, we can numerically solve (4.15) and (4.16) for their roots using methods such as Newton-Raphson method or the Secant method.

It is pertinent to mention here that the systems featuring complex eigenvalues, eigenfunctions, generalized orthogonality conditions, and the point-wise convergence of generalized series are thoroughly detailed in [111]-[112].

4.1.2 Traveling Wave Formulation in Cold Plasma

The Ampere's law for cold plasma can be stated as:

$$\nabla \times \mathbf{B} = -\frac{i\omega}{c^2} \bar{\epsilon}.\mathbf{E}. \tag{4.17}$$

In the context of cold, unmagnetized plasma, as discussed in [117], the Helmholtz equation is formulated in terms of the longitudinal components of the fields,

$$\left\{\nabla^2 + \frac{\omega^2}{c^2}\left(1 - \frac{\omega_p^2}{\omega^2}\right)\right\}\begin{pmatrix} E_z \\ B_z \end{pmatrix} = \begin{pmatrix} 0 \\ 0 \end{pmatrix}. \tag{4.18}$$

Meanwhile, the longitudinal components also serve as a basis for calculating the transverse components, as shown in the following expressions

$$E_r = \frac{is}{\tau^2}\frac{\partial E_z}{\partial r}, \quad E_\theta = -\frac{i\omega}{\tau^2}\frac{\partial B_z}{\partial r},$$

$$B_r = \frac{is}{\tau^2}\frac{\partial B_z}{\partial r}, \quad B_\theta = \frac{i\omega^2/c^2\left(1 - \omega_p^2/\omega^2\right)}{\omega\tau^2}\frac{\partial E_z}{\partial r},$$

where $\tau^2 = \frac{\omega^2}{c^2}\left(1 - \frac{\omega_p^2}{\omega^2}\right) - s^2$.

The boundary condition at the PEC wall $r = h_1$, representing the zero tangential field component at the wall in this region, can be expressed as follows:

$$\frac{\partial \phi_2}{\partial r}(h_1, z) = 0. \tag{4.19}$$

Invoking the variable separable technique to equation (4.18), the following expression represents the eigenfunction expansion:

$$\phi_2(r, z) = \sum_{n=0}^{\infty}\left(B_n^{(I)} e^{is_n^{(II)}z} + C_n^{(II)} e^{-is_n^{(I)}z}\right) R_{2n}^{(I)}(r), \tag{4.20}$$

where $B_n^{(I)}$ and $C_n^{(I)}$ reveal the amplitudes in regions R_2 and $s_n^{(I)} = \sqrt{k_1^2 - \tau_n^2}$ reveals the wavenumber of nth mode, where $k_1^2 = \frac{\omega^2}{c^2}\left(1 - \frac{\omega_p^2}{\omega^2}\right)$. The eigenfunctions, in this region, are expressed as

$$R_{2n}^{(I)}(r) = B_0 J_0(\tau_n r).$$

The functions $R_{2n}^{(I)}(r)$ satisfy the usual orthogonality relation,

$$\int_0^{h_1} R_{2m}^{(I)}(r) R_{2n}^{(I)}(r) r dr = \delta_{mn} E_{2m}^{(I)},$$

where $E_{2n}^{(I)} = \int_0^{h_1} R_{2n}^{(I)2}(r) r dr$. Here, $\tau_n;\ n = 0, 1, 2, \ldots$ represent the eigenvalues associated with the eigenfunctions $R_{2n}^{(I)}(r)$. By applying boundary condition (4.19), we establish that these eigenvalues satisfy the relation

$$J_0'(\tau_n h_1) = 0, \tag{4.21}$$

whereas, for $\tau_n;\ n = 0, 1, 2, \ldots$ we numerical solve (4.21) for their roots.

4.1.3 Traveling Wave Formulation in Dielectric Medium

The dielectrics are governed by Ampere's law in following manner:

$$\nabla \times \mathbf{B} = -i\omega\epsilon_d\mu_0\mathbf{E}. \tag{4.22}$$

The Helmholtz equation, in case of propagation in dielectric medium, is expressed in longitudinal components as

$$\left(\nabla^2 + \omega^2\epsilon_d\mu_0\right)\begin{pmatrix} E_z \\ B_z \end{pmatrix} = \begin{pmatrix} 0 \\ 0 \end{pmatrix}, \tag{4.23}$$

while the transverse components are stated as

$$E_r = \frac{is}{\chi^2}\frac{\partial E_z}{\partial r}, \quad E_\theta = -\frac{i\omega}{\chi^2}\frac{\partial B_z}{\partial r},$$

$$B_r = \frac{is}{\chi^2}\frac{\partial B_z}{\partial r}, \quad B_\theta = \frac{i\omega^2\epsilon_d\mu_0}{\omega\chi^2}\frac{\partial E_z}{\partial r},$$

where, $\chi^2 = \omega^2\epsilon_d\mu_0 - s^2$. The boundary conditions at the PEC walls located at $r = h_2$ and $r = a$ in this region can be expressed as

$$\frac{\partial\phi_4}{\partial r}(h_2, z) = 0, \tag{4.24}$$

$$\frac{\partial\phi_4}{\partial r}(a, z) = 0. \tag{4.25}$$

By applying method of separation of variables to dimensional equation (4.23), the eigenfunction expansion can be presented as:

$$\phi_4(r,z) = \sum_{n=0}^{\infty} \left(B_n^{(III)} e^{is_n^{(III)}z} + C_n^{(III)} e^{-is_n^{(III)}z} \right) R_{2n}^{(III)}(r), \tag{4.26}$$

where $B_n^{(III)}$ and $C_n^{(III)}$ reveal the amplitudes in regions R_4. The wavenumber of nth mode is in the form $s_n^{(III)} = \sqrt{k_2^2 - \chi_n^2}$, where $k_2^2 = \omega^2 \epsilon_d \mu_0$.
The boundary condition (4.24) yields the eigenfunctions, in this region, as

$$R_{2n}^{(III)}(r) = \frac{D_0}{N_0'(\chi_n h_2)} \left\{ N_0'(\chi_n h_2) J_0(\chi_n r) - J_0'(\chi_n h_2) N_0(\chi_n r) \right\}.$$

The usual orthogonality relations are satisfied by these functions,

$$\int_{h_2}^{a} R_{2m}^{(III)}(r) R_{2n}^{(III)}(r) r dr = \delta_{mn} E_{2m}^{(III)},$$

where $E_{2n}^{(III)} = \int_{h_2}^{a} R_{2n}^{(III)2}(r) r dr$. By using the boundary condition (4.25), we determine the eigenvalues $\chi_n; n = 0, 1, 2, \cdots$, that satisfy the equation (4.27) as follows:

$$N_0'(\chi_n h_2) J_0'(\chi_n a) - J_0'(\chi_n h_2) N_0'(\chi_n a) = 0. \tag{4.27}$$

Subsequently, we numerically find the roots of (4.27) to obtain the associated eigenvalues $\chi_n; n = 0, 1, 2, \cdots$.

4.1.4 Matching Conditions

The amplitudes of the propagating modes used in the expansions are still unknown, and these can be determined by matching the fields at interfaces $z = -L$ and $z = L$. This matching is based on the continuity of fields at the interfaces, resulting in the following matching conditions:

$$\phi_1(r,-L) = \begin{cases} \phi_2(r,-L), \\ \phi_3(r,-L), \\ \phi_4(r,-L), \end{cases} \tag{4.28}$$

$$\frac{\partial \phi_1}{\partial z}(r,-L) = \frac{\partial \phi_p}{\partial z}(r,-L), \tag{4.29}$$

$$\phi_5(r,L) = \begin{cases} \phi_2(r,L), \\ \phi_3(r,L), \\ \phi_4(r,L), \end{cases} \tag{4.30}$$

$$\frac{\partial \phi_5}{\partial z}(r,L) = \frac{\partial \phi_p}{\partial z}(r,L), \tag{4.31}$$

where $p = 2,3,4$. The next section explains the mode-matching procedure, which results in linear algebraic systems with unknown amplitudes.

4.2 MM Solution

The matching conditions outlined in the previous section are employed to calculate the unknown coefficients $A_n, B_n^{(j)}, C_n^{(j)}, D_n, ; j = I, II, III$. Based on condition (4.28), we obtain

$$1+\sum_{n=0}^{\infty} A_n R_n(r) = \begin{cases} \sum_{n=0}^{\infty} \left(B_n^{(I)} e^{-is_n^{(I)}L} + C_n^{(I)} e^{is_n^{(I)}L}\right) R_{2n}^{(I)}(r), & 0 \le r \le h_1, \\ \sum_{n=0}^{\infty} \left(B_n^{(I)} e^{-is_n^{(II)}L} + C_n^{(II)} e^{is_n^{(II)}L}\right) R_{2n}^{(I)}(r), & h_1 \le r \le h_2, \\ \sum_{n=0}^{\infty} \left(B_n^{(III)} e^{-is_n^{(III)}L} + C_n^{(III)} e^{is_n^{(III)}L}\right) R_{2n}^{(I)}(r), & h_2 \le r \le a. \end{cases} \tag{4.32}$$

Multiplying both the sides by $R_m(r)r$ and integrating with respect to r from 0 to a, we get

$$\begin{aligned} A_m = -\delta_{m0} &+ \frac{1}{E_m} \sum_{n=0}^{\infty} \left(B_n^{(I)} e^{-is_n^{(I)}L} + C_n^{(I)} e^{is_n^{(I)}L}\right) P_{mn} \\ &+ \frac{1}{E_m} \sum_{n=0}^{\infty} \left(B_n^{(II)} e^{-is_n^{(II)}L} + C_n^{(II)} e^{is_n^{(II)}L}\right) Q_{mn} \\ &+ \frac{1}{E_m} \sum_{n=0}^{\infty} \left(B_n^{(III)} e^{-is_n^{(III)}L} + C_n^{(III)} e^{is_n^{(III)}L}\right) R_{mn}, \end{aligned} \tag{4.33}$$

where δ_{mn} represents the Kronecker delta, such that

$$\delta_{mn} = \begin{cases} 0, m \neq n, \\ 1, m = n. \end{cases}$$

The quantities P_{mn}, Q_{mn} and R_{mn} can be stated as

$$P_{mn} = \int_0^{h_1} R_m(r)R_{2n}^{(I)}(r)rdr, \quad Q_{mn} = \int_{h_1}^{h_2} R_m(r)R_{2n}^{(II)}(r)rdr,$$

$$R_{mn} = \int_{h_2}^{a} R_m(r)R_{2n}^{(III)}(r)rdr.$$

The matching condition (4.29) implies

$$k_0 - \sum_{n=0}^{\infty} A_n s_n R_n(r) = \sum_{n=0}^{\infty} \left(B_n^{(I)} e^{-is_n^{(I)}L} - C_n^{(I)} e^{is_n^{(I)}L}\right) s_n^{(I)} R_{2n}^{(I)}(r),$$
$$0 \le r \le h_1, \qquad (4.34)$$

$$k_0 - \sum_{n=0}^{\infty} A_n s_n R_n(r) = \sum_{n=0}^{\infty} \left(B_n^{(II)} e^{-is_n(II)L} - C_n^{(II)} e^{is_n^{(II)}L}\right) s_n^{(II)} R_{2n}^{(II)}(r),$$
$$h_1 \le r \le h_2, \quad (4.35)$$

$$k_0 - \sum_{n=0}^{\infty} A_n s_n R_n(r) = \sum_{n=0}^{\infty} \left(B_n^{(III)} e^{-is_n^{(III)}L} - C_n^{(III)} e^{is_n^{(III)}L}\right) s_n^{(III)} R_{2n}^{(III)}(r),$$
$$h_2 \le r \le a. (4.36)$$

By multiplying (4.34) with $R_{2m}^{(I)}r$, integrating from 0 to h_1 and simplifying, we get

$$B_m^{(I)} e^{-is_m^{(I)}L} - C_m^{(I)} e^{is_m^{(I)}L} = \frac{1}{s_m^{(I)} E_{2m}^{(I)}} \left\{ k_0 P_{0m} - \sum_{n=0}^{\infty} A_n s_n P_{nm} \right\}. \qquad (4.37)$$

Again solving the equations (4.35) and (4.36) and a similar rearrangement leads to the following equations,

$$B_m^{(II)} e^{-is_m^{(II)}L} - C_m^{(II)} e^{is_m^{(II)}L} = \frac{1}{s_m^{(II)} E_{2m}^{(II)}} \left\{ k_0 Q_{0m} - \sum_{n=0}^{\infty} A_n s_n Q_{nm} \right\}, \qquad (4.38)$$

$$B_m^{(III)} e^{-is_m^{(III)}L} - C_m^{(III)} e^{is_m^{(III)}L} = \frac{1}{s_m^{(III)} E_{2m}^{(III)}} \left\{ k_0 R_{0m} - \sum_{n=0}^{\infty} A_n s_n R_{nm} \right\}. \qquad (4.39)$$

The matching condition (4.30) yields

$$\begin{aligned}D_m = \frac{1}{E_m}\sum_{n=0}^{\infty}\left(B_n^{(I)}e^{is_n^{(I)}L} + C_n^{(I)}e^{-is_n^{(I)}L}\right)P_{mn}\\ +\frac{1}{E_m}\sum_{n=0}^{\infty}\left(B_n^{(II)}e^{is_n^{(II)}L} + C_n^{(II)}e^{-is_n^{(II)}L}\right)Q_{mn}\\ +\frac{1}{E_m}\sum_{n=0}^{\infty}\left(B_n^{(III)}e^{is_n^{(III)}L} + C_n^{(III)}e^{-is_n^{(III)}L}\right)R_{mn}.\end{aligned} \tag{4.40}$$

Deploying the matching condition (4.31) gives rise to the following equations,

$$B_m^{(I)}e^{is_m^{(I)}L} - C_m^{(I)}e^{-is_m^{(I)}L} = \frac{1}{s_m^{(I)}E_{2m}^{(I)}}\sum_{n=0}^{\infty}D_n s_n P_{nm}, \tag{4.41}$$

$$B_m^{(II)}e^{is_m^{(II)}L} - C_m^{(II)}e^{-is_m^{(II)}L} = \frac{1}{s_m^{(II)}E_{2m}^{(II)}}\sum_{n=0}^{\infty}D_n s_n Q_{nm}, \tag{4.42}$$

$$B_m^{(III)}e^{is_m^{(III)}L} - C_m^{(III)}e^{-is_m^{(III)}L} = \frac{1}{s_m^{(III)}E_{2m}^{(III)}}\sum_{n=0}^{\infty}D_n s_n R_{nm}. \tag{4.43}$$

Adding the equations (4.33) and (4.40), leads to

$$\begin{aligned}\Psi_m^+ = -\delta_{m0} + \frac{2}{E_m}\sum_{n=0}^{\infty}\Phi_{In}^+\cos(s_n^{(I)}L)P_{mn} + \frac{2}{E_m}\sum_{n=0}^{\infty}\Phi_{IIn}^+\cos(s_n^{(II)}L)Q_{mn}\\ +\frac{2}{E_m}\sum_{n=0}^{\infty}\Phi_{IIIn}^+\cos(s_n^{(III)}L)R_{mn}.\end{aligned} \tag{4.44}$$

Subtracting (4.40) from (4.33), submits

$$\begin{aligned}\Psi_m^- = -\delta_{m0} - \frac{2i}{E_m}\sum_{n=0}^{\infty}\Phi_{In}^-\sin(s_n^{(I)}L)P_{mn} - \frac{2i}{E_m}\Phi_{IIn}^-\sin(s_n^{(II)L})Q_{mn}\\ -\frac{2i}{E_m}\Phi_{IIIn}^-\sin(s_n^{(III)}L)R_{mn},\end{aligned} \tag{4.45}$$

where $\Psi_m^{\pm} = A_m \pm D_m$ and $\Phi_{jm}^{\pm} = B_m^{(j)} \pm C_m^{(j)}, j = I, II, III.$

Subtracting (4.37) from (4.41), we get

$$\Phi_{Im}^+ = \frac{i}{2s_m^{(I)}E_{2m}^{(I)}\sin(s_m^{(I)}L)}\left(k_0P_{0m} - \sum_{n=0}^{\infty}\Psi_n^+ s_n P_{nm}\right). \tag{4.46}$$

Similarly, subtracting (4.38) from (4.42) and (4.39) from (4.43), respectively, yield Φ^+_{IIm} and Φ^+_{IIIm} as follows

$$\Phi^+_{IIm} = \frac{i}{2s_m^{(II)} E_{2m}^{(II)} \sin(s_m^{(II)} L)} \left(k_0 Q_{0m} - \sum_{n=0}^{\infty} \Psi_n^+ s_n Q_{nm} \right), \tag{4.47}$$

$$\Phi^+_{IIIm} = \frac{i}{2s_m^{(III)} E_{2m}^{(III)} \sin(s_m^{(III)} L)} \left(k_0 R_{0m} - \sum_{n=0}^{\infty} \Psi_n^+ s_n R_{nm} \right). \tag{4.48}$$

Now, respective adding of (4.37) and (4.41), (4.38) and (4.42), (4.39) and (4.43), leads to the formation of $\Phi^-_{Im}, \Phi^-_{IIm}$ and Φ^-_{IIm} in the following way:

$$\Phi^-_{Im} = \frac{1}{2s_m^{(I)} E_{2m}^{(I)} \cos(s_m^{(I)} L)} \left(k_0 P_{0m} - \sum_{n=0}^{\infty} \Psi_n^- s_n P_{nm} \right), \tag{4.49}$$

$$\Phi^-_{IIm} = \frac{1}{2s_m^{(II)} E_{2m}^{(II)} \cos(s_m^{(II)} L)} \left(k_0 Q_{0m} - \sum_{n=0}^{\infty} \Psi_n^- s_n Q_{nm} \right), \tag{4.50}$$

$$\Phi^-_{IIIm} = \frac{1}{2s_m^{(III)} E_{2m}^{(III)} \cos(s_m^{(III)} L)} \left(k_0 R_{0m} - \sum_{n=0}^{\infty} \Psi_n^- s_n R_{nm} \right). \tag{4.51}$$

The equations (4.44)-(4.51) divulge a system of infinite equations having the unknown coefficients $\left\{ A_n, B_n^{(j)}, C_n^{(j)}, D_n \right\}$, $j = I, II, III$. The system is truncated and is solved numerically and the results will be probed in the section of numerical discussion.

4.3 Energy Flux

The proper understanding of the energy flux allows for the measurement of the accuracy and convergence of an approximate solution. In order to calculate the energy propagating in duct regions, we use the Poynting vector [123],

$$Power = \int_R \pi r Re\left\{E_z\left(\frac{\partial E_z}{\partial z}\right)^*\right\} dr, \tag{4.52}$$

where (*) represents complex conjugate. Applying the Poynting vector, the quantification of the incident power P_i, P_r and P_t provides,

$$P_i = \frac{\pi k_0 a^2}{2}, \tag{4.53}$$

$$P_r = -\pi Re\left(\sum_{n=0}^{\infty}|A_n|^2 s_n^* E_n\right), \tag{4.54}$$

$$P_t = \pi Re\left(\sum_{n=0}^{\infty}|D_n|^2 s_n^* E_n\right). \tag{4.55}$$

Since $Re(s_n^*) = Re(s_n)$, therefore, (4.54) and (4.55) take the form,

$$P_r = -\pi Re\left(\sum_{n=0}^{\infty}|A_n|^2 s_n E_n\right), \tag{4.56}$$

$$P_t = \pi Re\left(\sum_{n=0}^{\infty}|D_n|^2 s_n E_n\right). \tag{4.57}$$

The principle of conservation of energy states,

$$P_i + P_r = P_t.$$

Applying this principle, yields

$$\frac{\pi k_0 a^2}{2} - \pi Re\left(\sum_{n=0}^{\infty}|A_n|^2 s_n E_n\right) = \pi Re\left(\sum_{n=0}^{\infty}|D_n|^2 s_n E_n\right). \tag{4.58}$$

Scaling the incident power P_i to unity, the equation (4.58) is modified as

$$1 = \mathcal{E}_1 + \mathcal{E}_2, \tag{4.59}$$

where

$$\mathcal{E}_1 = \frac{2}{k_0 a^2} Re\left(\sum_{n=0}^{\infty}|A_n|^2 s_n E_n\right),$$

$$\mathcal{E}_2 = \frac{2}{k_0 a^2} Re \left(\sum_{n=0}^{\infty} |D_n|^2 s_n E_n \right).$$

4.4 Numerical Results and Discussion

The results of numerical solution of the given physical problem are furnished in this section. The physical parameters chosen is speed of light, $c = 3 \times 10^8$ meter/second, permittivity of free space $\epsilon_0 = 8.85 \times 10^{-12}$ F/m (Farad per meter) and its permeability $\mu_0 = 4\pi \times 10^{-7}$ N/A^2(Newtons per Ampere squared). The numerical calculations are carried out by using the software Mathematica (versions 12.1).

The solutions are obtained after truncating the systems to finite number equations. The acquired solution is thus employed for confirmation of the accuracy of algebra, power distribution and its conservation.

The results for both frequency regimes, i.e., transparency ($\omega > \omega_p$) and non-transparency ($\omega < \omega_p$) are also achieved. For transparency regime, the angular and plasma frequencies are set as $\omega = 2.5 \times 10^9$ radian/second and $\omega_p = 2 \times 10^9$ radian/second. The computations in the case of non-transparency regime are conducted by fixing the frequencies as: $\omega = 2 \times 10^9$ radian/second and $\omega_p = 2.5 \times 10^9$ radian/second.

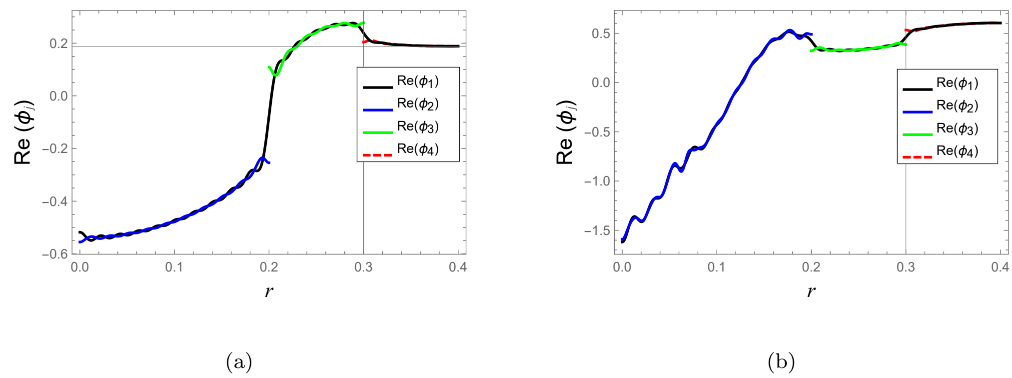

FIGURE 4.2: Real parts of the electric field in (a) transparency, and (b) non-transparency regions at $z = -L$.

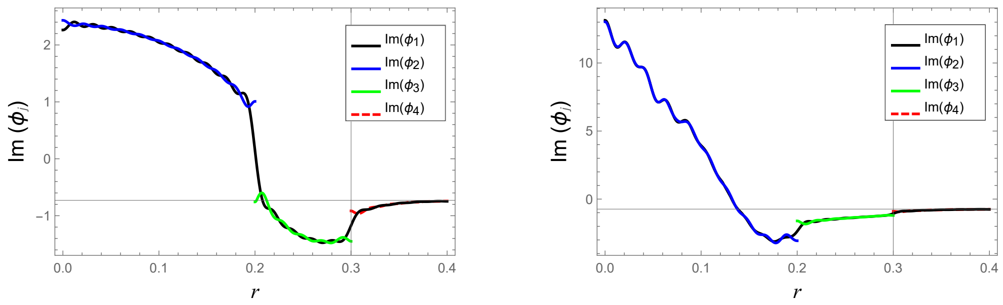

(a) (b)

FIGURE 4.3: Imaginary parts of the electric field in (a) transparency, and (b) non-transparency regions at $z = -L$.

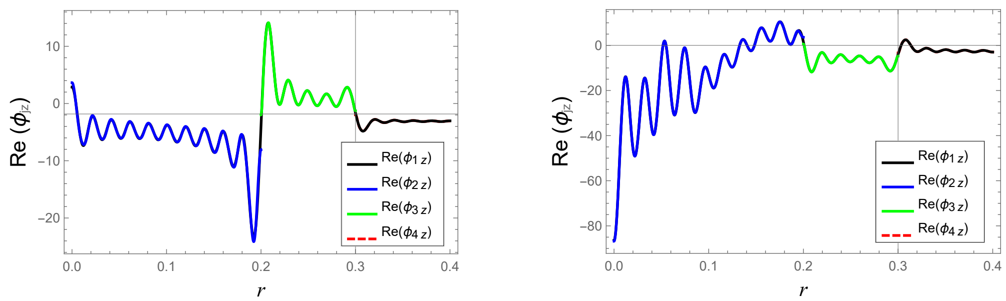

(a) (b)

FIGURE 4.4: Real parts of the magnetic field in (a) transparency, and (b) non-transparency regions at $z = -L$.

After setting the relevant duct radii to $a = 0.4$ cm, $h_1 = 0.2$ cm and $h_2 = 0.3$ cm, the matching conditions at the two interfaces $x = -L$ and $x = L$ are reconstructed. The length of the central chamber is fixed as $2 \times L = 2 \times 0.5$ cm. The system revealed in the equations (4.44)-(4.51) is truncated up to 120 terms. The solution of these equations yields the unknowns $\left\{A_n, B_n^{(j)}, C_n^{(j)}, D_n\right\}$; $j = I, II, III$; $n = 0, 1, 2, \ldots, 119$.

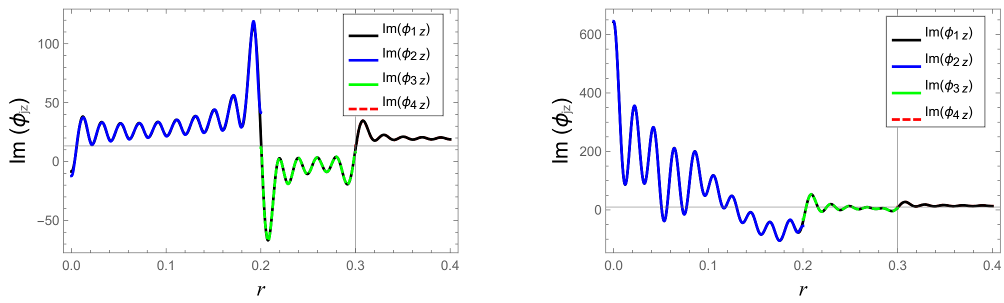

(a) (b)

FIGURE 4.5: Imaginary parts of the magnetic field in (a) transparency, and (b) non-transparency regions at $z = -L$.

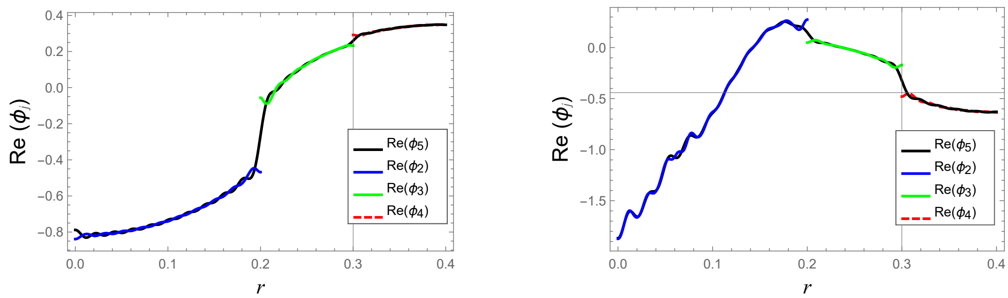

(a) (b)

FIGURE 4.6: Real parts of electric field in (a) transparency, and (b) non-transparency regions at $z = L$.

The figures 4.2-4.9 present validation of the MM solution with the help of matching conditions of the dimensional magnetic and electric fields, respectively, at the interfaces $z = \pm L$. These figures reveal the real and imaginary components of tangential electric and magnetic fields versus r in both transparency and non-transparency frequency regimes. The peaks observed in the graph of matching conditions of real and imaginary parts of magnetic field potential, the derivative of the electric field with respect to z, represent the discontinuity at the edges. However, in all mediums, i.e., cold plasma, vacuum and dielectric, the graphs of magnetic and electric fields reveal that the real and imaginary parts are in excellent agreement along the interfaces.

The accuracy of algebra is established also through the conservation of energy in different duct regions. The reflected power in left duct ($z < -L$) is represented by

$\mathcal{E}_1$. The quantity $\mathcal{E}_2$ is the transmitted power in right duct ($z > L$). Here, $\mathcal{E}_t$ is the sum of powers in all duct regions,

$$\mathcal{E}_t = \mathcal{E}_1 + \mathcal{E}_2.$$

For the sake of comparison, the behavior of reflected and transmitted powers is analyzed in both transparency and non-transparency regions against angular frequency, plasma radius and chamber length.

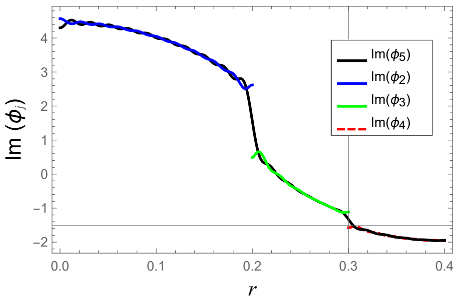

(a)

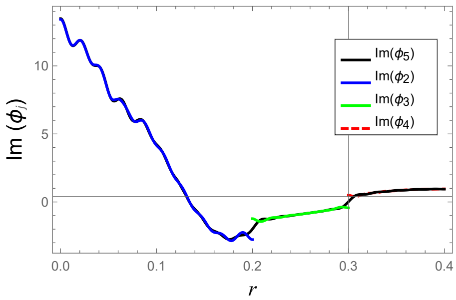

(b)

FIGURE 4.7: Imaginary parts of the electric field in (a) transparency, and (b) non-transparency regions at $z = L$.

For the plots of energy flux versus angular frequency ω, the values of duct radii and chamber length are taken to be $h_1 = 0.1$ cm, $h_2 = 0.2$ cm, $a = 0.4$ cm and $2 \times L = 2 \times 0.5$ cm. The resonant duct modes, for inlet and outlet regions, occur at points where s_n is zero or a complex number. The modes for $n = 1, 2, 3, \ldots$ become cut-on (energy propagating) when their mode wave number, s_n, becomes real. The complex value of s_n appears only if the medium and/or the bounding wall conditions become complex. Specifically, the cut-on modes appear for frequencies $\omega > c\eta_n$, where η_n are the roots of characteristic equation (4.15). Thus mode wave numbers, in all regions of the waveguide, depend on the respective roots of the characteristic equations.

The peak values and sudden fluctuations observed in the graphs depicting scattering powers versus frequency and duct radius (evident in figures 4.10-4.13) stem from the conversion of imaginary values to complex ones and vice versa. Additionally, fluctuations in the graphs are induced by trigonometric factors present within symmetric and anti-symmetric mode amplitudes as defined by equations (4.44)-(4.51).

In figure 4.10(a), the peaks appearing due to maximum values of reflection and transmission amplitudes, respectively, at $\omega = 2.16 \times 10^9$ radian/second and $\omega = 2.56 \times 10^9$ radian/second, represent the feature of resonance in the transparency regime. In the non-transparency regime, presented in Figure 4.10(b), the resonance behavior is observed when reflected power amplitude reaches its maximum at $\omega = 7.9 \times 10^8$ radian/second and $\omega = 1.63 \times 10^9$ radian/second.

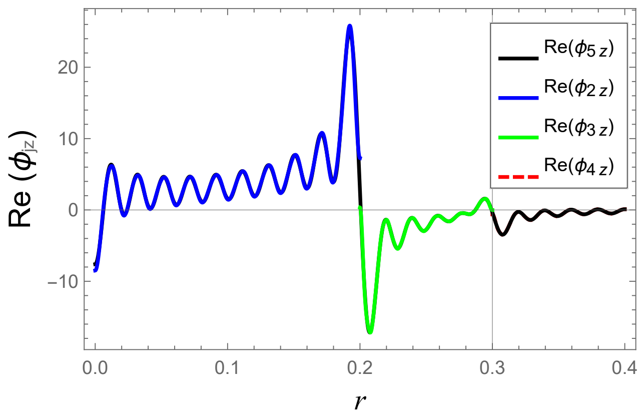

(a)

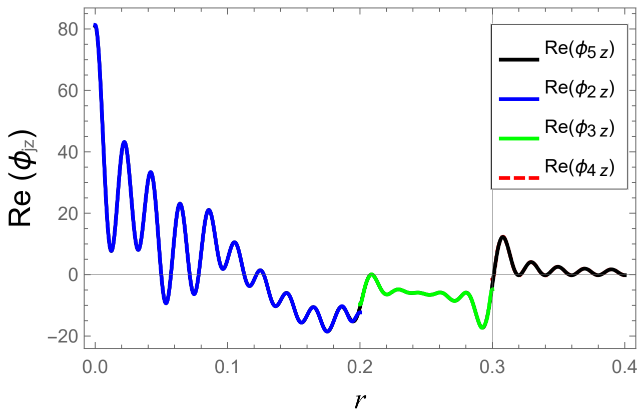

(b)

FIGURE 4.8: Real parts of the magnetic field in (a) transparency, and (b) non-transparency regions at $z = L$.

This section also discusses the impact of changes in material properties. Figure 4.11 compares the given cylindrical structure with a cylindrical waveguide containing dielectric in all duct regions in terms of power flux to explore this effect. Part (a) of the figure illustrates the reflected powers in both scenarios, while part (b) shows the transmitted powers in both geometries having distinct material properties. Considering the dielectric in all sections of the waveguide, it is evident that there is no reflection, leading to total transmission.

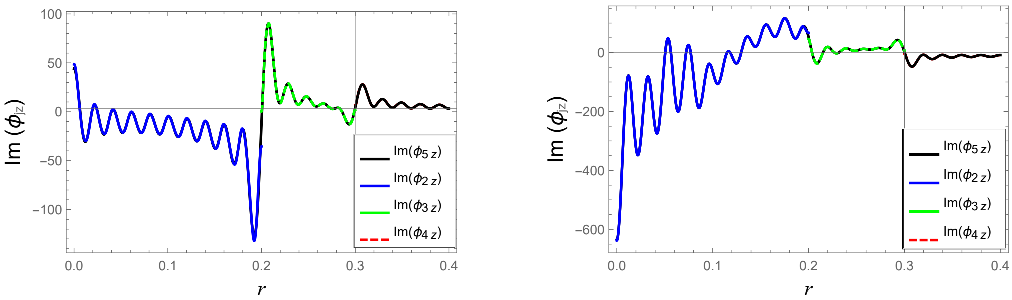

(a) (b)

FIGURE 4.9: Imaginary parts of the magnetic field in (a) transparency, and (b) non-transparency regions at $z = L$.

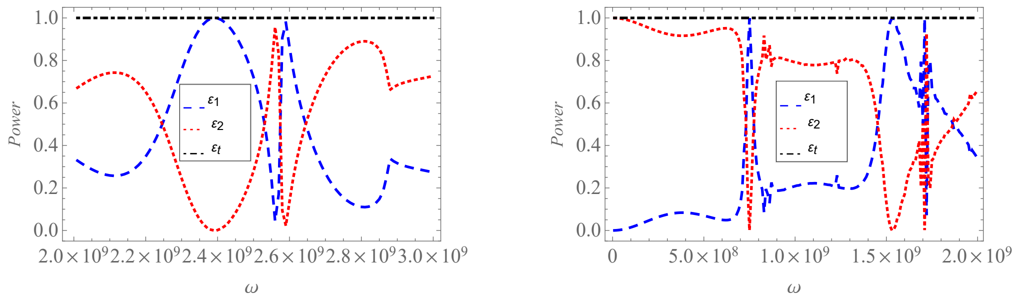

(a) (b)

FIGURE 4.10: Energy flux in (a) transparency, and (b) non-transparency regions versus the angular frequency ω.

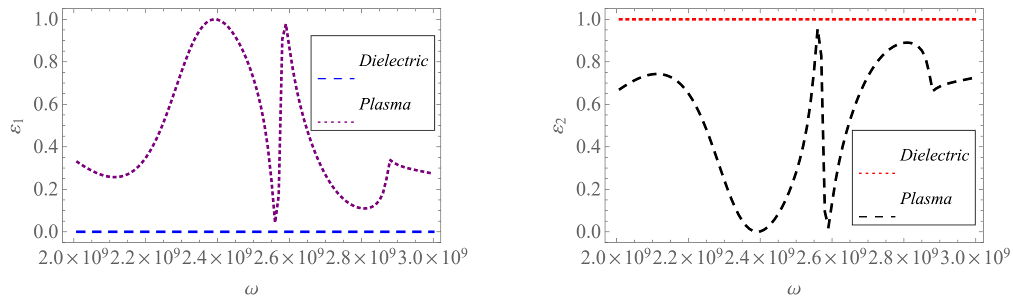

(a) (b)

FIGURE 4.11: Comparison of (a) reflected energy, and (b) transmitted energy, versus the angular frequency ω in dielectric and plasma settings .

The graphs of power flux plotted versus plasma radius h_1 for both frequency regimes are furnished in figures 4.12(a) and 4.12(b), respectively. The values of the radius h_1 are assumed to be $0 < h_1 < 0.5$ cm, while the radii of the other two sections of the duct are set to be $h_2 = 2 \times h_1$ (in cm) and $a = 3 \times h_1$ (in cm). The length of chamber is fixed as $2 \times L = 2 \times 0.5$ cm. In the two regimes, the increase in plasma radius implies the dominance of transmission of EM waves.

The plots of power flux for transparency and non-transparency regimes, versus chamber length L, are organized in figures 4.13(a) and 4.13(b). The chamber length is considered as $0 < L < 1$ cm, and radii are set as $h_1 = 0.1$ cm, $h_2 = 0.2$ cm and $a = 0.3$ cm. It is intriguing to notice that the increase in the length of this chamber shows almost same behavior of power in both regimes, but the power fluctuations are more rapid in non-transparency regime. It is evident from the figures 4.10-4.13 that energy conservation in scattering results is achieved, where the sum of reflected and transmitted powers is analytically formulated to be unity.

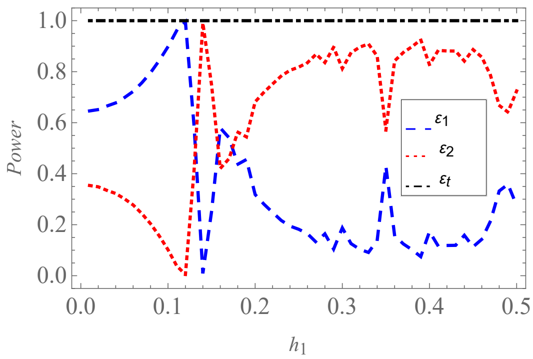

(a)

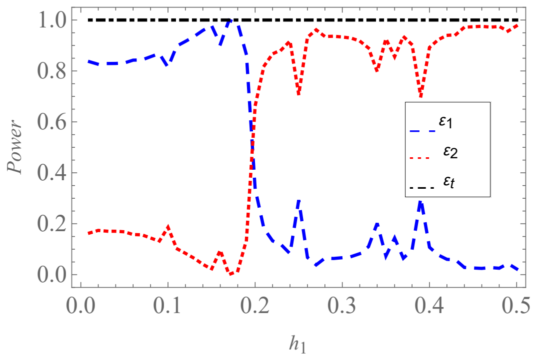

(b)

FIGURE 4.12: Energy flux in (a) transparency, and (b) non-transparency regions versus cold plasma radius h_1.

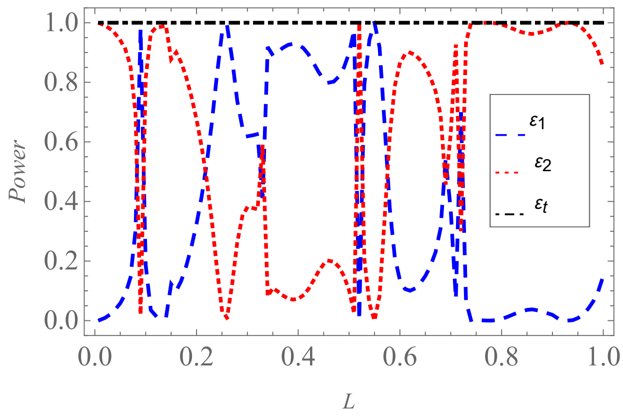

(a)

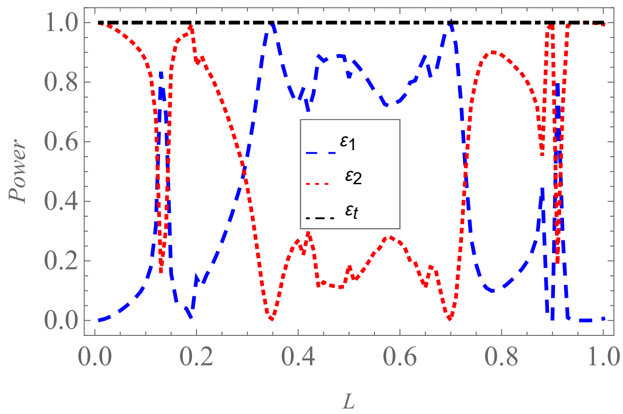

(b)

FIGURE 4.13: Energy flux in (a) transparency, and (b) non-transparency regions versus half the length of chamber L.

The convergence of solution is explored through the power conservation. The accuracy is checked up to six decimal places. The effect of the truncation becomes negligible when $N \geq 110$ as is obvious from table 4.1, which demonstrates that the power components match up to 1 decimal place when the systems are truncated to $N = 20$ terms. However, increasing the truncation parameter to 30 leads to a convergence of power components up to 3 decimal places, as evident from Figure 4.14, which also illustrates the convergence of power components and the satisfaction of the conserved power identity. Figure 4.14 also confirms that the solution remains convergent with rise in the truncation number N in the transparency regime in different sized waveguides. Figures 4.14(a) and 4.14(b) represent the convergence of reflected and transmitted powers, respectively. Therefore, this system of infinite algebraic equations can be handled as finite. The frequencies for this regime are already set as $\omega_p = 2 \times 10^9$ radian/second and $\omega = 2.5 \times 10^9$ radian/second, while radius h_1 is set to be $0.1, 0.01$ and 1 cm for three distinct sizes of waveguides, while the other two radii are taken as $h_2 = 2 \times h_1$ (in cm) and $a = 3 \times h_1$ (in cm).

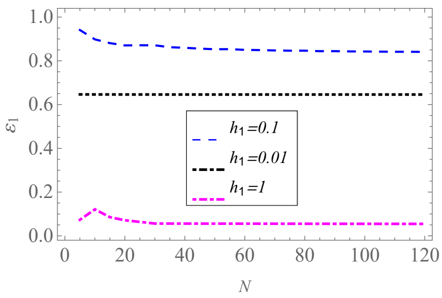

(a)

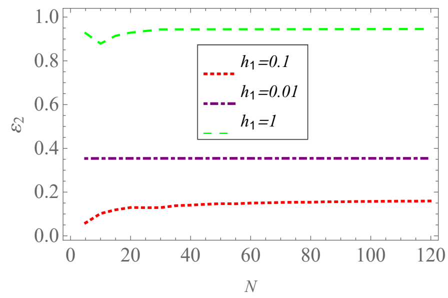

(b)

FIGURE 4.14: Power flux versus number of terms N in different sized cylindrical waveguides.

TABLE 4.1: Energy conservation versus number of terms N for $h_1 = 0.1$ cm.

Terms (N)	$\mathcal{E}_1$	$\mathcal{E}_2$	$\mathcal{E}_t$
10	0.330211	0.669789	1
20	0.349128	0.650872	1
30	0.326836	0.673164	1
40	0.326087	0.673913	1
50	0.329381	0.670619	1
60	0.324639	0.675361	1
70	0.323001	0.676999	1
80	0.320453	0.679547	1
90	0.321606	0.678394	1
100	0.321458	0.678542	1
110	0.322149	0.677851	1
120	0.321239	0.678761	1

Cut-on modes, within the central chamber, in regard to the plasma radius h_1 are also computed, which is set as $0 < h_1 < 0.5$ cm. In transparency regime, the increase in radius h_1 implicates constant number of these modes in all regions, i. e., the cold plasma, vacuum and dielectric exhibit one cut-on mode. However, in non-transparency regime, only one cut-on mode exists in the vacuum and dielectric regions, and no cut-on mode appears in plasma region. The impact on cut-on modes due to the variation in angular frequency ω is same as the effect of increasing plasma radius h_1. When the frequency range is 0.01×10^9 radian/second $< \omega < 2 \times 10^9$ radian/second, then there exists one cut-on mode in the regions containing the vacuum and dielectric but no cut-on mode is observed in plasma region. On the other hand, all the three regions including cold plasma display one cut-on mode for frequency ranging between 2.01×10^9 radian/second $< \omega < 3 \times 10^9$ radian/second.

Chapter 5

EM Wave Scattering in Plasma Beam Driven Waveguides under Strong Magnetic Field

The analysis of scattering of EM waves in a cold and uniform plasma-filled waveguide driven by an intense relativistic electron beam under a strong magnetic field is carried out in this chapter. Plasma, a state of matter consisting of charged particles, exhibits a strong interaction with EM waves. This interaction arises from the collective behavior of charged particles in the plasma medium when subjected to external EM fields. Due to this unique property, plasma has found potential applications in various types of waveguides. The literature indicates that various numerical techniques, including the MM method, have been applied to different types of slow wave structures to investigate EM phenomena. However, the outcomes of these studies were primarily limited to dispersion relations and electron dynamics. Therefore, the motivation for this study stems from the necessity to investigate the scattering characteristics, orthogonality relation, and power analysis within a plasma-filled cylindrical waveguide. The chapter comprises of two problems. The first problem pertains to scattering of EM waves through a semi-infinite plasma beam embedded in cold plasma in presence of a strong magnetic field in an infinite PEC cylindrical waveguide. The same beam plasma environment is considered within a central region of an infinite PEC cylindrical waveguide to investigate the scattering in the second problem. The two problems differ in eigenfunction expansions, interface conditions and the scattering coefficients. However, for both problems, the eigenfunctions and orthogonal properties in regions that have similar physical features remain same. The models presented can be applied as a traveling wave tube containing uniform cold plasma in a cylindrical structure under the influence of plasma beam.

This chapter is organized in nine sections. Sections 5.1-5.4 discuss the EM wave scattering in a cylindrical waveguide having electron beam enveloped between cold and collisionless plasma under strong magnetic field. The physical configuration of this problem is laid out in Section 5.1. Section 5.2 provides the MM solution of this slow wave structure. Section 5.3 delivers the validity of the law of power conservation. Section 5.4 gathers the detailed results obtained through numerical computations and their physical importance.

The scattering of EM waves through a same beam plasma environment in a central chamber of an infinite cylindrical waveguide is analyzed in Sections 5.5-5.9. The boundary value problem associated with the scattering is formulated in section 5.6. Section 5.7 renders the MM solution. Section 5.8 provides a rigorous proof of the power conservation principle, while Section 5.9 provides the validation of matching conditions and power analysis.

5.1 Formulation of Propagating Waves in an Electron Beam Embedded in Cold Plasma Environment

The wave problem investigated in this section revolves around scattering of EM waves in a cylindrical waveguide composed of an electron beam immersed in cold plasma under the influence of strong magnetic field. The scattering of EM waves is investigated within a PEC waveguide which is depicted in Figure (5.1). This infinite waveguide has PEC boundary at $r = a$. The propagation of a TM incident wave, having unit amplitude and making a zero incident angle with reference to the z axis, is considered in positive z direction from the left inlet $z < 0$ to interface at right. The region $z < 0$ comprises of vacuum and dielectric as shown in the figure, with PEC walls placed at $r = h_1$ and h_2. The beam in the right duct $z > 0$ is wrapped around by cold plasma at $r = h_1$. The permittivity and permeability of vacuum are represented as ϵ_0 and μ_0, respectively. This configuration corresponds to a wavenumber k_0 divulged as $k_0 = \omega\sqrt{\mu_0\epsilon_0}$, where ω represents the angular frequency and the speed of light c is related to free space permittivity and permeability as $c = 1/\sqrt{\epsilon_0\mu_0}$. This association gives a new description to k_0 expressed as $k_0 = \omega/c$. The permittivity ϵ_d in dielectric medium is assumed to be $\epsilon_d = 2 \times \epsilon_0$. Therefore the wavenumber in this medium can be manifested as $k_1 = \sqrt{2}k_0$. However, for the case of all mediums, i.e., beam, plasma and dielectric, the permeability remains μ_0.

A semi-finite intense and thick relativistic beam of density n_b, having a cold, collisionless, uniform plasma with density n_p, passes through the center of the waveguide. Here, the plasma, beam and cyclotron frequencies are given, respectively, as $\omega_p = (e^2 n_p/\epsilon_0 m)^{1/2}$, $\omega_b = (e^2 n_b/\epsilon_0 m)^{1/2}$ and $\omega_c = eB_0/m$. These frequencies involve B_0, m and e which indicate the magnetic field, electron mass and electric charge, respectively.

The permittivity tensor $\bar{\epsilon}$, is

$$\bar{\epsilon}_i = \begin{bmatrix} \epsilon_1 & -i\epsilon_2 & 0 \\ i\epsilon_2 & \epsilon_1 & 0 \\ 0 & 0 & \epsilon_{3i} \end{bmatrix}, \tag{5.1}$$

where $\epsilon_1 = 1 - \dfrac{\omega_p^2}{\omega^2 - \omega_c^2}, \epsilon_2 = \dfrac{\omega_c \omega_p^2}{\omega\left(\omega^2 - \omega_c^2\right)}$ [115]-[116].

In order to refrain from the association of the TE and TM modes, B_0 is considered very strong so that $|\epsilon_2|$ is infinitesimal and $\epsilon_1 = 1$ [118]. When $i = b$ then $\epsilon_{3b} = 1 - \dfrac{\omega_p^2}{\omega^2} - \dfrac{\omega_b^2}{\gamma^3(\omega - k_{nz}v)^2}$ [66]. These components form tensor for the beam. γ is the relativistic factor, $k_{nz} = k_0 + 2n\pi,\ n = 0, 1, 2, \ldots,$ is the axial wave number while v represents the beam velocity, such that $\gamma = \sqrt{1 - \dfrac{v^2}{c^2}}$. When $i = p$ then

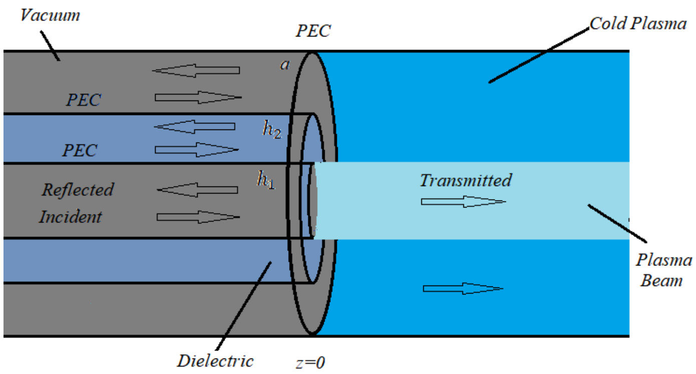

FIGURE 5.1: Propagation of EM waves in a cylindrical waveguide comprising of beam embedded in cold plasma.

$\epsilon_{3p} = 1 - \dfrac{\omega_p^2}{\omega^2}$. The tensor thus formed reveals the case of cold plasma. A time independent variant $e^{-i\omega t}$ is considered but ignored throughout this paper [114].

Maxwell's equations govern the propagation of the EM waves in a waveguide. The Faraday's law does not change for any of the four mediums, i.e., vacuum, dielectric, beam and cold plasma.

$$\nabla \times \mathbf{E} = i\omega \mathbf{B}. \tag{5.2}$$

However, the Ampere's law has a different behavior in each of these mediums and is discussed in the upcoming subsections.

In case of a two dimensional cylindrical waveguide, the fields remain invariant with respect to θ, i.e., $\partial/\partial\theta = 0$. For EM wave propagation, the Helmholtz equation derived from Maxwell's equations is solved along with boundary and interface conditions. The regions $z < 0, 0 < r < h_1$, and $z < 0, h_2 < r < a$ contain vacuum and are denoted by R_1, R_3, respectively. Likewise, R_2 represents the region $z < 0, h_1 < r < h_2$ and contains dielectric, R_4 denotes the region $z > 0, 0 < r < a$ which encircles plasma beam and the cold plasma.

5.1.1 Traveling Wave Formulation in Vacuum

The formulation of Ampere's law in vacuum is stated as:

$$\nabla \times \mathbf{B} = -\frac{i\omega}{c^2}\mathbf{E}. \tag{5.3}$$

The Helmholtz equation in terms of longitudinal components is given as

$$\left(\nabla^2 + \frac{\omega^2}{c^2}\right)\begin{pmatrix} E_z \\ B_z \end{pmatrix} = \begin{pmatrix} 0 \\ 0 \end{pmatrix}. \tag{5.4}$$

The longitudinal components are the source to compute

$$E_r = \frac{is}{\eta^2}\frac{\partial E_z}{\partial r}, \quad E_\theta = 0,$$

$$B_r = 0, \quad B_\theta = \frac{i\omega^2/c^2}{\omega\eta^2}\frac{\partial E_z}{\partial r},$$

where, $\eta^2 = \dfrac{\omega^2}{c^2} - s^2$ and s represents the wave number.

The electric field potentials in regions R_1 and R_3 containing vacuum, are expressed as ϕ_1 and ϕ_3, respectively.

The boundary conditions at the walls $r = h_1, h_2$ and a in region $z < 0$ are manifested as

$$\frac{\partial \phi_1}{\partial r}(h_1, z) = 0, \tag{5.5}$$

$$\frac{\partial \phi_3}{\partial r}(h_2, z) = 0, \tag{5.6}$$

$$\frac{\partial \phi_3}{\partial r}(a, z) = 0. \tag{5.7}$$

Applying the separation of variables technique to the dimensional equation (5.4), the expansion of eigenfunctions is formed as follows:

$$\phi_1(r, z) = e^{ik_0 z} + \sum_{n=0}^{\infty} A_n e^{-is_n^{(I)}(z)} R_{1n}^{(I)}(r), \tag{5.8}$$

$$\phi_3(r,z) = e^{ik_0 z} + \sum_{n=0}^{\infty} C_n e^{-is_n^{(III)}(z)} R_{1n}^{(III)}(r), \tag{5.9}$$

where A_n and C_n exhibit the amplitudes in regions R_1 and R_3. The nth reflected modes in these regions of cylindrical waveguide have wavenumbers expressed as $s_n^{(I)2} = k_0^2 - \eta_n^2;\ s_n^{(III)2} = k_0^2 - \lambda_n^2$.

The Bessel functions, in the regions R_1, are expressed as:

$$R_{1n}^{(I)}(r) = A_0 J_0(\eta_n r),$$

while in region R_3, the Bessel functions take the following form after implementation of condition (5.6),

$$R_{1n}^{(III)}(r) = \frac{C_0}{N_0'(\lambda_n h_2)} \left\{ N_0'(\lambda_n h_2) J_0(\lambda_n r) - J_0'(\lambda_n h_2) N_0(\lambda_n r) \right\}.$$

These functions satisfy the usual orthogonality relations in the following manner:

$$\int_0^a R_{1n}^{I}(r) R_{1m}^{I}(r) r dr = \delta_{mn} E_{1m}^{(I)}, \tag{5.10}$$

$$\int_0^a R_{1n}^{III}(r) R_{1m}^{III}(r) r dr = \delta_{mn} E_{1m}^{(III)}, \tag{5.11}$$

such that

$$E_{1n}^{(I)} = \int_0^a R_{1n}^{I2}(r) r dr,$$

$$E_{1n}^{(III)} = \int_{h_1}^{h_2} R_{1n}^{(III)2}(r) r dr.$$

It is important to note that η_n and $\lambda_n;\ n = 0, 1, 2, \ldots$ are the roots of the equations derived from boundary conditions (5.5) and (5.7),

$$J_0'(\eta_n h_1) = 0, \tag{5.12}$$

$$N_0'(\lambda_n h_2) J_0'(\lambda_n a) - J_0'(\lambda_n h_2) N_0'(\lambda_n a) = 0. \tag{5.13}$$

The equations (5.12) and (5.13) are solved numerically to determine these roots.

5.1.2 Traveling Wave Formulation in Dielectric Medium

The dielectrics are governed by Ampere's law in following manner:

$$\nabla \times \mathbf{B} = -i\omega\epsilon_d\mu_0\mathbf{E}. \tag{5.14}$$

The Helmholtz equation for the EM waves propagating in dielectric medium, can be indicated in longitudinal components as:

$$\left(\nabla^2 + k_1^2\right)\begin{pmatrix} E_z \\ B_z \end{pmatrix} = \begin{pmatrix} 0 \\ 0 \end{pmatrix}. \tag{5.15}$$

The transverse components can be stated as:

$$E_r = \frac{is}{\tau^2}\frac{\partial E_z}{\partial r}, \quad E_\theta = 0,$$

$$B_r = 0, \quad B_\theta = \frac{ik_1^2}{\omega\tau^2}\frac{\partial E_z}{\partial r},$$

such that, $\tau^2 = k_1^2 - s^2$, and $k_1^2 = \omega^2\epsilon_d\mu_0$.

The boundary conditions at the walls in dielectric region are exhibited as:

$$\frac{\partial\phi_2}{\partial r}(h_1, z) = 0, \tag{5.16}$$

$$\frac{\partial\phi_2}{\partial r}(h_2, z) = 0. \tag{5.17}$$

Incorporating the method of separation of variables to dimensional equation (5.15), the eigenfunction expansion takes the form:

$$\phi_2(r, z) = e^{ik_1 z} + \sum_{n=0}^{\infty} B_n e^{-is_n^{(II)}z} R_{1n}^{(II)}(r), \tag{5.18}$$

where B_n denote the amplitudes in regions R_2. The wavenumber of nth mode is given as $s_n^{(II)2} = \omega^2\epsilon_d\mu_0 - \tau_n^2$.

The boundary condition (5.16) yields the Bessel functions, in this region, as

$$R_{1n}^{(II)}(r) = \frac{B_0}{N_0'(\tau_n h_1)} \left\{ N_0'(\tau_n h_1) J_0(\tau_n r) - J_0'(\tau_n h_2) N_0(\tau_n r) \right\},$$

which satisfy the usual orthogonality relations,

$$\int_0^{h_1} R_{1n}^{(II)} R_{1m}^{(II)}(r) r dr = \delta_{mn} E_{1m}^{(II)}, \tag{5.19}$$

such that

$$E_{1n}^{(II)} = \int_0^{h_1} R_{1n}^{(II)2}(r) r dr.$$

The roots of the equation (5.20) derived from boundary condition (5.17) are given as $\tau_n;\ n = 0, 1, 2, \ldots,$

$$N_0'(\tau_n h_1) J_0'(\tau_n h_2) - J_0'(\tau_n h_1) N_0'(\tau_n h_2) = 0. \tag{5.20}$$

5.1.3 Traveling Wave Formulation in Beam and Cold Plasma

The Ampere's law for electron beam is of the form:

$$\nabla \times \mathbf{B} = -\frac{i\omega}{c^2} \overline{\epsilon}_b . \mathbf{E}. \tag{5.21}$$

The Helmholtz equation, in case of propagation in beam, is stated in longitudinal components as:

$$\left\{ \nabla^2 + \left(\frac{\omega^2}{c^2} - k_{nz}^2 \right) \left(1 - \frac{\omega_p^2}{\omega^2} - \frac{\omega_b^2}{\gamma^3 (\omega - k_{nz} v)^2} \right) \right\} \begin{pmatrix} E_z \\ B_z \end{pmatrix} = \begin{pmatrix} 0 \\ 0 \end{pmatrix}.$$

is transformed into the equation

$$\left(\nabla^2 + T_1^2 \right) \begin{pmatrix} E_z \\ B_z \end{pmatrix} = \begin{pmatrix} 0 \\ 0 \end{pmatrix}, \tag{5.22}$$

where $T_1^2 = \left(\frac{\omega^2}{c^2} - k_{nz}^2 \right) \left(1 - \frac{\omega_p^2}{\omega^2} - \frac{\omega_b^2}{\gamma^3 (\omega - k_{nz} v)^2} \right).$

The transverse components can be given as

$$E_r = \frac{is}{\chi^2}\frac{\partial E_z}{\partial r}, \quad E_\theta = 0,$$

$$B_r = 0, \quad B_\theta = \frac{iT_1^2}{\omega\chi^2}\frac{\partial E_z}{\partial r}.$$

Here $\chi^2 = T_1^2 - s^2$.

The Ampere's law for cold plasma is formulated as:

$$\nabla \times \mathbf{B} = -\frac{i\omega}{c^2}\bar{\epsilon}_p.\mathbf{E}. \tag{5.23}$$

For propagation in cold plasma, the Helmholtz equation in terms of longitudinal components, is as follows

$$\left\{\nabla^2 + \left(\frac{\omega^2}{c^2} - k_{nz}^2\right)\left(1 - \frac{\omega_p^2}{\omega^2}\right)\right\}\begin{pmatrix} E_z \\ B_z \end{pmatrix} = \begin{pmatrix} 0 \\ 0 \end{pmatrix},$$

which can be further transformed as

$$\left(\nabla^2 + T_2^2\right)\begin{pmatrix} E_z \\ B_z \end{pmatrix} = \begin{pmatrix} 0 \\ 0 \end{pmatrix}, \tag{5.24}$$

where $T_2^2 = \left(\frac{\omega^2}{c^2} - k_{nz}^2\right)\left(1 - \frac{\omega_p^2}{\omega^2}\right)$.

The transverse components of field can be revealed as

$$E_r = \frac{is}{\gamma^2}\frac{\partial E_z}{\partial r}, \quad E_\theta = 0,$$

$$B_r = 0, \quad B_\theta = \frac{iT_2^2}{\omega\gamma^2}\frac{\partial E_z}{\partial r},$$

where $\gamma^2 = T_2^2 - s^2$.

The boundary conditions at the walls $r = h_1$ and a in this region are mentioned as

$$\phi_4^{(I)}(h_1, z) = \phi_4^{(II)}(h_1, z), \tag{5.25}$$

$$\frac{\partial \phi_4^{(I)}}{\partial r}(h_1, z) = \frac{\partial \phi_4^{(II)}}{\partial r}(h_1, z), \tag{5.26}$$

$$\frac{\partial \phi_4^{(II)}}{\partial r}(a, z) = 0. \tag{5.27}$$

Employing the variable separable technique to equation (5.22) and (5.24), yields the eigenfunction expansion as

$$\phi_4(r,z) = \begin{cases} \phi_4^{(I)}(r,z), & 0 < r < h_1, \\ \phi_4^{(II)}(r,z), & h_1 < r < a, \end{cases} = \begin{cases} \displaystyle\sum_{n=0}^{\infty} D_n e^{is_n z} R_{2n}^{(I)}(r), & 0 < r < h_1, \\ \displaystyle\sum_{n=0}^{\infty} D_n e^{is_n z} R_{2n}^{(II)}(r), & h_1 < r < a, \end{cases} \tag{5.28}$$

where D_n represent the amplitudes in regions R_4 and $s_n\,; n = 0, 1, 2, \ldots$ reveals the wavenumber of nth mode.

The utilization of condition (5.27) reforms the Bessel functions, in this region, as follows

$$R_{2n}^{(I)}(r) = D_0 J_0(\chi_n r),$$

$$R_{2n}^{(II)}(r) = \frac{E_0}{N_0'(\gamma_n a)} \left\{ N_0'(\gamma_n a) J_0(\gamma_n r) - J_0'(\gamma_n a) N_0(\gamma_n r) \right\}.$$

The Bessel functions in $z > 0$, satisfy the derived orthogonality relation

$$\int_0^{h_1} R_{2m}^{(I)}(r) R_{2n}^{(I)}(r) r dr + \int_{h_1}^{a} R_{2m}^{(II)}(r) R_{2n}^{(II)}(r) r dr = \delta_{mn} E_m, \tag{5.29}$$

where

$$E_n = \int_0^{h_1} R_{2n}^{(I)2}(r) r dr + \int_{h_1}^{a} R_{2n}^{(II)2}(r) r dr.$$

Here, χ_n and γ_n, revealed as $\chi_n^2 = T_1^2 - s_n^2$ and $\gamma_n^2 = T_2^2 - s_n^2$; $n = 0, 1, 2, \ldots$ are the roots of the equation derived from boundary condition (5.25) and (5.26),

$$\begin{aligned} &\chi_n \left\{ J_0'(\chi_n h_1) N_0'(\gamma_n a) J_0(\gamma_n h_1) - J_0'(\chi_n h_1) J_0'(\gamma_n a) N_0(\gamma_n h_1) \right\} \\ &= \gamma_n \left\{ N_0'(\gamma_n a) J_0'(\gamma_n h_1) J_0(\chi_n h_1) - J_0'(\gamma_n a) N_0'(\gamma_n h_1) J_0(\chi_n h_1) \right\}. \end{aligned} \tag{5.30}$$

5.1.4 Matching Conditions

As the fields are continuous at the interface $z = 0$, thus the following matching conditions exist:

$$\phi_1(r,0) = \phi_4^{(I)}(r,0), \quad 0 \le r \le h_1, \tag{5.31}$$

$$\phi_2(r,0) = \phi_4^{(II)}(r,0), \quad h_1 \le r \le h_2, \tag{5.32}$$

$$\phi_3(r,0) = \phi_4^{(II)}(r,0), \quad h_2 \le r \le a, \tag{5.33}$$

$$\frac{\partial \phi_1}{\partial z}(r,0) = \frac{\partial \phi_4^{(I)}}{\partial z}(r,0), \quad 0 \le r \le h_1, \tag{5.34}$$

$$\frac{\partial \phi_2}{\partial z}(r,0) = \frac{\partial \phi_4^{(II)}}{\partial z}(r,0), \quad h_1 \le r \le h_2, \tag{5.35}$$

$$\frac{\partial \phi_1}{\partial z}(r,0) = \frac{\partial \phi_4^{(II)}}{\partial z}(r,0), \quad h_2 \le r \le a. \tag{5.36}$$

5.2 MM Solution

From conditions (5.31)-(5.33), we have

$$1 + \sum_{n=0}^{\infty} A_n R_{1n}^{(I)}(r) = \sum_{n=0}^{\infty} D_n R_{2n}^{(I)}(r), \tag{5.37}$$

$$1 + \sum_{n=0}^{\infty} B_n R_{1n}^{(II)}(r) = \sum_{n=0}^{\infty} D_n R_{2n}^{(II)}(r), \tag{5.38}$$

$$1 + \sum_{n=0}^{\infty} C_n R_{1n}^{(III)}(r) = \sum_{n=0}^{\infty} D_n R_{2n}^{(II)}(r). \tag{5.39}$$

Multiplying both the sides of (5.36) by $R_{1m}^{(I)}(r)r$ and integrating from 0 to h_1, we get

$$A_m = -\delta_{m0} + \frac{1}{E_{1m}^{(I)}} \sum_{n=0}^{\infty} D_n P_{mn}, \tag{5.40}$$

where

$$P_{mn} = \int_0^{h_1} R_{1m}^{(I)}(r) R_{2n}^{(I)}(r) r dr.$$

A similar treatment to the equations (5.38) and (5.39) produces

$$B_m = -\delta_{m0} + \frac{1}{E_{1m}^{(II)}} \sum_{n=0}^{\infty} D_n Q_{mn}, \tag{5.41}$$

$$C_m = -\delta_{m0} + \frac{1}{E_{1m}^{(III)}} \sum_{n=0}^{\infty} D_n R_{mn}, \tag{5.42}$$

where

$$Q_{mn} = \int_{h_1}^{h_2} R_{1m}^{(II)}(r) R_{2n}^{(II)}(r) r dr,$$

$$R_{mn} = \int_{h_2}^{a} R_{1m}^{(III)}(r) R_{2n}^{(II)}(r) r dr.$$

Now, incorporating the conditions (5.34)-(5.36) and solving in above mentioned manner, the following equations are formed,

$$k_0 - \sum_{n=0}^{\infty} A_n s_n^{(I)} R_{1n}^{(I)}(r) = \sum_{n=0}^{\infty} D_n s_n R_{2n}^{(I)}(r), \tag{5.43}$$

$$k_1 - \sum_{n=0}^{\infty} B_n s_n^{(II)} R_{1n}^{(II)}(r) = \sum_{n=0}^{\infty} D_n s_n R_{2n}^{(II)}(r), \tag{5.44}$$

$$k_0 - \sum_{n=0}^{\infty} C_n s_n^{(III)} R_{1n}^{(III)}(r) = \sum_{n=0}^{\infty} D_n s_n R_{2n}^{(II)}(r). \tag{5.45}$$

Multiplying (5.43) with $R_{2m}^{(I)}(r)r$ and integrating from 0 to h_1, yields

$$k_0 P_{0m} - \sum_{n=0}^{\infty} A_n s_n^{(I)} P_{nm} = \sum_{n=0}^{\infty} D_n s_n \int_0^{h_1} R_{2m}^{(I)} R_{2n}^{(I)}(r) r dr. \tag{5.46}$$

Similarly, multiplying (5.44) and (5.45) with $R_{2m}^{(II)}(r)r$ and integrating from h_1 to a, the following equation is formed

$$k_1 Q_{0m} + k_0 R_{0m} - \sum_{n=0}^{\infty} B_n s_n^{(II)} Q_{nm} - \sum_{n=0}^{\infty} C_n s_n^{(III)} R_{nm}$$
$$= \sum_{n=0}^{\infty} D_n s_n \int_{h_1}^{a} R_{2m}^{(II)} R_{2n}^{(II)}(r) r dr. \tag{5.47}$$

Adding (5.46) and (5.47) and employing the derived orthogonality relation (5.29), we get

$$D_m = \frac{1}{s_m E_m}\left(k_0 P_{0m} - \sum_{n=0}^{\infty} A_n s_n^{(I)} P_{nm}\right)$$
$$+\frac{1}{s_m E_m}\left(k_1 Q_{0m} + k_0 R_{0m} - \sum_{n=0}^{\infty} B_n s_n^{(II)} Q_{nm} - \sum_{n=0}^{\infty} C_n s_n^{(III)} R_{nm}\right). \quad (5.48)$$

A system of infinite equations is manifested through the equations (5.40)-(5.42) and (5.48) having the unknown coefficients $\{A_n, B_n, C_n, D_n\}$, $n = 0, 1, 2, \ldots$ The system is solved numerically after truncation and the outcomes are displayed and scrutinized in numerical section.

5.3 Energy Flux

The energy flux is a yardstick that determines the convergence of the truncated solution and its accuracy. The Poynting vector is utilized to find energy propagating in different sections of the waveguide, which is stated as [123],

$$Power = \int_R \pi r Re\left\{E_z \left(\frac{\partial E_z}{\partial z}\right)^*\right\} dr, \quad (5.49)$$

where (*) represents complex conjugate.

As we have three different regions in the left duct $z < 0$, the incident and reflected powers in this duct are of the form

$$P_i = P_i^{(I)} + P_i^{(II)} + P_i^{(III)}, \quad (5.50)$$

$$P_r = P_r^{(I)} + P_r^{(II)} + P_r^{(III)}. \quad (5.51)$$

By employing the Poynting vector, the incident (P_i), reflected (P_r) and transmitted (P_t) powers can be ascertained as,

$$P_i = \frac{\pi k_0 h_1^2}{2} + \frac{\pi k_1 (h_2^2 - h_1^2)}{2} + \frac{\pi k_0 (a^2 - h_2^2)}{2}, \quad (5.52)$$

$$P_r = -\pi Re\left(\sum_{n=0}^{\infty}|A_n|^2 s_n^{(I)} E_{1n}^{(I)}\right) - \pi Re\left(\sum_{n=0}^{\infty}|B_n|^2 s_n^{(II)} E_{1n}^{(II)}\right) \\ -\pi Re\left(\sum_{n=0}^{\infty}|C_n|^2 s_n^{(III)} E_{1n}^{(III)}\right), \tag{5.53}$$

$$P_t = \pi Re\left(\sum_{n=0}^{\infty}|D_n|^2 s_n E_n\right). \tag{5.54}$$

The application of law of conservation of power,

$$P_i + P_r = P_t.$$

yields the following form,

$$\frac{\pi k_0 h_1^2}{2} + \frac{\pi k_1(h_2^2 - h_1^2)}{2} + \frac{\pi k_0(a^2 - h_2^2)}{2} \\ -\pi Re\left(\sum_{n=0}^{\infty}|A_n|^2 s_n^{(I)} E_{1n}^{(I)}\right) - \pi Re\left(\sum_{n=0}^{\infty}|B_n|^2 s_n^{(II)} E_{1n}^{(II)}\right) \\ -\pi Re\left(\sum_{n=0}^{\infty}|C_n|^2 s_n^{(III)} E_{1n}^{(III)}\right) = \pi Re\left(\sum_{n=0}^{\infty}|D_n|^2 s_n E_n\right). \tag{5.55}$$

The incident power P_i is scaled to unity to reshape the equation (5.55) as

$$1 = \mathcal{E}_1 + \mathcal{E}_2 + \mathcal{E}_3 + \mathcal{E}_4, \tag{5.56}$$

where

$$\mathcal{E}_1 = \frac{2}{K} Re\left(\sum_{n=0}^{\infty}|A_n|^2 s_n^{(I)} E_{1n}^{(I)}\right),$$

$$\mathcal{E}_2 = \frac{2}{K} Re\left(\sum_{n=0}^{\infty}|B_n|^2 s_n^{(II)} E_{1n}^{(II)}\right),$$

$$\mathcal{E}_3 = \frac{2}{K} Re\left(\sum_{n=0}^{\infty}|C_n|^2 s_n^{(III)} E_{1n}^{(III)}\right),$$

$$\mathcal{E}_4 = \frac{2}{K} Re\left(\sum_{n=0}^{\infty}|D_n|^2 s_n E_n\right),$$

and

$$K = k_0 h_1^2 + k_1(h_2^2 - h_1^2) + k_0(a^2 - h_2^2).$$

5.4 Numerical Results and Discussion

In this section, the outcomes of the numerical solution of the given physical problem are provided. The electric field potentials are illustrated in the figures as follows:

$$\phi_T(r,z) = \begin{cases} \phi_1(r,z), & z<0, \quad 0<r<h_1, \\ \phi_2(r,z), & z<0, \quad h_1<r<h_2, \\ \phi_3(r,z), & z<0, \quad h_2<r<a, \\ \phi_4(r,z), & z>0, \quad 0<r<a. \end{cases}$$

The magnetic fields in the respective regions are displayed in the figures in following manner

$$\phi_{Tz}(r,z) = \begin{cases} \phi_{1z}(r,z), & z<0, \quad 0<r<h_1, \\ \phi_{2z}(r,z), & z<0, \quad h_1<r<h_2, \\ \phi_{3z}(r,z), & z<0, \quad h_2<r<a, \\ \phi_{4z}(r,z), & z>0, \quad 0<r<a, \end{cases}$$

where $\phi jz = \dfrac{\partial \phi_j}{\partial z}$; $j = 1, 2, 3, 4$.

The physical parameters chosen are speed of light, $c = 3 \times 10^8$ m/s and free space permittivity and permeability, mentioned as $\epsilon_0 = 8.85 \times 10^{-12}$ F/m (Farads per meter) and $\mu_0 = 4\pi \times 10^{-7}$ N/A^2 (Newtons per Ampere squared). To attain rigorous numerical results, the duct radii are set as $\overline{h}_1 = 0.2$ cm, $\overline{h}_2 = 0.3$ cm, and $\overline{a} = 0.4$ cm. The beam velocity v is fixed at 0.134×10^8 cm/second while the frequencies are taken as $\omega = 2.5 \times 10^9$ radian/second, $\omega_b = 2 \times 10^9$ radian/second, and $\omega_p = 10^9$ radian/second. The axial wavenumber is considered $k_{1z} = k_0 + 2\pi$. The quantities h_1, h_2 and a reveal the non-dimensional form of radii $\overline{h}_1, \overline{h}_2$ and $\overline{a}$, respectively. The software Mathematica (version 12.1) is used to carry out the simulations.

The MM solution of the system revealed in the equations (5.40)-(5.42) and (5.48) with a truncation parameter N is applied to obtain the numerical results. The solution yields the unknowns $\{A_n, B_n, C_n, D_n\}$; $n = 0, 1, 2, \ldots, 149$ and is utilized to exhibit the accuracy of algebra, distribution of energy and its conservation.

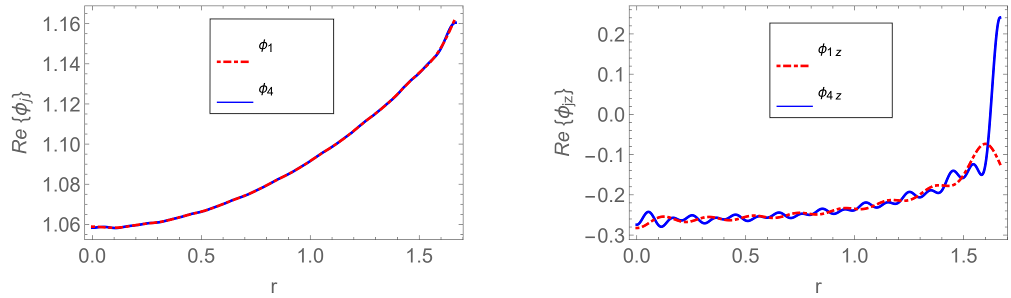

(a) (b)

FIGURE 5.2: Real parts of the electric field and magnetic fields at the interface $z = 0$ and $0 \leq r \leq h_1$.

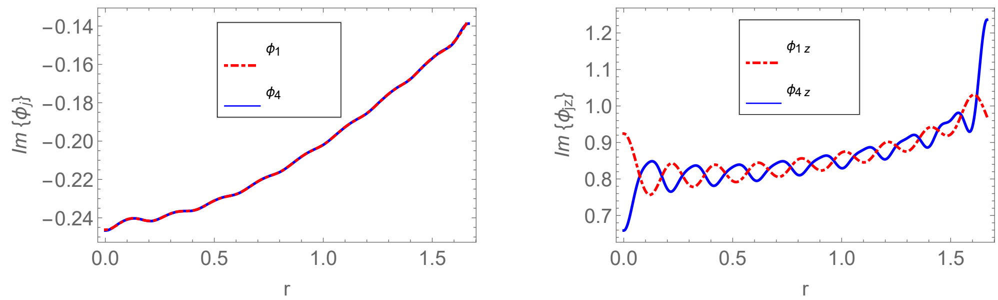

(a) (b)

FIGURE 5.3: Imaginary parts of the electric field and magnetic fields at the interface $z = 0$ and $0 \leq r \leq h_1$.

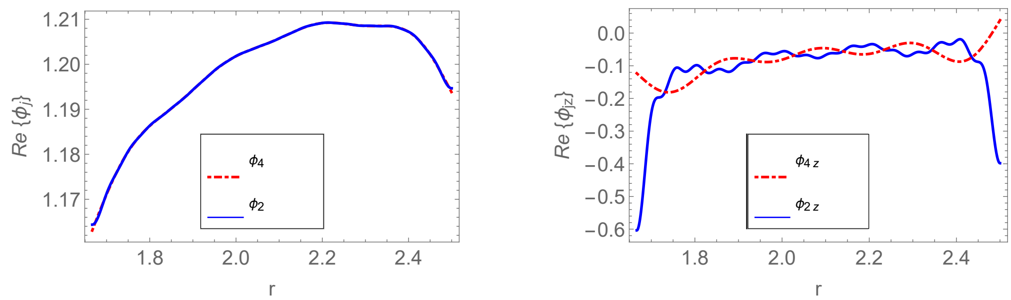

(a) (b)

FIGURE 5.4: Real parts of the electric field and magnetic fields at the interface $z = 0$ and $h_1 \leq r \leq h_2$.

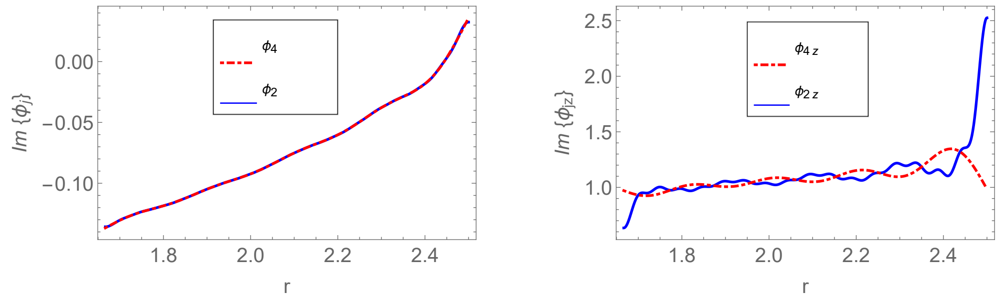

(a) (b)

FIGURE 5.5: Imaginary parts of the electric field and magnetic fields at the interface $z = 0$ and $h_1 \leq r \leq h_2$.

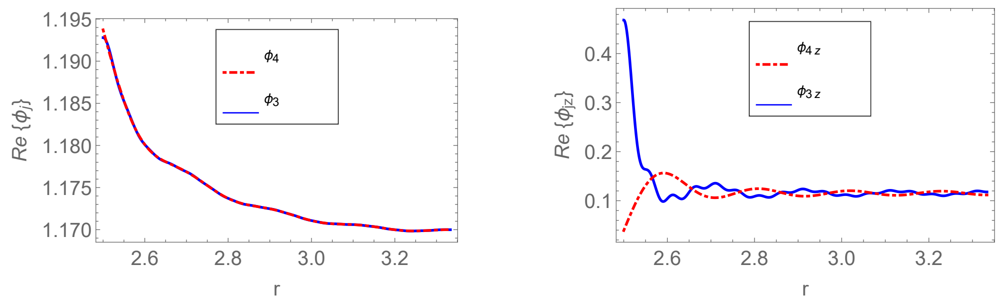

(a) (b)

FIGURE 5.6: Real parts of the electric field and magnetic fields at the interface $z = 0$ and $h_2 \leq r \leq a$.

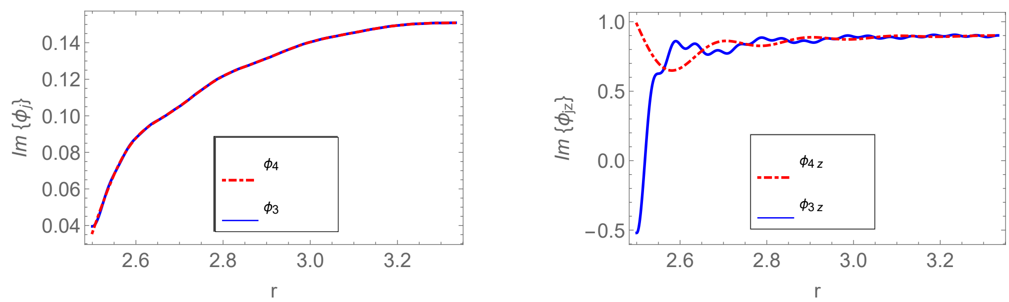

(a) (b)

FIGURE 5.7: Imaginary parts of the electric field and magnetic fields at the interface $z = 0$ and $h_2 \leq r \leq a$.

The figures 5.2 to 5.7 confirm that the matching conditions are validated by the solution at the interface $z = 0$. Across various media, such as vacuum, dielectric, beam, and cold plasma, the magnetic and electric field graphs show a remarkable consistency between their real and imaginary components, indicating excellent agreement along the interface between the different media.

The cogency of law of power conservation in different duct regions is another check on the accuracy of truncated solution. The reflected powers in left duct ($z < 0$) for regions R_1, R_2 and R_3 are represented by $\mathcal{E}_1, \mathcal{E}_2$ and $\mathcal{E}_3$, respectively while the transmitted power in right duct ($z > 0$) is given as $\mathcal{E}_4$. Here, $\mathcal{E}_t$ represents the sum of all powers within the regions of the duct and can be divulged as

$$\mathcal{E}_t = \mathcal{E}_1 + \mathcal{E}_2 + \mathcal{E}_3 + \mathcal{E}_4.$$

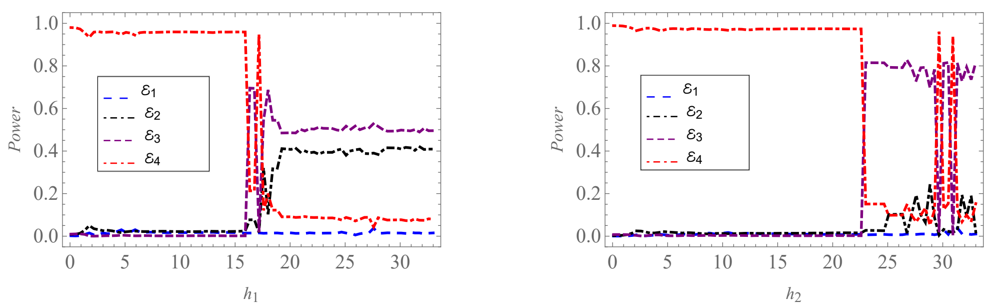

(a) (b)

FIGURE 5.8: Energy flux versus (a) beam radius h_1 and (b) dielectric radius h_2.

The distribution of power versus angular, plasma and beam frequencies as well as plasma and beam radii in different regions of this cylindrical waveguide is analyzed. To study the power behavior in regards to the change in beam and vacuum radius h_1, the other radii are fixed as $h_2 = 2 \times h_1$ (in cm) and $a = 3 \times h_1$ (in cm), while the values of h_1 lie between 0.01 cm $< h_1 <$ 32.5 cm. It is apparent from the graph in (5.8(a)) that the transmission declines very slowly but suddenly drops at $h_1 = 16.33$ cm and reaches almost zero as h_1 grows.

The power is also analyzed against dielectric radius h_2. For this purpose h_2 is assumed between 0.01 cm $< h_2 <$ 32.5 cm, while h_1 and a are set as $h_1 = 0.5 \times h_2$ (in cm) and $a = 2 \times h_2$ (in cm). The figure 5.8(b) reveals that though the transmission seems to have a dominating behavior in the start but after $h_2 = 22.5$

cm, it has a fluctuating behavior which persists with increase in the radius of the dielectric duct.

The power graphs against radius a are plotted in Figure 5.9(a) with the assumptions that the duct radius a takes the values from 0.01 cm $< a <$ 40 cm and $h_1 = 0.5 \times a$ (in cm) and $h_2 = 0.7 \times a$ (in cm). The graph also shows that the reflection is negligible and almost whole power is transmitted through plasma and beam. Notably, in all the power analyses, the plasma, beam and angular frequencies are fixed as $\omega_p = 10^9$ radian/second, $\omega_b = 2 \times 10^9$ radian/second, and $\omega = 2.5 \times 10^9$ radian/second.

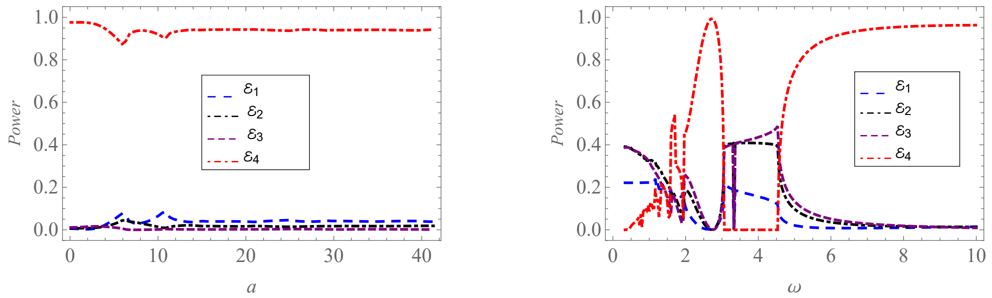

(a) (b)

FIGURE 5.9: Energy flux versus (a) plasma radius a and (b) angular frequency ω.

The impact of angular frequency ω on power propagation is presented in Figure 5.9(b). To investigate this case, the normalized frequency ranges between $0.33 < \omega/c < 10$ while the radii and plasma and beam frequencies are fixed to aforementioned values. It is observed that after some fluctuation all the powers become zero at $\omega/c = 3.33$. The transmission reappears at $\omega/c = 4.57$ while the reflection starts decreasing and reaches almost zero as the angular frequency grows.

To study the effect of increasing plasma frequency, the energy flux is displayed in terms of ω_p/ω in Figure 5.10(a), the range being taken as $0 < \omega_p/\omega < 1.2$. It is obvious from the figure that no transmission takes place after 0.94. As the plasma frequency equals the angular frequency, the reflected and transmitted powers become zero. The transmission remains zero and the whole energy is reflected with increase in ω_p. It complies with the fact that propagation of EM waves does not occur if plasma frequency is greater than wave frequency ω.

The plot of power with respect to ω_b/ω, revealed in Figure 5.10(b), shows that the increase in beam frequency ω_b results in gradual increase in reflection of EM waves. The values vary between $0 < \omega_b/\omega < 1.6$.

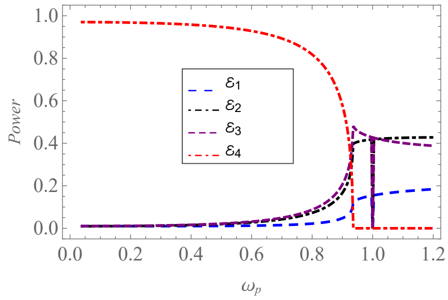

(a)

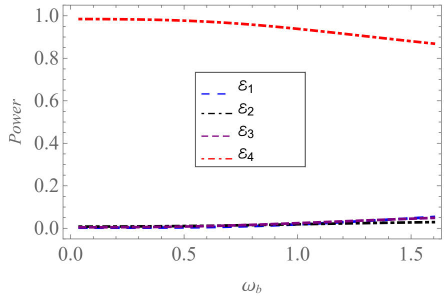

(b)

FIGURE 5.10: Energy flux versus (a) plasma frequency ω_p and (b) beam frequency ω_b.

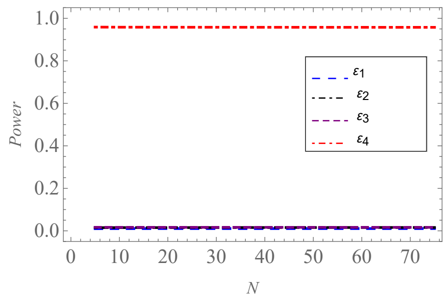

FIGURE 5.11: Power flux plotted against truncated terms N.

TABLE 5.1: Energy conservation versus number of terms N.

Terms (N)	$\mathcal{E}_1$	$\mathcal{E}_2$	$\mathcal{E}_3$	$\mathcal{E}_4$	$\mathcal{E}_t$
10	0.010434	0.015087	0.016378	0.958101	1
20	0.010596	0.015090	0.016345	0.957969	1
30	0.010493	0.015347	0.016324	0.957836	1
40	0.010473	0.015508	0.016304	0.957715	1
50	0.010570	0.015505	0.016294	0.957631	1
60	0.010538	0.015593	0.016285	0.957584	1
70	0.010552	0.015655	0.016275	0.957518	1

TABLE 5.2: Cut-on modes versus duct radius a

Height (a)	R_1	R_2	R_3	R_4
3.33333	1	1	1	1
5.16667	1	1	1	2
5.75000	1	1	2	2
8.75000	1	1	2	3
8.91667	1	1	3	3
12.25000	1	1	3	4
15.75000	1	1	3	5

The conserved power also indicates that the truncated solution is convergent. The accuracy is checked up to six decimal places. The impact of the truncation becomes negligible when $N \geq 50$, which is obvious from Table 5.1 as well as from Figure 5.11. Thus, the given system of infinite equations can easily be considered finite.

Cut-on modes in regard to the plasma and vacuum radius a are computed and presented in Table 5.2. The regions R_1, R_2, R_3 and R_4 are already mentioned in Section 5.1. The increase in radii h_1, h_2 and angular frequency ω does not affect the cut-on modes in any region. There is only one cut-on mode in each region for increasing values of h_1 and ω. The extension of this scattering problem is discussed in the next section.

5.5 TM Wave Scattering in a Cylindrical Waveguide with a Central Chamber containing Beam-Plasma Environment

In the current scattering problem, the beam-plasma region discussed in the preceding section is bounded within the central segment ($|z| < L$) of the waveguide that extends infinitely along the z-axis to discuss the TM wave scattering. Figure 5.12 illustrates the physical setup, providing a visual representation of the arrangement. This investigation conducts a comprehensive analysis of the scattering of EM waves as they propagate in a beam-plasma environment. The study meticulously examines the wave propagation, originating from the region $z < -L$, undergoing interactions with the central region, and ultimately exiting the domain at $z > L$, providing valuable insights into the underlying physical phenomena.

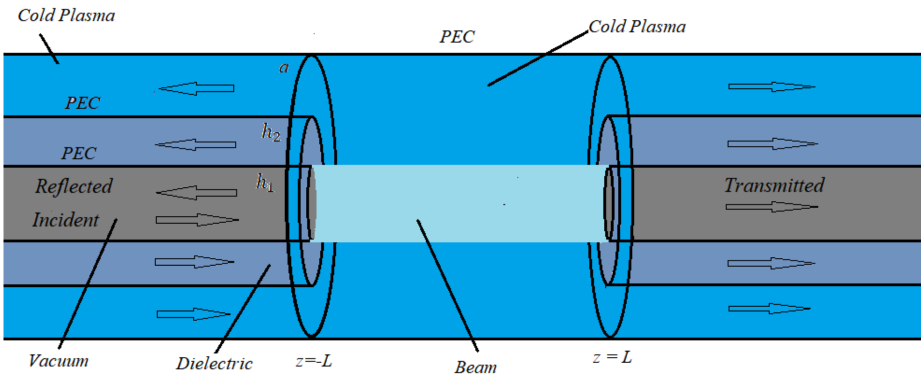

FIGURE 5.12: Propagation of EM waves in a cylindrical waveguide comprising of central chamber containing beam-plasma environment.

5.6 Problem Formulation

The infinite waveguide has PEC boundary at $r = a$. The propagation of a TM incident wave is considered in positive z direction from the left inlet $z < -L$ to the chamber enclosed in the region $|z| < L$. Thus TM wave leaves the chamber at the interface $z = L$ and exits to the right. This incident wave makes a zero angle with the z axis and has unit amplitude. The region $|z| > L$ comprises of vacuum and dielectric, with PEC walls placed at $r = h_1$ and h_2. These mediums are again wrapped in cold magnetized plasma as shown in the figure. The beam in the central chamber is enveloped by cold magnetized plasma at $r = h_1$. The regions $|z| > L, 0 < r < h_1$, denoted by R_1 and R_5 comprise vacuum, while the regions $|z| > L, h_1 < r < h_2$ contain dielectric and are indicated as by R_2 and R_6. Likewise, R_3 and R_7 represent the regions $|z| > L, h_2 < r < a$ comprising plasma. The central region $|z| < L$ decomposed into sub-regions containing beam and plasma in $0 < r < h_1$ and $h_1 < r < a$ is indicated as R_4. The electric fields in these regions R_1 to R_7 are expressed in scalar field potential as $\phi_1, \phi_2, \phi_3, \phi_4, \phi_5, \phi_6$ and ϕ_7, respectively.

$$\phi_1(r,z) = e^{ik_0 z} + \sum_{n=0}^{\infty} A_n e^{-is_n^{(I)}(z)} R_{1n}^{(I)}(r), \tag{5.57}$$

$$\phi_2(r,z) = e^{ik_1 z} + \sum_{n=0}^{\infty} B_n e^{-is_n^{(II)}(z)} R_{1n}^{(II)}(r), \tag{5.58}$$

$$\phi_3(r,z) = e^{ik_2 z} + \sum_{n=0}^{\infty} C_n e^{-is_n^{(III)}(z)} R_{1n}^{(III)}(r), \tag{5.59}$$

$$\phi_4(r,z) = \begin{cases} \phi_4^{(I)}(r,z), & 0 < r < h_1, \\ \phi_4^{(II)}(r,z), & h_1 < r < a, \end{cases}$$

$$= \begin{cases} \displaystyle\sum_{n=0}^{\infty} \left(D_{1n} e^{is_n z} + D_{2n} e^{-is_n z}\right) R_{2n}^{(I)}(r), & 0 < r < h_1, \\ \displaystyle\sum_{n=0}^{\infty} \left(D_{1n} e^{is_n z} + D_{2n} e^{-is_n z}\right) R_{2n}^{(II)}(r), & h_1 < r < a, \end{cases} \tag{5.60}$$

$$\phi_5(r,z) = \sum_{n=0}^{\infty} F_n e^{is_n^{(I)}(z)} R_{1n}^{(I)}(r), \tag{5.61}$$

$$\phi_6(r,z) = \sum_{n=0}^{\infty} G_n e^{is_n^{(II)}(z)} R_{1n}^{(II)}(r), \tag{5.62}$$

$$\phi_7(r,z) = \sum_{n=0}^{\infty} H_n e^{is_n^{(III)}(z)} R_{1n}^{(III)}(r). \tag{5.63}$$

The boundary conditions at the walls $r = h_1, h_2$ and a in regions $|z| > L$ and $|z| < L$ are revealed as

$$\frac{\partial \phi_1}{\partial r}(h_1, z) = \frac{\partial \phi_5}{\partial r}(h_1, z) = 0, \tag{5.64}$$

$$\frac{\partial \phi_2}{\partial r}(h_1, z) = \frac{\partial \phi_6}{\partial r}(h_1, z) = 0, \tag{5.65}$$

$$\frac{\partial \phi_2}{\partial r}(h_2, z) = \frac{\partial \phi_6}{\partial r}(h_2, z) = 0, \tag{5.66}$$

$$\frac{\partial \phi_3}{\partial r}(h_2, z) = \frac{\partial \phi_7}{\partial r}(h_2, z) = 0, \tag{5.67}$$

$$\frac{\partial \phi_3}{\partial r}(a, z) = \frac{\partial \phi_7}{\partial r}(a, z) = 0, \tag{5.68}$$

$$\phi_4^{(I)}(h_1, z) = \phi_4^{(II)}(h_1, z), \tag{5.69}$$

$$\frac{\partial \phi_4^{(I)}}{\partial r}(h_1, z) = \frac{\partial \phi_4^{(II)}}{\partial r}(h_1, z), \tag{5.70}$$

$$\frac{\partial \phi_4^{(II)}}{\partial r}(a, z) = 0, \tag{5.71}$$

where A_n, B_n, C_n, F_n, G_n and H_n exhibit the amplitudes in regions R_1, R_2, R_3, R_5, R_6 and R_7. The nth reflected modes in these regions of cylindrical waveguide have wavenumbers expressed as $s_n^{(I)2} = k_0^2 - \eta_n^2;\ s_n^{(II)2} = k_1^2 - \tau_n^2;\ s_n^{(III)2} = T_2^2 - \lambda_n^2$.

The Bessel functions, in the region R_1 are expressed as,

$$R_{1n}^{(I)}(r) = A_0 J_0(\eta_n r),$$

while in regions R_2 and R_3 the Bessel functions take the following form after implementation of condition (5.65) and (5.67),

$$R_{1n}^{(II)}(r) = \frac{B_0}{N_0'(\tau_n h_1)} \left\{ N_0'(\tau_n h_1) J_0(\tau_n r) - J_0'(\tau_n h_2) N_0(\tau_n r) \right\},$$

$$R_{1n}^{(III)}(r) = \frac{C_0}{N_0'(\lambda_n h_2)} \left\{ N_0'(\lambda_n h_2) J_0(\lambda_n r) - J_0'(\lambda_n h_2) N_0(\lambda_n r) \right\},$$

which satisfy the usual orthogonality relations, such that

$$\int_0^{h_1} R_{1m}^{(I)}(r) R_{1n}^{(I)}(r) r dr = \delta_{mn} E_{1m}^{(I)},$$

$$\int_{h_1}^{h_2} R_{1m}^{(II)}(r) R_{1n}^{(II)}(r) r dr = \delta_{mn} E_{1m}^{(II)},$$

$$\int_{h_2}^{a} R_{1m}^{(III)}(r) R_{1n}^{(III)}(r) r dr = \delta_{mn} E_{1m}^{(III)},$$

where

$$E_{1n}^{(I)} = \int_0^{h_1} R_{1n}^{(I)2}(r) r dr.,$$

$$E_{1n}^{(II)} = \int_{h_1}^{h_2} R_{1n}^{II2}(r) r dr,$$

$$E_{1n}^{(III)} = \int_{h_2}^{a} R_{1n}^{(III)2}(r) r dr.$$

It is important to note that η_n, τ_n and $\lambda_n;\ n = 0, 1, 2, \ldots$ are the roots of the characteristic equations derived from boundary conditions (5.64), (5.66) and (5.68),

$$J_0^{'}(\eta_n h_1) = 0, \tag{5.72}$$

$$N_0^{'}(\tau_n h_1) J_0^{'}(\tau_n h_2) - J_0^{'}(\tau_n h_1) N_0^{'}(\tau_n h_2) = 0, \tag{5.73}$$

$$N_0^{'}(\lambda_n h_2) J_0^{'}(\lambda_n a) - J_0^{'}(\lambda_n h_2) N_0^{'}(\lambda_n a) = 0. \tag{5.74}$$

The Bessel functions and characteristic equations expressed for above-mentioned regions remain valid for the regions R_5, R_6 and R_7.

Invoking condition (5.71), the Bessel functions, in the region $|z| < L$, are expressed as

$$R_{2n}^{(I)}(r) = D_0 J_0(\chi_n r),$$

$$R_{2n}^{(II)}(r) = \frac{E_0}{N_0^{'}(\gamma_n a)} \left\{ N_0^{'}(\gamma_n a) J_0(\gamma_n r) - J_0^{'}(\gamma_n a) N_0(\gamma_n r) \right\},$$

where $\chi_n^2 = T_1^2 - s_n^2$ and $\gamma_n^2 = T_2^2 - s_n^2;\ n = 0, 1, 2, \ldots,$ and s_n reveals the wavenumber of nth mode. The Bessel functions in this region satisfy the derived orthogonality relation

$$\int_0^{h_1} R_{2m}^{(I)}(r) R_{2n}^{(I)}(r) r dr + \int_{h_1}^{a} R_{2m}^{(II)}(r) R_{2n}^{(II)}(r) r dr = \delta_{mn} E_m, \tag{5.75}$$

where

$$E_n = \int_0^{h_1} R_{2n}^{(I)2}(r) r dr + \int_{h_1}^{a} R_{2n}^{(II)2}(r) r dr.$$

Here, χ_n and $\gamma_n;\ n = 0, 1, 2, \ldots$ are the eigenvalues that can be calculated from the characteristic equation, derived from boundary condition (5.69) and (5.70),

$$\begin{aligned} &\chi_n \left\{ J_0^{'}(\chi_n h_1) N_0^{'}(\gamma_n a) J_0(\gamma_n h_1) - J_0^{'}(\chi_n h_1) J_0^{'}(\gamma_n a) N_0(\gamma_n h_1) \right\} \\ &= \gamma_n \left\{ N_0^{'}(\gamma_n a) J_0^{'}(\gamma_n h_1) J_0(\chi_n h_1) - J_0^{'}(\gamma_n a) N_0^{'}(\gamma_n h_1) J_0(\chi_n h_1) \right\}. \end{aligned} \tag{5.76}$$

5.6.1 Matching Conditions

The continuity of electric and magnetic field potentials at the interfaces $z = \pm L$, implies the existence of the following matching conditions:

$$\phi_i(r, \pm L) = \phi_4(r, \pm L), \quad 0 \leq ra, \tag{5.77}$$

$$\frac{\partial \phi_i}{\partial z}(r, \pm L) = \frac{\partial \phi_4}{\partial z}(r, \pm L), \quad 0 \leq r \leq a, \tag{5.78}$$

where $i = 1, 2, 3$ at the interface $z = -L$, while at the interface $z = L$, the variation of i is described as $i = 5, 6, 7$.

5.7 MM Solution

In order to find the unknown coefficients appearing in the field potentials of different regions of this waveguide, we incorporate the matching conditions. Applying conditions (5.77) at the interface $z = -L$, we have

$$1 + \sum_{n=0}^{\infty} A_n R_{1n}^{(I)}(r) = \sum_{n=0}^{\infty} \left(D_{1n} e^{-is_n L} + D_{2n} e^{is_n L}\right) R_{2n}^{(I)}(r), \tag{5.79}$$

$$1 + \sum_{n=0}^{\infty} B_n R_{1n}^{(II)}(r) = \sum_{n=0}^{\infty} \left(D_{1n} e^{-is_n L} + D_{2n} e^{is_n L}\right) R_{2n}^{(II)}(r), \tag{5.80}$$

$$1 + \sum_{n=0}^{\infty} C_n R_{1n}^{(III)}(r) = \sum_{n=0}^{\infty} \left(D_{1n} e^{-is_n L} + D_{2n} e^{is_n L}\right) R_{2n}^{(II)}(r). \tag{5.81}$$

Multiplying both the sides of (5.79) by $R_{1m}^{(I)}(r)r$ and integrating from 0 to h_1, we get

$$A_m = -\delta_{m0} + \frac{1}{E_{1m}^{(I)}} \sum_{n=0}^{\infty} \left(D_{1n} e^{-is_n L} + D_{2n} e^{is_n L}\right) P_{mn}, \tag{5.82}$$

where

$$P_{mn} = \int_0^{h_1} R_{1m}^{(I)}(r) R_{2n}^{(I)}(r) r dr.$$

Solving in a similar manner, the equations (5.80) and (5.81) produce

$$B_m = -\delta_{m0} + \frac{1}{E_{1m}^{(II)}} \sum_{n=0}^{\infty} \left(D_{1n}e^{-is_nL} + D_{2n}e^{is_nL}\right) Q_{mn}, \tag{5.83}$$

$$C_m = -\delta_{m0} + \frac{1}{E_{1m}^{(III)}} \sum_{n=0}^{\infty} \left(D_{1n}e^{-is_nL} + D_{2n}e^{is_nL}\right) R_{mn}, \tag{5.84}$$

where

$$Q_{mn} = \int_{h_1}^{h_2} R_{1m}^{(II)}(r) R_{2n}^{(II)}(r) r dr,$$

$$R_{mn} = \int_{h_2}^{a} R_{1m}^{(III)}(r) R_{2n}^{(II)}(r) r dr.$$

Employing the matching conditions (5.77) at the interface $z = L$, yields

$$\sum_{n=0}^{\infty} F_n R_{1n}^{(I)}(r) = \sum_{n=0}^{\infty} \left(D_{1n}e^{is_nL} + D_{2n}e^{-is_nL}\right) R_{2n}^{(I)}(r), \tag{5.85}$$

$$\sum_{n=0}^{\infty} G_n R_{1n}^{(II)}(r) = \sum_{n=0}^{\infty} \left(D_{1n}e^{is_nL} + D_{2n}e^{-is_nL}\right) R_{2n}^{(II)}(r), \tag{5.86}$$

$$\sum_{n=0}^{\infty} H_n R_{1n}^{(III)}(r) = \sum_{n=0}^{\infty} \left(D_{1n}e^{is_nL} + D_{2n}e^{-is_nL}\right) R_{2n}^{(II)}(r). \tag{5.87}$$

Multiplying both the sides of (5.85) by $R_{1m}^{(I)}(r)r$ and integrating from 0 to h_1, we get

$$F_m = \frac{1}{E_{1m}^{(I)}} \sum_{n=0}^{\infty} \left(D_{1n}e^{is_nL} + D_{2n}e^{-is_nL}\right) P_{mn}. \tag{5.88}$$

Solving the equations (5.86) and (5.87) in a similar way, produces

$$G_m = \frac{1}{E_{1m}^{(II)}} \sum_{n=0}^{\infty} \left(D_{1n}e^{is_nL} + D_{2n}e^{-is_nL}\right) Q_{mn}, \tag{5.89}$$

$$H_m = \frac{1}{E_{1m}^{(III)}} \sum_{n=0}^{\infty} \left(D_{1n}e^{is_nL} + D_{2n}e^{-is_nL}\right) R_{mn}, \tag{5.90}$$

In the above-mentioned manner, by implementing the matching condition (5.78) at the interface $z = -L$, the following equations are derived,

$$k_0 - \sum_{n=0}^{\infty} A_n s_n^{(I)} R_{1n}^{(I)}(r) = \sum_{n=0}^{\infty} \left(D_{1n}e^{-is_nL} - D_{2n}e^{is_nL}\right) s_n R_{2n}^{(I)}(r), \tag{5.91}$$

$$k_1 - \sum_{n=0}^{\infty} B_n s_n^{(II)} R_{1n}^{(II)}(r) = \sum_{n=0}^{\infty} \left(D_{1n} e^{-is_n L} - D_{2n} e^{is_n L}\right) s_n R_{2n}^{(II)}(r), \tag{5.92}$$

$$T_2 - \sum_{n=0}^{\infty} C_n s_n^{(III)} R_{1n}^{(III)}(r) = \sum_{n=0}^{\infty} \left(D_{1n} e^{-is_n L} - D_{2n} e^{is_n L}\right) s_n R_{2n}^{(II)}(r). \tag{5.93}$$

Multiplying (5.91) by $R_{2m}^{(I)}(r)r$ and integrating from 0 to h_1, yields

$$k_0 P_{0m} - \sum_{n=0}^{\infty} A_n s_n^{(I)} P_{nm} = \sum_{n=0}^{\infty} \left(D_{1n} e^{-is_n L} - D_{2n} e^{is_n L}\right) s_n \int_0^{h_1} R_{2m}^{(I)} R_{2n}^{(I)}(r) r dr. \tag{5.94}$$

Similarly, multiplying (5.92) and (5.93) with $R_{2m}^{(II)}(r)r$ and integrating from h_1 to a, the following equation is formed

$$\begin{aligned} &k_1 Q_{0m} + k_2 R_{0m} - \sum_{n=0}^{\infty} B_n s_n^{(II)} Q_{nm} - \sum_{n=0}^{\infty} C_n s_n^{(III)} R_{nm} \\ &= \sum_{n=0}^{\infty} \left(D_{1n} e^{-is_n L} - D_{2n} e^{is_n L}\right) s_n \int_{h_1}^{a} R_{2m}^{(II)} R_{2n}^{(II)}(r) r dr. \end{aligned} \tag{5.95}$$

Adding (5.94) and (5.95) and employing the derived orthogonality relation (5.75), we get

$$\begin{aligned} D_{1m} e^{-is_m L} - D_{2m} e^{is_m L} &= \frac{1}{s_m E_m} \left(k_0 P_{0m} - \sum_{n=0}^{\infty} A_n s_n^{(I)} P_{nm} \right) \\ &+ \frac{1}{s_m E_m} \left(k_1 Q_{0m} + T_2 R_{0m} - \sum_{n=0}^{\infty} B_n s_n^{(II)} Q_{nm} - \sum_{n=0}^{\infty} C_n s_n^{(III)} R_{nm} \right). \end{aligned} \tag{5.96}$$

Solving in a similar way, the deployment of condition (5.78) at the interface $z = L$, the following equations are formed,

$$\sum_{n=0}^{\infty} F_n s_n^{(I)} R_{1n}^{(I)}(r) = \sum_{n=0}^{\infty} \left(D_{1n} e^{is_n L} - D_{2n} e^{-is_n L}\right) s_n R_{2n}^{(I)}(r), \tag{5.97}$$

$$\sum_{n=0}^{\infty} G_n s_n^{(II)} R_{1n}^{(II)}(r) = \sum_{n=0}^{\infty} \left(D_{1n} e^{-is_n L} - D_{2n} e^{is_n L}\right) s_n R_{2n}^{(II)}(r), \tag{5.98}$$

$$\sum_{n=0}^{\infty} H_n s_n^{(III)} R_{1n}^{(III)}(r) = \sum_{n=0}^{\infty} \left(D_{1n} e^{-is_n L} - D_{2n} e^{is_n L}\right) s_n R_{2n}^{(II)}(r). \tag{5.99}$$

Multiplication of (5.97) by $R_{2m}^{(I)}(r)r$ and integrating from 0 to h_1, yields

$$\sum_{n=0}^{\infty} F_n s_n^{(I)} P_{nm} = \sum_{n=0}^{\infty} \left(D_{1n}e^{is_nL} - D_{2n}e^{-is_nL}\right) s_n \int_0^{h_1} R_{2m}^{(I)} R_{2n}^{(I)}(r) r dr. \tag{5.100}$$

Similarly, multiplying (5.98) and (5.99) with $R_{2m}^{(II)}(r)r$ and integrating from h_1 to a, the following equation is formed

$$\begin{aligned} &\sum_{n=0}^{\infty} G_n s_n^{(II)} Q_{nm} + \sum_{n=0}^{\infty} H_n s_n^{(III)} R_{nm} \\ &= \sum_{n=0}^{\infty} \left(D_{1n}e^{is_nL} - D_{2n}e^{-is_nL}\right) s_n \int_{h_1}^{a} R_{2m}^{(II)} R_{2n}^{(II)}(r) r dr. \end{aligned} \tag{5.101}$$

Adding (5.100) to (5.101) and employing the derived orthogonality relation (5.75), we get

$$\begin{aligned} D_{1m}e^{is_mL} - D_{2m}e^{-is_mL} &= \frac{1}{s_m E_m} \sum_{n=0}^{\infty} F_n s_n^{(I)} P_{nm} \\ &+ \frac{1}{s_m E_m} \sum_{n=0}^{\infty} G_n s_n^{(II)} Q_{nm} + \frac{1}{s_m E_m} \sum_{n=0}^{\infty} H_n s_n^{(III)} R_{nm}. \end{aligned} \tag{5.102}$$

Adding (5.82) and (5.88) yields,

$$\Psi_{1m}^{+} = -\delta_{m0} + \frac{2}{E_{1m}^{(I)}} \sum_{n=0}^{\infty} \Phi_n^{+} \cos(s_n L) P_{mn}. \tag{5.103}$$

Similarly adding (5.83) to (5.89) and (5.84) to (5.90), renders

$$\Psi_{2m}^{+} = -\delta_{m0} + \frac{2}{E_{1m}^{(II)}} \sum_{n=0}^{\infty} \Phi_n^{+} \cos(s_n L) Q_{mn}, \tag{5.104}$$

$$\Psi_{3m}^{+} = -\delta_{m0} + \frac{2}{E_{1m}^{(III)}} \sum_{n=0}^{\infty} \Phi_n^{+} \cos(s_n L) R_{mn}. \tag{5.105}$$

Subtracting (5.88) from (5.82), (5.89) from (5.83) and (5.90) from (5.84)

$$\Psi_{1m}^{-} = -\delta_{m0} - \frac{2i}{E_{1m}^{(I)}} \sum_{n=0}^{\infty} \Phi_n^{-} \cos(s_n L) P_{mn}, \tag{5.106}$$

$$\Psi_{2m}^{-} = -\delta_{m0} - \frac{2i}{E_{1m}^{(II)}} \sum_{n=0}^{\infty} \Phi_n^{-} \cos(s_n L) Q_{mn}, \tag{5.107}$$

$$\Psi_{3m}^{-} = -\delta_{m0} - \frac{2i}{E_{1m}^{(III)}} \sum_{n=0}^{\infty} \Phi_n^{-} \cos(s_n L) R_{mn}, \tag{5.108}$$

where $\Psi_{1m}^{\pm} = A_m \pm F_m$, $\Psi_{2m}^{\pm} = B_m \pm G_m$, $\Psi_{3m}^{\pm} = C_m \pm H_m$ and $\Phi_m^{\pm} = D_{1m} \pm D_{2m}$. Subtracting (5.96) from (5.102), we obtain

$$\begin{aligned}\Phi_n^{+} = &-\frac{k_0 P_{0m} + k_1 Q_{0m} + T_2 R_{0m}}{2i s_m E_m \sin(s_m L)} + \frac{1}{2i s_m E_m \sin(s_m L)} \sum_{n=0}^{\infty} \Psi_{1n}^{+} s_n^{(I)} P_{nm} \\ &+ \frac{1}{2i s_m E_m \sin(s_m L)} \sum_{n=0}^{\infty} \Psi_{2n}^{+} s_n^{(II)} Q_{nm} + \frac{1}{2i s_m E_m \sin(s_m L)} \sum_{n=0}^{\infty} \Psi_{3n}^{+} s_n^{(III)} R_{nm}.\end{aligned} \tag{5.109}$$

Adding (5.96) and (5.102), we get

$$\begin{aligned}\Phi_n^{-} = &\frac{k_0 P_{0m} + k_1 Q_{0m} + T_2 R_{0m}}{2 s_m E_m \cos(s_m L)} - \frac{1}{2 s_m E_m \cos(s_m L)} \sum_{n=0}^{\infty} \Psi_{1n}^{-} s_n^{(I)} P_{nm} \\ &- \frac{1}{2 s_m E_m \cos(s_m L)} \sum_{n=0}^{\infty} \Psi_{2n}^{-} s_n^{(II)} Q_{nm} - \frac{1}{2 s_m E_m \cos(s_m L)} \sum_{n=0}^{\infty} \Psi_{3n}^{-} s_n^{(III)} R_{nm}.\end{aligned} \tag{5.110}$$

A system of infinite equations is manifested through the equations (5.103)-(5.110) having the unknown coefficients $\{A_n, B_n, C_n, D_{1n}, D_{2n}, F_n, G_n, H_n\}$, $n = 0, 1, 2, \ldots$ The system is solved numerically after truncation and the outcomes are displayed and scrutinized in numerical section.

5.8 Energy Flux

Using the Poynting vector the energy flux is determined to establish the accuracy and convergence of the MM solution. As we have three different regions in the left duct $z < -L$, the incident and reflected powers in this duct are of the form

$$P_i = P_i^{(I)} + P_i^{(II)} + P_i^{(III)}, \tag{5.111}$$

$$P_r = P_r^{(I)} + P_r^{(II)} + P_r^{(III)}. \tag{5.112}$$

In the right duct $z > L$, the transmitted powers in the three regions can be described as

$$P_t = P_t^{(I)} + P_t^{(II)} + P_t^{(III)}, \tag{5.113}$$

By employing the Poynting vector, the incident (P_i), reflected (P_r) and transmitted (P_t) powers can be ascertained as,

$$P_i = \frac{\pi k_0 h_1^2}{2} + \frac{\pi k_1 (h_2^2 - h_1^2)}{2} + \frac{\pi k_0 (a^2 - h_2^2)}{2}, \tag{5.114}$$

$$\begin{aligned} P_r = -\pi Re\left(\sum_{n=0}^{\infty} |A_n|^2 s_n^{(I)} E_{1n}^{(I)}\right) - \pi Re\left(\sum_{n=0}^{\infty} |B_n|^2 s_n^{(II)} E_{1n}^{(II)}\right) \\ -\pi Re\left(\sum_{n=0}^{\infty} |C_n|^2 s_n^{(III)} E_{1n}^{(III)}\right), \end{aligned} \tag{5.115}$$

$$\begin{aligned} P_t = \pi Re\left(\sum_{n=0}^{\infty} |F_n|^2 s_n^{(I)} E_{1n}^{(I)}\right) + \pi Re\left(\sum_{n=0}^{\infty} |G_n|^2 s_n^{(II)} E_{1n}^{(II)}\right) \\ +\pi Re\left(\sum_{n=0}^{\infty} |H_n|^2 s_n^{(III)} E_{1n}^{(III)}\right), \end{aligned} \tag{5.116}$$

The application of law of conservation of power,

$$P_i + P_r = P_t.$$

yields the following form,

$$\begin{aligned} \frac{\pi k_0 h_1^2}{2} + \frac{\pi k_1 (h_2^2 - h_1^2)}{2} + \frac{\pi k_0 (a^2 - h_2^2)}{2} - \pi Re\left(\sum_{n=0}^{\infty} |A_n|^2 s_n^{(I)} E_{1n}^{(I)}\right) \\ -\pi Re\left(\sum_{n=0}^{\infty} |B_n|^2 s_n^{(II)} E_{1n}^{(II)}\right) - \pi Re\left(\sum_{n=0}^{\infty} |C_n|^2 s_n^{(III)} E_{1n}^{(III)}\right) \\ = \pi Re\left(\sum_{n=0}^{\infty} |F_n|^2 s_n^{I} E_{1n}^{(I)}\right) + \pi Re\left(\sum_{n=0}^{\infty} |G_n|^2 s_n^{(II)} E_{1n}^{(II)}\right) \\ +\pi Re\left(\sum_{n=0}^{\infty} |H_n|^2 s_n^{(III)} E_{1n}^{(III)}\right). \end{aligned} \tag{5.117}$$

To reshape the equation (5.117), the incident power P_i is normalized to a value of 1, such that

$$1 = \mathcal{E}_1 + \mathcal{E}_2 + \mathcal{E}_3 + \mathcal{E}_4 + \mathcal{E}_5 + \mathcal{E}_6, \tag{5.118}$$

where

$$\mathcal{E}_1 = \frac{2}{K} Re\left(\sum_{n=0}^{\infty} |A_n|^2 s_n^{(I)} E_{1n}^{(I)}\right),$$

$$\mathcal{E}_2 = \frac{2}{K} Re\left(\sum_{n=0}^{\infty} |B_n|^2 s_n^{(II)} E_{1n}^{(II)}\right),$$

$$\mathcal{E}_3 = \frac{2}{K} Re\left(\sum_{n=0}^{\infty} |C_n|^2 s_n^{(III)} E_{1n}^{(III)}\right),$$

$$\mathcal{E}_4 = \frac{2}{K} Re\left(\sum_{n=0}^{\infty} |F_n|^2 s_n^{(I)} E_{1n}^{(I)}\right),$$

$$\mathcal{E}_5 = \frac{2}{K} Re\left(\sum_{n=0}^{\infty} |G_n|^2 s_n^{(II)} E_{1n}^{(II)}\right),$$

$$\mathcal{E}_6 = \frac{2}{K} Re\left(\sum_{n=0}^{\infty} |H_n|^2 s_n^{(III)} E_{1n}^{(III)}\right),$$

and

$$K = k_0 h_1^2 + k_1(h_2^2 - h_1^2) + k_0(a^2 - h_2^2).$$

5.9 Numerical Discussion

In this section, the results of the numerical solution of the specified physical problem are presented. The electric field potentials are depicted in the figures as below:

$$\phi_T(r,z) = \begin{cases} \phi_1(r,z), & z < -L, & 0 < r < h_1, \\ \phi_2(r,z), & z < -L, & h_1 < r < h_2, \\ \phi_3(r,z), & z < -L, & h_2 < r < a, \\ \phi_4(r,z), & -L < z < L, & 0 < r < a, \\ \phi_5(r,z), & z > L, & 0 < r < h_1, \\ \phi_6(r,z), & z > L, & h_1 < r < h_2, \\ \phi_7(r,z), & z > L, & h_2 < r < a. \end{cases}$$

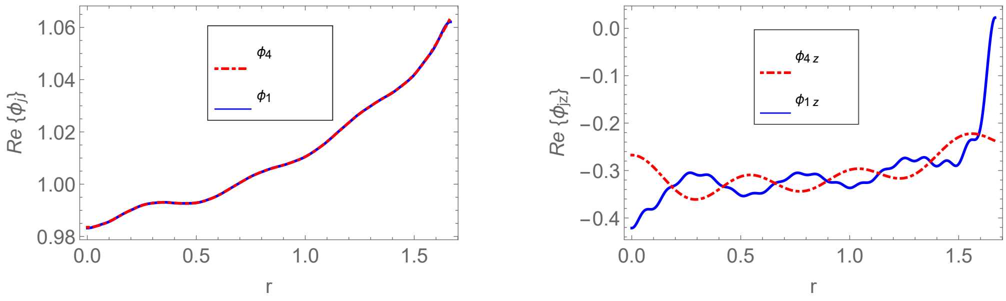

(a) (b)

FIGURE 5.13: Real parts of the electric field and magnetic fields at the interface $z = -L$ and $0 \leq r \leq h_1$.

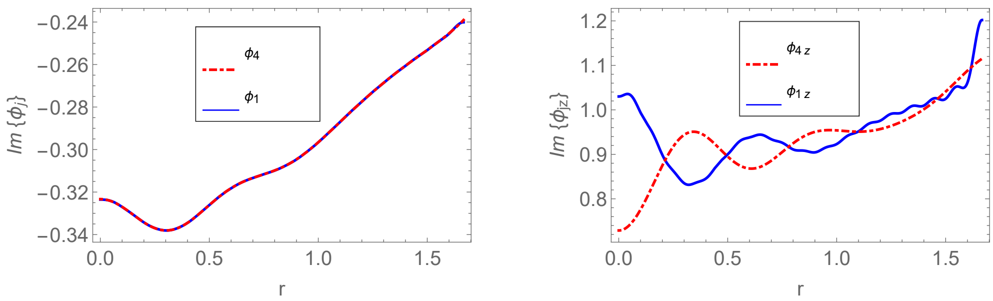

(a) (b)

FIGURE 5.14: Imaginary parts of the electric field and magnetic fields at the interface $z = -L$ and $0 \leq r \leq h_1$.

The figures display the magnetic fields in their respective regions as follows:

$$\phi_{Tz}(r,z) = \begin{cases} \phi_{1z}(r,z), & z < -L, \qquad 0 < r < h_1, \\ \phi_{2z}(r,z), & z < -L, \qquad h_1 < r < h_2, \\ \phi_{3z}(r,z), & z < -L, \qquad h_2 < r < a, \\ \phi_{4z}(r,z), & -L < z < L, \quad 0 < r < a, \\ \phi_{5z}(r,z), & z > L, \qquad 0 < r < h_1, \\ \phi_{6z}(r,z), & z > L, \qquad h_1 < r < h_2, \\ \phi_{7z}(r,z), & z > L, \qquad h_2 < r < a, \end{cases}$$

where $\phi jz = \dfrac{\partial \phi_j}{\partial z}$; $j = 1, 2, 3, 4, 5, 6, 7$.

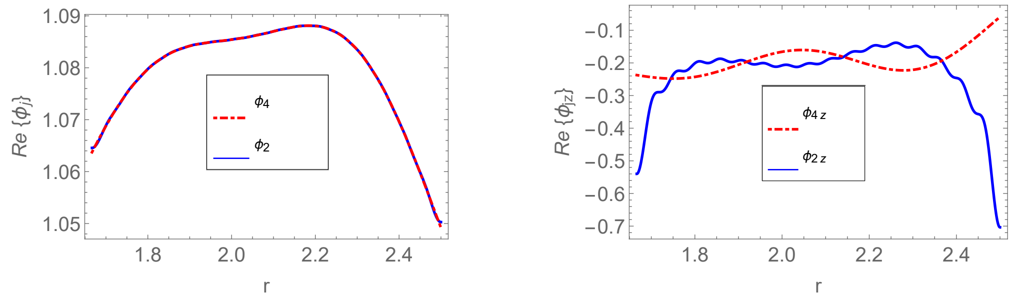

(a) (b)

FIGURE 5.15: Real parts of the electric field and magnetic fields at the interface $z = -L$ and $h_1 \leq r \leq h_2$.

The physical parameters, values of duct radii, axial wavenumber and the frequencies are same as were considered in Section 5.4. The chamber length L is set as $2 \times L = 2 \times 0.25$ cm. The quantities h_1, h_2 and a are the non-dimensional analogues of radii $\overline{h}_1, \overline{h}_2$ and $\overline{a}$, respectively. The truncated system of equations is solved and the simulations are executed using the software Mathematica (version 12.1).

The utilization of the MM technique has provided the solution for the system described in the equations (5.103)-(5.110) with a truncation parameter N. Thus the unknown coefficients $\{A_n, B_n, C_n, D_{1n}, D_{2n}, F_n, G_n, H_n\}$; $n = 0, 1, 2, \ldots, 99$ are determined. The solution is further employed to verify the precision of algebra as well as conservation and distribution of power.

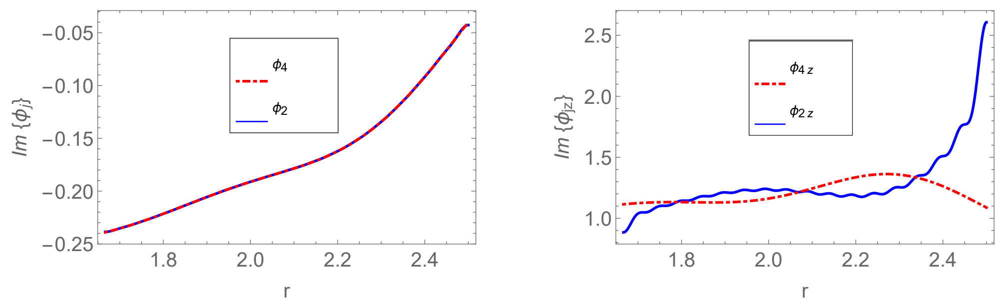

(a) (b)

FIGURE 5.16: Imaginary parts of the electric field and magnetic fields at the interface $z = -L$ and $h_1 \leq r \leq h_2$.

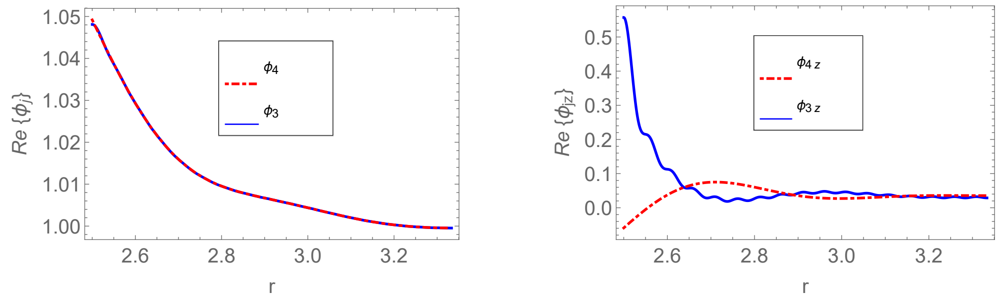

(a) (b)

FIGURE 5.17: Real parts of the electric field and magnetic fields at the interface $z = -L$ and $h_2 \leq r \leq a$.

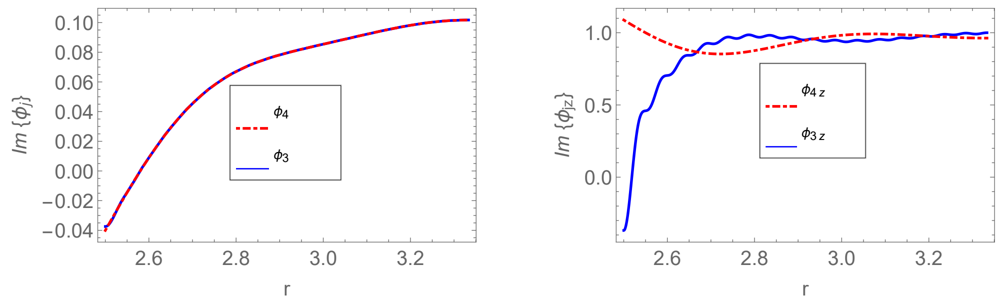

(a) (b)

FIGURE 5.18: Imaginary parts of the electric field and magnetic fields at the interface $z = -L$ and $h_2 \leq r \leq a$.

The accuracy of truncated solution is checked through reconstruction of the matching conditions at the two interfaces $z = \pm L$ and are displayed in figures 5.13-5.24. The real and imaginary parts of electric and magnetic field potentials completely coincide at the two interfaces in all mediums as is obvious from the figures.

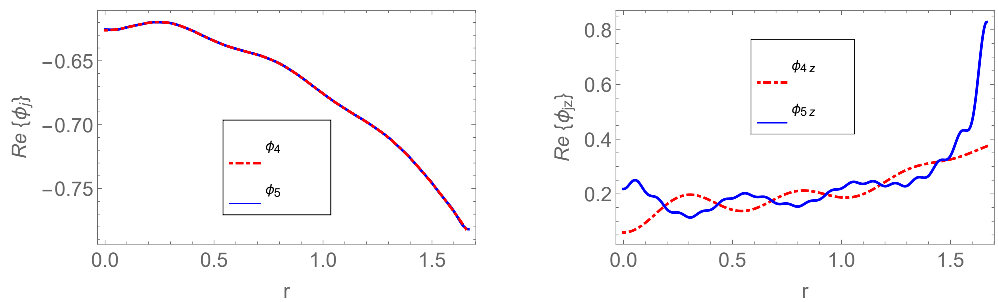

(a) (b)

FIGURE 5.19: Real parts of the electric field and magnetic fields at the interface $z = L$ and $0 \leq r \leq h_1$.

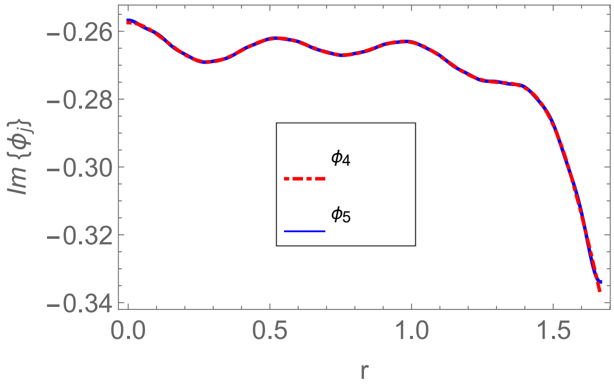

(a)

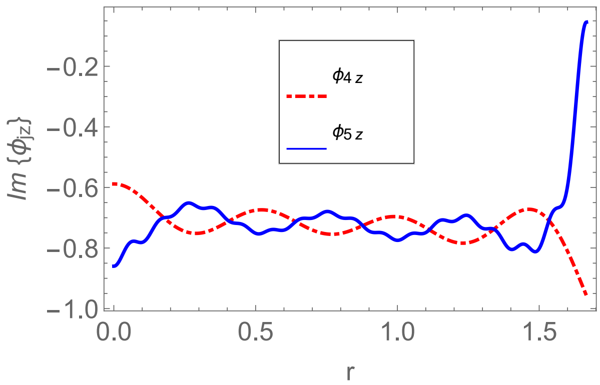

(b)

FIGURE 5.20: Imaginary parts of the electric field and magnetic fields at the interface $z = L$ and $0 \leq r \leq h_1$.

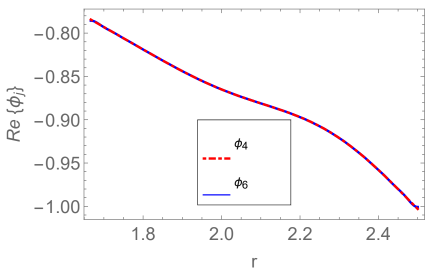

(a)

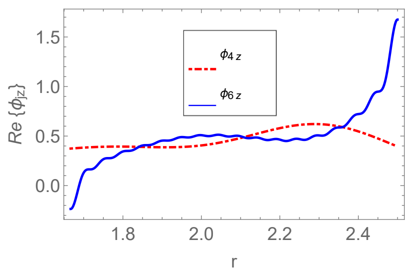

(b)

FIGURE 5.21: Real parts of the electric field and magnetic fields at the interface $z = L$ and $h_1 \leq r \leq h_2$.

The validity of the law of conservation of energy in various duct regions serves as another means to verify the accuracy of a truncated solution. The reflected powers in left duct ($z < -L$) for regions R_1, R_2 and R_3 are revealed as $\mathcal{E}_1, \mathcal{E}_2$ and

$\mathcal{E}_3$, respectively while $\mathcal{E}_4, \mathcal{E}_5$ and $\mathcal{E}_6$ exhibit the transmitted powers in the right duct $(z > L)$. The sum of all powers $\mathcal{E}_t$ is stated as:

$$\mathcal{E}_t = \mathcal{E}_1 + \mathcal{E}_2 + \mathcal{E}_3 + \mathcal{E}_4 + \mathcal{E}_5 + \mathcal{E}_6.$$

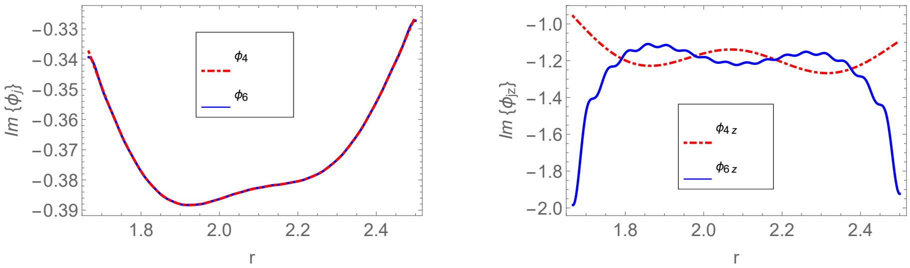

(a) (b)

FIGURE 5.22: Imaginary parts of the electric field and magnetic fields at the interface $z = L$ and $h_1 \leq r \leq h_2$.

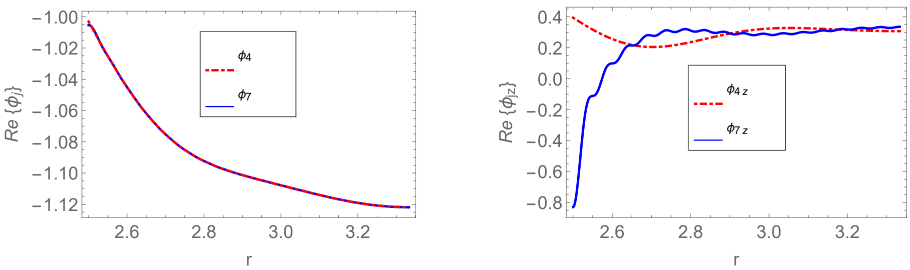

(a) (b)

FIGURE 5.23: Real parts of the electric field and magnetic fields at the interface $z = L$ and $h_2 \leq r \leq a$.

The influence of increasing angular frequency, plasma radius and plasma frequency on power propagation is depicted in figures 5.25 and 5.26. The figure 5.25 presents the effect of angular frequency ω on propagation. In order to study this impact, the distribution of power versus ω/c is considered. The range of angular frequency is between $0.33 < \omega/c < 10$. The graph illustrates the concept of increasing angular frequency ω leading to predominant transmission and minimal reflection.

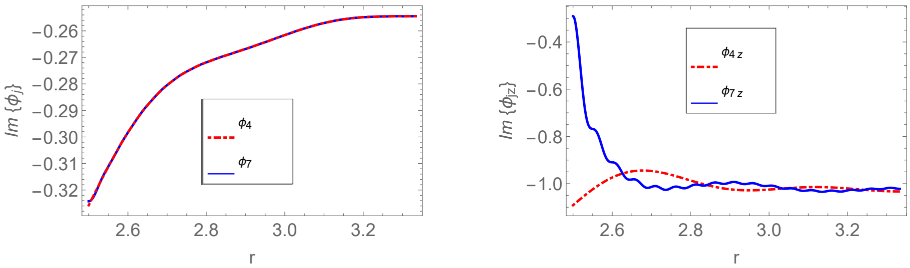

(a) (b)

FIGURE 5.24: Imaginary parts of the electric field and magnetic fields at the interface $z = L$ and $h_2 \leq r \leq a$.

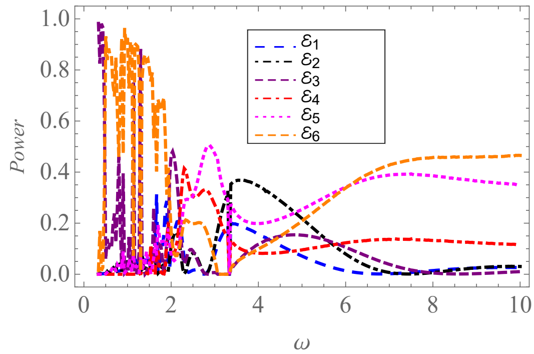

FIGURE 5.25: Power flux versus angular frequency ω.

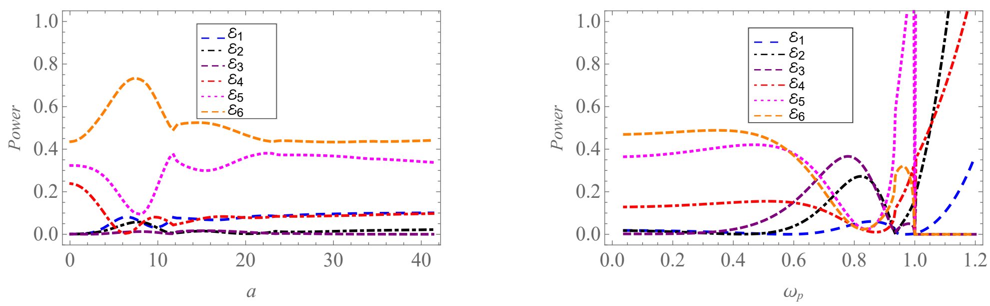

(a) (b)

FIGURE 5.26: Energy flux versus (a) plasma radius a, and (b) plasma frequency ω_p.

The impact of increasing plasma radius a and plasma frequency ω_p/ω on power flux is exhibited in figures 5.26(a) and 5.26(b), respectively. The plasma radius a ranges between 0.01 cm $< a <$ 40 cm, while the other two radii are fixed as $h_1 = 0.5 \times a$ (in cm) and $h_2 = 0.7 \times a$ (in cm). Figure 5.26(a) reveals that transmission in cold plasma region is dominant as a increases. Meanwhile, the plot of power against plasma frequency in Figure 5.26(b) shows that no transmission and reflection takes place in cold plasma region when $\omega_p/\omega > 1$. The values of plasma frequency are set as $0 < \omega_p/\omega < 1.2$.

Chapter 6

Conclusion and Future Work

This dissertation explores the scattering analysis of EM waves in various plasma-filled structures, employing the MM technique to solve the governing boundary value problems. The results demonstrate a close agreement in the curves of EM field potentials and scattering of powers.

In the introductory chapter (Chapter 1), the context of this study is established, including its relevance to current research and an overview of related literature. The objectives of this dissertation are outlined, focusing on physical problem solutions. The fundamental concepts required for understanding scattering analysis of EM waves in diverse waveguide structures, as well as the derivation of wave equations and different boundary conditions for various waveguide models, are discussed in Chapter 2. Additionally, standard and generalized orthogonality relations are explored based on physical models within this chapter.

Chapter 3 of the study focuses on the impact of cold plasma on the transmission of EM waves within rectangular waveguides. The findings suggest a lossless configuration suitable for application in plasma waveguide amplifiers, comprising two partially enclosed waveguides. The first segment consisted of a partially bounded waveguide featuring a metallic wall with dielectric material. The second segment involved a partially bounded waveguide incorporating a layer of cold plasma situated between dielectric layers. The MM solution was explored to analyze the behavior of transmission and reflection coefficients in relation to the initial three incident modes, with a focus on both transparency and non-transparency regions. This analysis is crucial in understanding how EM waves interact with different mediums and interfaces. In both frequency regimes, the magnitudes of reflection coefficients for modes other than the dominant mode are negligible, indicating their insignificant contribution to the overall reflection. The reflection coefficient magnitude remains constant in both the transparency and non-transparency frequency regions for the dominant mode. The transmission coefficient of the dominant mode in the non-transparency frequency region exhibits a non-zero magnitude, and attains a maximum value in the transparency region. The analysis also includes the examination of energy flux in various duct sections versus waveguide dimensions, across both transparency and non-transparency frequency regions. In the non-transparency region, it is noted that energy propagation in cold plasma is not possible, regardless of changes to the waveguide dimensions. However, in the transparency region, energy propagation increases with increment in plasma width. One significant observation from the analysis is that in the non-transparency regime, altering the waveguide dimensions has no effect on energy propagation in cold plasma regions, where energy propagation remains impossible. This suggests a unique behavior of energy transmission in this specific condition. Moreover, it was noted that as the width of plasma increases, there is a corresponding increase in the energy flux. The coefficients are structured in a manner to ensure that the law of conservation of power is upheld. The comprehensive approach of determining the conservation of energy both mathematically and intrinsically, utilizing the Poynting vector, resulted in the verification of the accuracy of the solution.

In Chapter 3, an in-depth analysis was also performed on the behavior of EM waves in a rectangular waveguide with a grooved structure, featuring a central cold plasma slab. The study investigated a structure with potential applications in plasma waveguide resonators and gas chromatography equipment, with versatile uses in various designs, such as plasma antennas, halfway plates and frequency selective surfaces. A groove is enveloped between two semi-bounded waveguides in this arrangement. The semi-bounded regions in the left and right sections of the waveguide contain dielectric and are bounded by metallic walls. The bounded metallic groove located in the central section consists of a cold plasma slab, configured in two ways: (I) sandwiched between metallic strips, and (II) sandwiched between dielectric layers, without metallic strips. The systems of infinite algebraic equations were extracted from the boundary value problems associated with the reflection and transmission for both cases. The numerical outcomes acquired for case (I) are comparable with the results presented by Najari et al. [106] in their article. Using the MM solution, an investigation was conducted to analyze the transmission and reflection coefficients of the initial three incident modes in two regimes, i. e., transparency and non-transparency, to understand their behavior in different scenarios. It is also concluded that first mode of both reflected and transmitted modes remains dominant in both frequency regimes. In the non-transparency regime, the reflection and transmission coefficients for the modes other than the dominant are significantly small, making their contribution negligible, while the dominant mode plays a significant role. The proposed solution is validated by the conservation of power, ensuring convergence and accuracy. The analysis reveals that the energy propagates through different duct sections with increasing waveguide heights, in both transparency and non-transparency regimes, with minimal reflection, confirming the efficacy of the solution.

In Chapter 4, the analysis of EM wave scattering in a PEC cylindrical waveguide comprising a central chamber, having a center filled with cold plasma, has been carried out rigorously. The study was pivoted around a structure with prospects of its potential use as a plasma waveguide amplifier. The physical setup consists of a chamber sandwiched between two semi-bounded waveguides with a PEC wall and having vacuum, in an infinite cylindrical waveguide. The central section is a bounded chamber comprising cold plasma, enclosed within vacuum. This vacuum is again wrapped within a dielectric environment through PEC walls. The boundary value problem corresponding to reflection and transmission was formed into system of infinite algebraic equations. The verification of the matching conditions was also performed. It was concluded that the electric and magnetic fields perfectly coincide at the two interfaces. The power flux was also probed, for both transparency and non-transparency regimes, in different duct regions. It was apparent through computations that energy propagates through this waveguide with some reflection phenomenon for both frequency regimes. The change in plasma radius or chamber length does not have a significant effect on transmission. In transparency regime, a single cut-on or propagating mode is consistently observed across all three regions within the chamber, regardless of changes in plasma radius or angular frequency. In the non-transparency regime, no cut-on modes appear in the cold plasma region, however, both vacuum and dielectric regions still exhibit one propagating mode each.

The structure and settings of this cylindrical waveguide are comparable with the work presented by Saviz [124], though the focus of numerical discussion differs.

In Chapter 5, a detailed analysis on the propagation of EM waves, within a PEC cylindrical waveguide having an electron beam encompassed by cold plasma, has been carried out. Plasma conductivity has a substantial influence on EM propagation in the proposed design. This structure has its utility as high power microwave source and in cavity resonators. The physical configuration includes a beam embedded in cold collisionless plasma within an unbounded waveguide. The waveguide is composed of semi-bounded left and right duct regions and has a PEC wall. The left section is configured as vacuum-dielectric-vacuum, bounded by PEC walls. The corresponding boundary value problem was formed into infinite system of linear algebraic equations. The matching conditions were reconstructed in order to confirm the accuracy of truncated solution. The real and imaginary components of the EM fields were observed to match perfectly at the interface. The energy distribution within this waveguide was also explored. It was noticed through computations and plots that the increase in beam radius in the right duct leads to decrease in transmission and increase in dielectric radius results in fluctuation in powers. However, power seems to be transmitted completely through beam and plasma as the duct radius increases. It was also noticed that the angular frequency larger than the plasma and beam frequencies results in total transmission of the EM waves within the waveguide. The increase in beam and plasma frequencies, with respect to angular frequency, creates a negative impact on transmission of EM waves. Cut-on modes were also calculated for all regions of this waveguide. The number of cut-on modes in right duct increased with increase in the cold plasma radius. Conversely, the increase in beam radius and angular frequency did not affect the number of cut-on modes and only one cut-on mode persists in each region.

The arrangement inside the right duct of this cylindrical waveguide is analogous to the design presented by Hong-Quan and Pu-Kun [67] in their paper, however the numerical results and discussion are different.

The last problem discussed, in chapter 5, is the extension of the beam-plasma problem discussed earlier. The physical configuration depicts the beam-plasma region bounded by PEC walls within the central segment of a cylindrical waveguide that extends infinitely along the z-axis to discuss the TM wave scattering. The vacuum-dielectric-plasma regions in the semi-bounded left and right ducts are separated by PEC walls. The system of infinite algebraic equations was derived from the boundary value problem associated with reflection and transmission. The matching conditions were reconstructed to validate the accuracy of the truncated solution. It was determined that the electric and magnetic fields align perfectly at the two interfaces. The graph of power flux versus angular frequency shows an increase in transmission as the angular frequency rises. The effect of increasing cold plasma radius and plasma frequency on power was also ascertained. The transmission of power in cold plasma region was dominant with increase in plasma radius, while energy transmission in this region disappeared as plasma frequency exceeded angular frequency.

Future Directions

- The extension of the physical problems explored in this dissertation can be expanded to investigate: a structure featuring periodic grooves with plasma slabs sandwiched between dielectric layers and, a symmetric rectangular waveguide with multiple plasma slabs embedded between metallic plates or dielectric layers within the groove. These configurations offer a promising area of study, with potential for extensive analysis and exploration.
- This study has prospects to be scaled up to a circular waveguide of infinite length, featuring a plasma beam at the center of a chamber. The chamber

would be enclosed by semi-bounded waveguides filled with dielectric material, and the plasma beam could be sandwiched in layers of cold unmagnetized plasma and dielectric, without PEC walls.

- The research has also the potential to be expanded by exploring an infinite cylindrical structure where a chamber, containing plasma beam, is bounded by cold plasma in the left and right ducts, with the cold plasma layers separated from the beam within the chamber by PEC walls.

- The EM scattering phenomenon analyzed in this dissertation has broad applicability to various plasma-filled structures, including a cylindrical waveguide with a beam embedded in plasma in left and right ducts, and a central chamber with a vacuum-dielectric-vacuum configuration. The design offers opportunities for further discussion and analysis.

Bibliography

[1] Z. Chen and R. E. Wirz, *Cold atmospheric plasma (CAP) technology and applications*. Morgan & Claypool Publishers, 2021.

[2] H. Poeverlein, “Propagation of electromagnetic waves in a plasma with strong magnetic field,” *The Physics of Fluids*, vol. 4, no. 4, pp. 397–405, 1961.

[3] A. Privat-Maldonado, C. Bengtson, J. Razzokov, E. Smits, and A. Bogaerts, “Modifying the tumour microenvironment: Challenges and future perspectives for anticancer plasma treatments,” *Cancers*, vol. 11, no. 12, p. 1920, 2019.

[4] G. R. Warne, P. M. Williams, H. Q. Pho, N. N. Tran, V. Hessel, and I. D. Fisk, “Impact of cold plasma on the biomolecules and organoleptic properties of foods: A review,” *Journal of Food Science*, vol. 86, no. 9, pp. 3762–3777, 2021.

[5] L. Di, J. Zhang, X. Zhang, H. Wang, H. Li, Y. Li, and D. Bu, “Cold plasma treatment of catalytic materials: a review,” *Journal of Physics D: Applied Physics*, vol. 54, no. 33, p. 333001, 2021.

[6] K. Lotov, “Laser wakefield acceleration in narrow plasma-filled channels,” *Laser and Particle Beams*, vol. 19, no. 2, pp. 219–222, 2001.

[7] A. P. Misra and A. Holkundkar, “Wakefield generation and particle acceleration in high-intensity laser plasma and beam-plasma interactions,” 2023.

[8] A. Refaie Ali, N. Eldabe, A. A. El Naby, M. Ibrahim, and O. Abo-Seida, “Em wave propagation within plasma-filled rectangular waveguide using fractional space and lfd,” *The European Physical Journal Special Topics*, vol. 232, no. 14, pp. 2531–2537, 2023.

[9] M. Jasiński, M. Dors, and J. Mizeraczyk, "Production of hydrogen via methane reforming using atmospheric pressure microwave plasma," *Journal of Power Sources*, vol. 181, no. 1, pp. 41–45, 2008.

[10] D. Czylkowski, B. Hrycak, M. Jasiński, M. Dors, and J. Mizeraczyk, "Microwave plasma-based method of hydrogen production via combined steam reforming of methane," *Energy*, vol. 113, pp. 653–661, 2016.

[11] P. Viegas, E. Slikboer, Z. Bonaventura, O. Guaitella, A. Sobota, and A. Bourdon, "Physics of plasma jets and interaction with surfaces: review on modelling and experiments," *Plasma Sources Science and Technology*, vol. 31, no. 5, p. 053001, 2022.

[12] H. Nowakowska, M. Jasiński, and J. Mizeraczyk, "Electromagnetic field distributions in waveguide-based axial-type microwave plasma source," *The European Physical Journal D*, vol. 54, no. 2, pp. 511–518, 2009.

[13] M. C. Downer, R. Zgadzaj, A. Debus, U. Schramm, and M. Kaluza, "Diagnostics for plasma-based electron accelerators," *Reviews of Modern Physics*, vol. 90, no. 3, p. 035002, 2018.

[14] E. Bustamante, M. Calderon, J. Senties, and E. Anabitarte, "Absorption of high-frequency electromagnetic waves by a transversely magnetised cold plasma waveguide," *Journal of Physics D: Applied Physics*, vol. 22, no. 3, p. 408, 1989.

[15] I. Alexeff, T. Anderson, E. Farshi, N. Karnam, and N. R. Pulasani, "Recent results for plasma antennas," *Physics of Plasmas*, vol. 15, no. 5, 2008.

[16] E. Garcia, J. A. Murphy, E. De Lera, and D. Segovia, "Analysis of the left-handed corrugated circular waveguide," *IET microwaves, antennas & propagation*, vol. 2, no. 7, pp. 659–667, 2008.

[17] J. P. Leite Neto and J. J. Barroso, "The sinusoid as the longitudinal profile in backward-wave oscillators of large cross sectional area," *Brazilian journal of physics*, vol. 34, pp. 1577–1582, 2004.

[18] S.-H. Min, H. Jung, O. Kwon, M. Sattorov, S. Kim, S.-H. Park, D. Hong, S. Kim, C. Park, B. H. Hong, I. Cho, S. Ma, M. Kim, Y. J. Yoo, S. Y. Park, and G.-S. Park, "Analysis of electromagnetic pulse effects under high-power microwave sources," *IEEE Access*, vol. 9, pp. 136775–136791, 2021.

[19] N. Marcuvitz, *Waveguide handbook*. No. 21, Iet, 1951.

[20] J. R. Wait, "Some boundary value problems involving plasma," *Journal of Research of the National Bureau of Standards: Mathematics and mathematical physics. B*, vol. 65, p. 137, 1961.

[21] H.-M. Shen, "Plasma waveguide: A concept to transfer electromagnetic energy in space," *Journal of applied physics*, vol. 69, no. 10, pp. 6827–6835, 1991.

[22] M. Liu, "Four-layer tunable wideband electromagnetic shield based on cold plasma," *IEEE Access*, vol. 8, pp. 171621–171627, 2020.

[23] S. M. Khalil, K. H. El-Shorbagy, and E. El-Siragy, "Minimizing energy losses in a plasma-filled wave-guide," *Contributions to Plasma Physics*, vol. 42, no. 1, pp. 67–80, 2002.

[24] R. L. Ives, M. Read, T. Bui, D. Marsden, G. Collins, H. Freund, R. Ho, L. Higgins, C. Walker, J. Conant, *et al.*, "High efficiency, low cost, rf sources for accelerators and colliders," *Journal of Instrumentation*, vol. 18, no. 05, p. T05003, 2023.

[25] A. Shivarova and I. Zhelyazkov, "Surface waves in a homogeneous plasma sharply bounded by a dielectric," *Plasma Physics*, vol. 20, no. 10, p. 1049, 1978.

[26] G. Zhou, B. Zhu, J. Zhao, G. Zhu, B. Jin, Y. Feng, L. Kang, W. Xu, J. Chen, and P. Wu, "A broadband reflective-type half-wave plate employing optical feedbacks," *Scientific Reports*, vol. 7, no. 1, p. 9103, 2017.

[27] A. Yahyaoui, H. Rmili, K. Achouri, M. Sheikh, A. Dobaie, A. Affandi, T. Aguili, *et al.*, "Transmission control of electromagnetic waves by using

quarter-wave plate and half-wave plate all-dielectric metasurfaces based on elliptic dielectric resonators," *International Journal of Antennas and Propagation*, vol. 2017, 2017.

[28] Z. Gong, A. Robinson, X. Yan, and A. Arefiev, "Highly collimated electron acceleration by longitudinal laser fields in a hollow-core target," *Plasma Physics and Controlled Fusion*, vol. 61, no. 3, p. 035012, 2019.

[29] T. Wang, Z. Gong, K. Chin, and A. Arefiev, "Impact of ion dynamics on laser-driven electron acceleration and gamma-ray emission in structured targets at ultra-high laser intensities," *Plasma Physics and Controlled Fusion*, vol. 61, no. 8, p. 084004, 2019.

[30] H. Malik, S. Kumar, and K. Singh, "Electron acceleration in a rectangular waveguide filled with unmagnetized inhomogeneous cold plasma," *Laser and Particle Beams*, vol. 26, no. 2, pp. 197–205, 2008.

[31] N. Sakhnenko, A. Nerukh, and N. Ruzhitskaya, "Transformation of radiation by appearance of a cylindrical plasma inclusion in a waveguide," in *Proceedings of 2002 4th International Conference on Transparent Optical Networks (IEEE Cat. No. 02EX551)*, vol. 2, pp. 108–111, IEEE, 2002.

[32] O. Gehre, H. Mayer, and M. Tutter, "Propagation of microwaves in a circular waveguide partially filled with a cold plasma dielectric," *Zeitschrift für Naturforschung A*, vol. 27, no. 2, pp. 215–221, 1972.

[33] H. Kinderdijk and H. Hagebeuk, "The propagation of electromagnetic waves in a circular waveguide containing a cold cylindrically stratified plasma," *Physica*, vol. 52, no. 2, pp. 299–315, 1971.

[34] M. U. Shahid, A. Ghaffar, M. A. Alkanhal, and Y. Khan, "Propagation of electromagnetic waves in graphene-wrapped cylindrical waveguides filled with magnetized plasma," *Optik*, vol. 244, p. 167566, 2021.

[35] Y. Geng, X. Wu, and L.-W. Li, "Analysis of electromagnetic scattering by a plasma anisotropic sphere," *Radio Science*, vol. 38, no. 6, pp. 12–1, 2003.

[36] J. Sui, R. Dong, S. Liao, Z. Zhao, Y. Wang, and H.-F. Zhang, "Janus metastructure based on magnetized plasma material with and logic gate and multiple physical quantity detection," *Annalen der Physik*, vol. 535, no. 3, p. 2200509, 2023.

[37] H. Ikegami, "Scattering of microwaves from a plasma column in rectangular waveguide," *Japanese Journal of Applied Physics*, vol. 7, no. 6, p. 634, 1968.

[38] G. Cicconi, V. Molinari, and C. Rosatelli, "Microwave reflection from a plasma column in a rectangular waveguide," *Japanese Journal of Applied Physics*, vol. 12, no. 5, p. 721, 1973.

[39] G. Zaginaylov, V. Shcherbinin, and K. Shuenemann, "On the dispersion properties of waveguides filled with a magnetized plasma," *Plasma physics reports*, vol. 31, pp. 596–603, 2005.

[40] F. Hedayatian, M. Salem, and S. Saviz, "Cylindrical waveguide filled with radially inhomogeneous magnetized plasma as a microwave accelerating structure," *Physics of Plasmas*, vol. 25, no. 1, 2018.

[41] Y. A. Akimov, N. Azarenkov, and V. Olefir, "Non-symmetric surface waves in cylindrical waveguide structures with radially non-uniform plasma filling," *Physica Scripta*, vol. 67, no. 4, p. 329, 2003.

[42] V. Girka and I. Girka, "Asymmetric long-wavelength surface waves in magnetized plasma waveguides entirely filled with plasma," *Plasma Physics Reports*, vol. 28, pp. 916–924, 2002.

[43] A. Aleksandrov, M. Kuzelev, and A. Rukhadze, "Electromagnetic waves in cylindrical plasma-dielectric structures," *Journal of Communications Technology and Electronics*, vol. 53, no. 12, pp. 1359–1379, 2008.

[44] A. Helaly, E. Soliman, and A. Megahed, "Electromagnetic waves scattering by nonuniform plasma cylinder," *IEE Proceedings-Microwaves, Antennas and Propagation*, vol. 144, no. 2, pp. 61–66, 1997.

[45] S. M. Khalil and N. Mousa, "Dispersion characteristics of plasma-filled cylindrical waveguide," *Journal of Theoretical and Applied Physics*, vol. 8, pp. 1–14, 2014.

[46] K. Thomassen, "Interaction between a dielectric (or cold plasma) and a cavity," *Journal of Applied Physics*, vol. 34, no. 6, pp. 1622–1629, 1963.

[47] W. M. Manheimer, "Nonlinear development of an electron plasma wave in a cylindrical waveguide," *The Physics of Fluids*, vol. 12, no. 11, pp. 2426–2428, 1969.

[48] J. M. Dawson and C. R. Oberman, *Oscillations of a finite cold plasma in a strong magnetic field*, vol. 8053. United States Atomic Energy Commission, Technical Information Service, 1958.

[49] S. Kumar and M. Yoon, "Electron dynamics and acceleration study in a magnetized plasma-filled cylindrical waveguide," *Journal of Applied Physics*, vol. 103, no. 2, 2008.

[50] A. York, H. Milchberg, J. Palastro, and T. Antonsen, "Direct acceleration of electrons in a corrugated plasma waveguide," *Physical review letters*, vol. 100, no. 19, p. 195001, 2008.

[51] A. Abdoli-Arani, B. Jazi, and B. Shokri, "Acceleration of an electron inside the circular and elliptical waveguides by microwave radiation," *IEEE Transactions on Plasma Science*, vol. 41, no. 1, pp. 62–69, 2012.

[52] T. Y. Alekhina and A. V. Tyukhtin, "Cherenkov-transition radiation in a waveguide partly filled with a strongly magnetized plasma," *Radiation Physics and Chemistry*, vol. 164, p. 108364, 2019.

[53] F. Aghamir and M. Abbas-nejad, "Dispersion characteristics of cyclotron waves in a warm plasma waveguide," in *2007 16th IEEE International Pulsed Power Conference*, vol. 1, pp. 505–508, IEEE, 2008.

[54] V. Bevc, "Wave propagation in a waveguide partially filled with plasma in an infinite axial magnetic field," *Journal of Applied Physics*, vol. 38, no. 12, pp. 4857–4866, 1967.

[55] S. Rao, H. Fu, J. Zhang, D. Zhang, and H. Zhang, "Tunable phase retarder of 1d layered photonic structure combining nonlinear kerr dielectric defect layers and magnetized plasma materials," *Annalen der Physik*, vol. 534, no. 11, p. 2200337, 2022.

[56] S. Mohseni Armaki, M. Tohidlo, and M. Kazerooni, "Design and fabrication of coaxial plasma waveguide filter with the ability to reconfigure the frequency band," *Journal of Electrical and Computer Engineering Innovations (JECEI)*, vol. 11, no. 1, pp. 75–84, 2023.

[57] W. Leemans, "Beams and plasmas," *Physics Today*, vol. 72, no. 2, pp. 40–41, 2019.

[58] A. Klimov, A. Zenin, T. Van Tu, and I. Y. Bakeev, "Electron-beam plasma and its applications to polymer treatment in the forevacuum," in *Journal of Physics: Conference Series*, vol. 1393, p. 012097, IOP Publishing, 2019.

[59] S. Kobayashi, T. M. Antonsen, and G. S. Nusinovich, "Linear theory of a plasma loaded, helix type, slow wave amplifier," *IEEE transactions on plasma science*, vol. 26, no. 3, pp. 669–679, 1998.

[60] Y. Cao, J. Leopold, Y. P. Bliokh, G. Leibovitch, and Y. E. Krasik, "Nonlinear absorption of high-power microwave pulses in a plasma filled waveguide," *Physics of Plasmas*, vol. 28, no. 6, 2021.

[61] S. L. Dvorak, R. W. Ziolkowski, and D. G. Dudley, "Ultra-wideband electromagnetic pulse propagation in a homogeneous, cold plasma," *Radio Science*, vol. 32, no. 1, pp. 239–250, 1997.

[62] B. Jazi, Z. Rahmani, and B. Shokri, "Reflection and absorption of electromagnetic wave propagation in an inhomogeneous dissipative magnetized plasma slab," *IEEE Transactions on Plasma Science*, vol. 41, no. 2, pp. 290–295, 2013.

[63] G. S. Nusinovich, Y. Carmel, T. M. Antonsen, D. M. Goebel, and J. Santoru, "Recent progress in the development of plasma-filled traveling-wave tubes and

backward-wave oscillators," *IEEE Transactions on Plasma Science*, vol. 26, no. 3, pp. 628–645, 1998.

[64] E. Abubakirov, A. Konyushkov, A. Leontyev, R. Rozental, and V. Tarakanov, "Multi-pass relativistic traveling-wave tube with simultaneous operation on symmetric and asymmetric modes," *Physics of Plasmas*, vol. 27, no. 7, 2020.

[65] Y. Carmel, J. Ivers, R. Kribel, and J. Nation, "Intense coherent cherenkov radiation due to the interaction of a relativistic electron beam with a slow-wave structure," *Physical Review Letters*, vol. 33, no. 21, p. 1278, 1974.

[66] X. Hong-Quan and L. Pu-Kun, "Theoretical analysis of a relativistic travelling wave tube filled with plasma," *Chinese Physics*, vol. 16, no. 3, p. 766, 2007.

[67] X. Hong-Quan and L. Pu-Kun, "Analysis of the axial electric field in a plasma-loaded-helix travelling wave tube," *Chinese Physics*, vol. 15, no. 9, p. 2042, 2006.

[68] S. Bayat, S. Babanejad, S. M. Hasheminejad, and S. M. Vahabi, "Exact numerical solution of the dispersion relation in relativistic backward-wave oscillator and relativistic travelling-wave tube filled with plasma," *Plasma Physics and Controlled Fusion*, vol. 56, no. 12, p. 125009, 2014.

[69] Q. Yang, B. Wei, L. Li, and D. Ge, "Simulation of electromagnetic waves in a magnetized cold plasma by the so-dgtd method," *IEEE Transactions on Antennas and Propagation*, vol. 66, no. 8, pp. 4151–4157, 2018.

[70] G. Mur, "Absorbing boundary conditions for the finite-difference approximation of the time-domain electromagnetic-field equations," *IEEE transactions on Electromagnetic Compatibility*, no. 4, pp. 377–382, 1981.

[71] R. J. Luebbers, F. Hunsberger, and K. S. Kunz, "A frequency-dependent finite-difference time-domain formulation for transient propagation in plasma," *IEEE Transactions on Antennas and Propagation*, vol. 39, no. 1, pp. 29–34, 1991.

[72] T. Otsuyama and M. Hayakawa, "Fdtd simulation and experimental result on vlf scattering by ionospheric perturbations in earth-ionosphere waveguide,"

IEEJ Transactions on Fundamentals and Materials, vol. 122, no. 1, pp. 59–64, 2002.

[73] H. Yang and V. P. Pasko, "Three-dimensional finite difference time domain modeling of the diurnal and seasonal variations in schumann resonance parameters," *Radio Science*, vol. 41, no. 02, pp. 1–10, 2006.

[74] T. Tan, A. Taflove, and V. Backman, "Single realization stochastic fdtd for weak scattering waves in biological random media," *IEEE transactions on antennas and propagation*, vol. 61, no. 2, pp. 818–828, 2012.

[75] S. M. Smith and C. Furse, "Stochastic fdtd for analysis of statistical variation in electromagnetic fields," *IEEE Transactions on Antennas and Propagation*, vol. 60, no. 7, pp. 3343–3350, 2012.

[76] A. Samimi and J. J. Simpson, "An efficient 3-d fdtd model of electromagnetic wave propagation in magnetized plasma," *IEEE Transactions on Antennas and Propagation*, vol. 63, no. 1, pp. 269–279, 2014.

[77] Y. Fang, J.-F. Liu, Z.-H. Jiao, G.-H. Bai, and X.-L. Xi, "A 3-d stochastic fdtd algorithm for wave propagation in isotropic cold plasma medium based on bilinear transform," *IEEE Transactions on Plasma Science*, vol. 47, no. 1, pp. 173–178, 2018.

[78] J.-F. Liu, J. Wang, Y. Fang, Y.-R. Pu, and X.-L. Xi, "An unconditionally stable stochastic wlp-fdtd algorithm for wave propagation in isotropic cold plasma media," *IEEE Microwave and Wireless Components Letters*, vol. 28, no. 10, pp. 852–854, 2018.

[79] Y. Fang, X.-L. Xi, J.-M. Wu, J.-F. Liu, and Y.-R. Pu, "A je collocated wlp-fdtd model of wave propagation in isotropic cold plasma," *IEEE Transactions on Microwave Theory and Techniques*, vol. 64, no. 7, pp. 1957–1965, 2016.

[80] Y. Yu and J. J. Simpson, "An ej collocated 3-d fdtd model of electromagnetic wave propagation in magnetized cold plasma," *IEEE Transactions on Antennas and Propagation*, vol. 58, no. 2, pp. 469–478, 2009.

[81] B. T. Nguyen, A. Samimi, and J. J. Simpson, "A polynomial chaos approach for em uncertainty propagation in 3d-fdtd magnetized cold plasma," in *2015 IEEE Symposium on Electromagnetic Compatibility and Signal Integrity*, pp. 356–360, IEEE, 2015.

[82] Y. G. Smirnov and D. V. Valovik, "Guided electromagnetic waves propagating in a plane dielectric waveguide with nonlinear permittivity," *Physical Review A*, vol. 91, no. 1, p. 013840, 2015.

[83] J. Galejs, "Impedance of a finite insulated antenna in a cold plasma with a perpendicular magnetic field," *IEEE Transactions on Antennas and Propagation*, vol. 14, no. 6, pp. 737–748, 1966.

[84] C. M. Davies, "The boundary layer between a cold plasma and a confined magnetic field when the plasma is not normally incident on the boundary," *Planetary and Space Science*, vol. 16, no. 10, pp. 1249–1257, 1968.

[85] F. Leuterer and H. Derfler, "Gap excitation of plasma waves in a bounded inhomogeneous cold plasma," *Plasma Physics*, vol. 18, no. 6, p. 453, 1976.

[86] T. Y. Alekhina and A. V. Tyukhtin, "Electromagnetic field of a charge intersecting a cold plasma boundary in a waveguide," *Physical Review E*, vol. 83, no. 6, p. 066401, 2011.

[87] P. Li and L. J. Jiang, "Simulation of electromagnetic waves in the magnetized cold plasma by a dgfetd method," *IEEE Antennas and Wireless Propagation Letters*, vol. 12, pp. 1244–1247, 2013.

[88] X. M. Mitsalas, T. Kaifas, and G. Kyriacou, "Wiener-hopf analysis of planar canonical structures loaded with longitudinally magnetized plasma biased normally to the extraordinary wave propagation: Near and far field," *Progress In Electromagnetics Research B*, vol. 88, pp. 119–149, 2020.

[89] S. Lee, "Cylindrical antenna in uniaxial resonant plasmas," *Radio Science*, vol. 4, no. 2, pp. 179–189, 1969.

[90] A. Abdoli-Arani, "Modification of density profile at interaction of three superposing fundamental modes with plasma in a cylindrical waveguide," *Waves in Random and Complex Media*, vol. 24, no. 3, pp. 316–332, 2014.

[91] D. Nguyen, "The infinite cylindrical antenna in a compressible plasma," *Canadian Journal of Physics*, vol. 46, no. 11, pp. 1311–1321, 1968.

[92] L. Chaohui, C. Zhaoquan, L. Minghai, J. Zhonghe, and H. Xiwei, "Three-dimensional numerical simulation of surface-wave plasma source," *Plasma Science and Technology*, vol. 11, no. 1, p. 66, 2009.

[93] S. Ikuno, Y. Fujita, T. Itoh, S. Nakata, H. Nakamura, and A. Kamitani, "Numerical simulation of electromagnetic wave propagation using time domain meshless method," *Plasma and Fusion Research*, vol. 7, pp. 2406044–2406044, 2012.

[94] B. Tiryakioglu, "Mode matching analysis of sound waves in an infinite pipe with perforated screen," *Acoustical Physics*, vol. 66, no. 6, pp. 580–586, 2020.

[95] H. Alahmadi, R. Nawaz, M. Alkinidri, and A. Alruwaili, "Noise control from dual air cavity membranes in a rigid waveguide," *Meccanica*, vol. 57, no. 12, pp. 3023–3032, 2022.

[96] B. Tiryakioglu, "Sound radiation from non-uniformly lined duct with partial rigidity," *Computational Mathematics and Mathematical Physics*, vol. 61, no. 12, pp. 2118–2128, 2021.

[97] H. Alahmadi, H. Afsar, R. Nawaz, and M. O. Alkinidri, "Scattering characteristics through multiple regions of the wave-bearing trifurcated waveguide," *Waves in Random and Complex Media*, pp. 1–17, 2022.

[98] J. V. H.T. Anastassiu and D. Ross, "The mode matching technique for electromagnetic scattering by cylindrical waveguides with canonical terminations," *Journal of Electromagnetic Waves and Applications*, vol. 9, no. 11-12, pp. 1363–1391, 1995.

[99] J. Dai and Q. H. Liu, "Efficient computation of electromagnetic waves in anisotropic orthogonal-plano-cylindrically layered media using the improved

numerical mode matching (nmm) method," *IEEE Transactions on Antennas and Propagation*, vol. 63, no. 8, pp. 3569–3578, 2015.

[100] Q.-H. Liu and W. C. Chew, "Numerical mode-matching method for the multi-region vertically stratified media (em wave propagation)," *IEEE transactions on antennas and propagation*, vol. 38, no. 4, pp. 498–506, 1990.

[101] C. Bachiller, H. Esteban, H. Mata, M. Á. Valdés, V. E. Boria, Á. Belenguer, and J. V. Morro, "Hybrid mode matching method for the efficient analysis of metal and dielectric rods in h plane rectangular waveguide devices," *IEEE transactions on microwave theory and techniques*, vol. 58, no. 12, pp. 3634–3644, 2010.

[102] U. Balaji and R. Vahldieck, "Mode-matching analysis of circular-ridged waveguide discontinuities," *IEEE transactions on microwave theory and techniques*, vol. 46, no. 2, pp. 191–195, 1998.

[103] E. D. Caballero, H. Esteban, A. Belenguer, and V. Boria, "Efficient analysis of substrate integrated waveguide devices using hybrid mode matching between cylindrical and guided modes," *IEEE transactions on microwave theory and techniques*, vol. 60, no. 2, pp. 232–243, 2012.

[104] C. G. Wells and J. A. Ball, "Mode-matching analysis of a shielded rectangular dielectric-rod waveguide," *IEEE transactions on microwave theory and techniques*, vol. 53, no. 10, pp. 3169–3177, 2005.

[105] L. Christie and P. Mondal, "Mode matching method for the analysis of cascaded discontinuities in a rectangular waveguide," *Procedia Computer Science*, vol. 93, pp. 251–258, 2016.

[106] S. Najari, B. Jazi, and S. Jahanbakht, "The mode generation due to the wave transmission phenomena from a loss free isotropic cylindrical metallic waveguide to the semi-bounded plasma waveguide," *Waves in Random and Complex Media*, vol. 31, no. 6, pp. 1287–1302, 2021.

[107] A. Abdoli-Arani and M. Moghaddasi, "Study of electron acceleration through the mode in a collisional plasma-filled cylindrical waveguide," *Waves in Random and Complex Media*, vol. 26, no. 3, pp. 339–347, 2016.

[108] A. P. Gashturi, A. V. Palitsin, M. B. Goykhman, A. V. Gromov, A. Panin, M. D. Proyavin, and Y. V. Rodin, "Microwave notch filters for plasma diagnostics, numerical simulation by method of moments with mode matching," in *2021 46th International Conference on Infrared, Millimeter and Terahertz Waves (IRMMW-THz)*, pp. 1–2, IEEE, 2021.

[109] F. Arndt, R. Beyer, J. M. Reiter, T. Sieverding, and T. Wolf, "Automated design of waveguide components using hybrid mode-matching/numerical em building-blocks in optimization-oriented cad frameworks-state of the art and recent advances," *IEEE Transactions on Microwave Theory and Techniques*, vol. 45, no. 5, pp. 747–760, 1997.

[110] Y.-h. Liu and H.-f. Li, "An application of the mode-matching technique in the calculation of resonators in gyro-devices," *Nuclear Instruments and Methods in Physics Research Section A: Accelerators, Spectrometers, Detectors and Associated Equipment*, vol. 598, no. 2, pp. 605–610, 2009.

[111] J. B. Lawrie, "On eigenfunction expansions associated with wave propagation along ducts with wave-bearing boundaries," *IMA journal of applied mathematics*, vol. 72, no. 3, pp. 376–394, 2007.

[112] J. Lawrie, "Orthogonality relations for fluid-structural waves in a three-dimensional, rectangular duct with flexible walls," *Proceedings of the Royal Society A: Mathematical, Physical and Engineering Sciences*, vol. 465, no. 2108, pp. 2347–2367, 2009.

[113] R.-B. Hwang, *Periodic structures: mode-matching approach and applications in electromagnetic engineering.* John Wiley & Sons, 2012.

[114] E. Cojocaru, "Modes in dielectric or ferrite gyrotropic slab and circular waveguides, longitudinally magnetized, with open and completely or partially filled wall," *JOSA B*, vol. 27, no. 10, pp. 1965–1977, 2010.

[115] M. Ayub, T. A. Khan, and K. Jilani, "Effect of cold plasma permittivity on the radiation of the dominant tem-wave by an impedance loaded parallel-plate waveguide radiator," *Mathematical Methods in the Applied Sciences*, vol. 39, no. 1, pp. 134–143, 2016.

[116] A. Ishimaru, *Electromagnetic wave propagation, radiation, and scattering: from fundamentals to applications.* John Wiley & Sons, 2017.

[117] D. G. Swanson, *Plasma waves.* CRC Press, 2020.

[118] N. A. Krall, A. W. Trivelpiece, and R. A. Gross, "Principles of plasma physics," *American Journal of Physics*, vol. 41, no. 12, pp. 1380–1381, 1973.

[119] K. Nagaya and K. Poltorak, "Method for solving eigenvalue problems of the helmholtz equation with a circular outer and a number of eccentric circular inner boundaries," *The Journal of the Acoustical Society of America*, vol. 85, no. 2, pp. 576–581, 1989.

[120] T. Rother, "General aspects of solving helmholtz's equation underlying eigenvalue and scattering problems in electromagnetic wave theory," *Journal of electromagnetic waves and applications*, vol. 13, no. 7, pp. 867–888, 1999.

[121] M. Karimaghaei and A.-V. Phan, "Boundary integral formulation of the standard eigenvalue problem for the 2-d helmholtz equation," *Engineering Analysis with Boundary Elements*, vol. 132, pp. 281–288, 2021.

[122] H. J. Eom, "Electromagnetic wave theory for boundary-value problems," *An Advanced Course on Analytical Methods*, 2004.

[123] D. Shiffler, J. A. Nation, and G. S. Kerslick, "A high-power, traveling wave tube amplifier," *IEEE transactions on plasma science*, vol. 18, no. 3, pp. 546–552, 1990.

[124] S. Saviz, "Self-consistent and complete field theory of relativistic travelling wave tube amplifier with plasma loaded tape helix," *Canadian Journal of Physics*, vol. 90, no. 12, pp. 1237–1257, 2012.